Structural and Electrical Characteristics of Printed Metal Nanoparticle Networks

Claire Barbara van den Berg

A thesis submitted in fulfilment of the requirements
for the degree of Masters in Science
in the Department of Physics
University of CapeTown

December 10, 2016

Abstract

The structural and electrical properties of metal nanoparticle (NP) networks and their dependence on the constituent phases have been investigated. Percolation and effective media theories have been used to describe the physical properties of disordered systems, as well as providing a link between their structural features and the corresponding electrical transport properties. Silver and palladium nanoparticulate layers in ethyl cellulose polymer binder (ETHOCEL^{TM}), were fabricated onto paper using the method of screen printing. The metal-binder ratios were varied in order to observe changes in the microstructure when a percolating network consisting of the metal NPs is formed through the layer. The electron microscopy studies revealed the microstructural features of the silver and palladium layers to be different. The silver NPs aggregate into dense clusters resulting in a tightly packed layer, whereas the palladium NPs assembled into "chain-like" structures which produced a more "loosely" packed layer. The electrical conductivity, I-V characteristics and Hall effect for the metal layers were studied as a function of metal NP concentration. The two exponent phenomenological percolation equation (TEPPE) was fitted to the conductivity data for the silver and palladium systems which revealed the percolation threshold (φ_c) to be higher in the silver layers. For both metal systems the Hall coefficient and Hall mobility showed a dependence on particle concentration with the largest changes in their magnitude observed in the region of φ_c. Insight into the microscopic charge transport through the metal layers was provided by impedance spectroscopy studies. Equivalent circuit models based on the microstructural features of the layers were proposed. For both metal systems, the printed layers with particle loadings below φ_c could be described by a $R - CPE$ circuit, whereas for concentrations above φ_c a $RL - C$ circuit was used. It can be shown that differences observed in the values of R, L and C for the silver and palladium layers can be related to the manner in which the metal NPs aggregate to form the final microstructure.

Acknowledgements

To my family, thank you for your love and encouragement through the years. To Batsirai Magunje and Emmanuel Jonah, thank you for the guidance and support. I would like to thank my supervisors, Prof. M. Blumenthal and Dr. M. Topic, and my former supervisor Prof M. Härting for their support. I would like to acknowledge Prof D. T. Britton for his assistance on aspects of this work. I would also like to thank Prof. M.E. Lee, Dr. J.E. Olivier and Mr. A. Janse van Vuuren from the Centre for High Resolution Transmission Electron Microscopy at Nelson Mandela Metropolitan University, for their assistance with the electron microscopy measurements. Thank you to Mrs. M. Waldrin and Mr. M. Jaffer from the Electron Microscopy Unit at the University of Cape Town, for their support with the electron microscopy measurements. Special thanks to the electrical engineering department at the Cape Peninsula University of Technology, for allowing access to the impedance spectrometer. I would also like to thank my sponsors over the coarse of this thesis, the South African National Research Foundation (NRF)/iThemba LABS and Mintek.

Contents

Abstract i

Acknowledgements ii

1 Introduction 1

2 Metallic Nanoparticles 3

2.1 General Properties of Metal Nanoparticles 3

2.1.1 Silver (Ag) 6

2.1.2 Palladium (Pd) 6

2.2 Metal Nanoparticle Production 7

2.2.1 Top-Down Methods 7

2.2.2 Bottom-Up Methods 8

3 Electrical Properties in Disordered Systems 11

3.1 Percolation Theory 11

3.1.1 Lattice Percolation 11

3.1.2 Topological Properties of Percolation Structures 13

3.1.3 Continuum Percolation 16

3.2 Effective Media Theories 19

3.3 Two-Exponent Phenomenological Percolation Equation (TEPPE) 21

3.4 Magneto-transport Properties of Metals 23

3.4.1 Hall Effect and Magnetoresistance in Bulk Metals 23

3.4.2 Low- and High-Field Galvanomagnetic Properties of Metals 27

4 Experimental Procedure **30**

4.1 Sample Preparation 30

4.1.1 Materials 30

4.1.2 Preparation of Nanoparticle Inks 30

4.1.3 Screen Printing 31

4.2 Structural Characterisation of the Metal Nanoparticles 33

4.3 Structural Characterisation of the Printed Layers 33

4.3.1 Argon Ion Beam Polishing 34

4.3.2 Focused Ion Beam Milling 35

4.4 Electrical Characterisation 38

4.4.1 Hall Effect Measurements 38

4.4.2 Impedance Spectroscopy 43

5 Results and Analysis **45**

5.1 Morphological Characterisation 45

5.1.1 Morphology of the Metal Nanoparticles 45

5.1.2 Morphology of the Printed Layers 46

5.2 Electrical Characterisation 58

5.2.1 Percolative Behaviour of the Printed Layers 58

5.2.2 I-V Charactersitics of the Metal Layers 60

5.2.3 Hall Effect Measurements 62

5.2.4 Impedance Spectroscopy 65

6 Discussion **71**

6.1 Electron Microscopy 71

6.2 Conductivity of the Metal Layers 72

6.3 I-V Characteristics 73
6.4 Hall Effect Parameters 74
6.5 Impedance Spectroscopy of Metal Layers 77

7 Conclusion **80**

References **97**

1. Introduction

Printed electronics technology has attracted interest over the last few years as an alternative to conventional methods for the fabrication of electronic and optelectronic devices. Printing techniques such as screen and inkjet printing and roll-printing (flexography and gravure printing) have been used for patterning a wide variety of devices such as sensors, transistors, radio-frequency identification (RFID) tags, flexible batteries and solar cells [1, 2, 3, 4, 5]. These techniques are advantageous because they are relatively simple, promise low production cost and can be adapted for large scale production. Another advantage is the wide variety of materials such as paper, plastics and ceramics that can be used as substrates [6, 7, 8]. One of the major challenges is to formulate suitable inks for the different printing techniques. Functional electronics inks consist of nanoparticles (NPs) with specific properties, dispersed in a liquid medium [7, 9]. Printing the inks involves the selectively deposition of the functional materials onto a substrate followed by a curing stage which may involve a number of processing steps [6, 10]. In order for the proper functioning of these devices, contacts as well as conductive structures are required [5]. For this reason metallic NPs are of particular interest due to their applications in forming conductive tracks and films in these devices [1, 4, 5].

The basic requirement for the printed layer to display metallic behaviour is that the particle fraction must be above a critical threshold [11]. Above this critical concentration the metal NPs aggregate to form a connected network that traverses the layer, thus providing paths along which charge can flow [5, 12, 13]. The printed layers which comprise of a conductive phase (metal NPs) dispersed in an insulating medium (binder), can be classified as a percolative material. Percolation theory (PT) has been used to describe the electrical conductivity of disordered media near to the critical threshold where the system undergoes an abrupt change from insulating to metallic as the amount of the conducting phase is increased [14, 15]. Other models such as the effective medium theories (EMT) describe the electrical properties for concentrations further away from the critical threshold. EMT describes the effective conductivity of a inhomogeneous medium which is determined by averaging over the different constituent phases [16, 17]. A more recent model known as the two exponent phenomenological percolation equation (TEPPE), which combines aspects from both PT and EMT, has been used to analyse the conductivity data for a number of percolating systems [18, 19]. In order for these materials to be used in electronic devices, it is essential to understand how the physical properties are affected by the composition and packing arrangement

of their components [15, 20, 21].

In this study, the effect of metal NP loading on the electrical properties and morphology of the layers was determined. Silver (Ag) and palladium (Pd) nanoparticulate inks were produced with different metal-binder concentrations and deposited onto a substrate using screen printing. The TEPPE was applied to the *dc* electrical conductivity data in order to determine the critical concentration at which the system undergoes a structural phase transition from insulating to conducting. The I-V characteristics of the layers were used infer changes in the charge transport mechanism with particle loading. Changes in the microstructure of the printed layers with different particle loadings was investigated using scanning electron microscopy (SEM) and high resolution transmission electron microscopy (HRTEM). Hall effect measurements were performed on the printed layers in order to ascertain information about the charge carriers as a function of particle loading. In addition to this, impedance spectroscopy measurements were performed in order to find a suitable model to describe the conduction mechanism based on the microstructural features of the layer.

This thesis is laid out as follows; chapter 2 provides an overview of the properties of metal NPs followed by a brief discussion on the various techniques employed to produce the particles. Chapter 3 gives a review of the theories used to describe the electrical conduction in disordered systems. This is followed with a discussion on the Hall effect in metals. The experimental procedure is given in chapter 4 which describes in detail the techniques used to produce and measure the nanoparticulate samples. This is followed with the analysis of the data given in chapter 5. The interpretation of the data is presented in chapter 6 and conclusions from this study as well as recommendations for future work is given in chapter 7.

2. Metallic Nanoparticles

In this section an overview of the physical and chemical properties of metal NPs is given, with an emphasis on how the reduction in size affects the crystalline and electronic structure of the metal. The properties of two metals namely, silver (Ag) and palladium (Pd) are discussed. This is followed with a brief description of the techniques used to produce metal NPs.

2.1 General Properties of Metal Nanoparticles

NP have garnered interest over the last few decades due to their display of unique physical and chemical properties which differ from that of the bulk form and atomic level [22, 23]. NP in general can be defined as any particle with lateral dimensions less than 100 nm [24], with a nuclearity ranging from 10 to 10^{10} or more metal atoms per particle [23]. These particles can be a single crystallite, an aggregate of a number of crystallites or noncrystalline [25]. The majority of metal NP will have either hexagonal or cubic close-packed crystal structures. The metal NP comprises of a central atom that is encompassed by a number of densely-packed shells [26, 27]. The differences in the metal properties as one moves from the bulk to the atomic scale can be attributed to two types of size dependent effects. The first is the scalable effects that are related to the number of surface atoms [22, 28] and the second being quantum size effects which involves changes to the electronic structure of the metal nanoparticles [24, 29].

As the size of the metal is reduced from bulk to the nanometre regime the surface-to-volume ratio increases [26, 30]. As a result the proportion of atoms found on the surface will increase with decreasing particle size. Assuming that the particles are spherical in shape, the fraction of atoms at the surface is given by $P_s(N) = 4N^{-1/3}$, where N known as the nuclearity, is the number of atoms in the nanocrystal [28, 31]. The atoms located in the interior of the particle are coordinately saturated and are therefore highly stable [28], unlike the surface atoms which are coordinately unsaturated and weakly bound [24, 30, 32]. The atoms located at the corners and on the edges of the particle are more highly reactive compared to the atoms lying in the surface planes [26, 28]. As a result, there are a number of physiochemical properties of the metal NPs that are affected by the change in the number of surface atoms [24]. As the fraction of surface atoms increases so will the number of active sites which will

affect the surface bonding and chemical reactivity of the NP [23, 32]. For this reason, metal NPs are ideal candidates for surface dependent chemical processes (*e.g* catalysis, corrosion, oxidation and reduction) [26, 33]. Another property that is affected is the temperature of the melting point which decreases with decreasing particle size [24, 30]. As the dimensions of the metal NP is reduced, the surface energy is raised due to an increase in the number of corner and edge atoms on the surface [30, 34]. The smaller the metal NP size, the more easily the surface atoms can rearrange which in turn causes the melting process to start at a lower temperature [26, 30].

All properties of a solid are dependent on the energy gap between the conduction and valence bands [35]. The band structure determines how the electrons are allowed to execute their motion in the material [26, 36]. In bulk metals, there is no bandgap and the electrons which are highly delocalised within the partially filled conduction band can therefore move freely in the unoccupied bands [26, 36, 37]. With a decrease in the particles dimension, the electron wavefunction becomes spatially confined [32, 36]. If the particles size is reduced to a point where it is comparable to that of the electrons wavelength, then the electrons energy becomes discrete due to quantum confinement [12]. As a result a energy gap (δ) begins to appear between the valence and conduction bands [28, 36]. This is known as the Kubo gap, and it is related to the temperature T by,

$$k_B T = \delta = \frac{4E_F}{3N} \tag{2.1}$$

where k_B is the Boltzman constant and E_F is the Fermi energy [38]. Metal particles of finite size will have discrete electronic energy levels unlike in bulk which is continuous [29]. From equation 2.1, it states that the energy gap δ between the conduction and valence band will increase with decreasing particle size [12]. As the particle diameter D is reduced to the mesoscopic size, the metallic property of the particles will be maintained provided that $\delta < k_B T$. With a further reduction in the particle size, the system will undergo a transition from a metallic to insulating state when $\delta > k_B T$ [31, 38]. When δ becomes approximately equal to or greater than $k_B T$, then the system undergoes a transition from a metallic to semiconducting state. Upon further reduction, the energy separation increases and the system becomes insulating. This size-induced metal-to-insulator transition is shown in figure 2.1. Table 2.1 gives the relevant values for D, δ and N in the different size regimes.

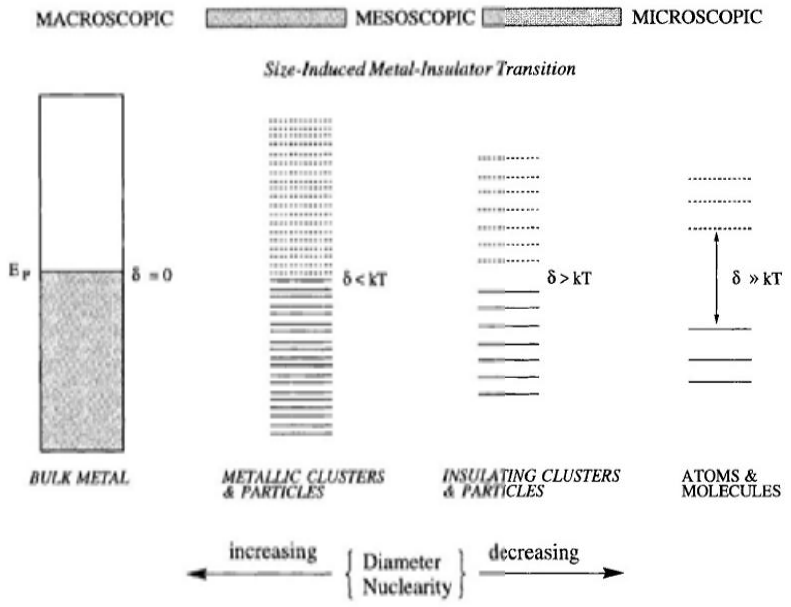

Fig. 2.1: Schematic diagram showing the gradual change in the band gap and density of states (DOS) as the nuclearity of the metal system increases [31].

Table 2.1: The approximate values for the diameter D, nuclearity N and Kubo gap δ in the different size regimes [29].

Bulk Metal	Metal NP	Insulating NP	Atoms and Molecules
$D >> 10^4$ Å	$D \approx 10^4 - 10^2$ Å	$D \approx 10^2 - 10$ Å	$D < 10$ Å
$N >> 10^{10}$	$N \approx 10^{10} - 10^4$	$N \approx 10^4 - 10$	$N < 10$
$\delta << 10^{-6}K$	$\delta \approx 10^{-6} - 1K$	$\delta \approx 1 - 10^3K$	$\delta > 10^3K$

The electron confinement has shown to have a profound effect on the optical properties in certain metal NPs [27, 38]. When a metal particle interacts with an electromagnetic field, the free electrons will collectively oscillate in phase with the incoming light [27]. This is known as surface plasmon resonance (SPR) [39]. Strong scattering and absorption of light by the metal NPs will occur when the frequency of the incident wave becomes resonant with the oscillating electrons [30, 36]. This is the reason for the brilliant colours observed in colloidal solutions containing these metal NPs [36]. Noble metal NPs such as silver (Ag), gold (Au) and copper (Cu) have shown strong plasmon resonances from the visible to near infrared spectral range [26, 40]. The properties of the SPR are dependent on the metal NPs size and shape, interparticle interactions and the surrounding environment [32, 39].

2.1.1 Silver (Ag)

Ag forms part of the noble metals and has a ground state valence electronic configuration of [Kr] $5s^1 4d^{10}$ [41, 42]. Ag is a monovalent metal in that it has a single electron per atom in the conduction band. The d-band which is completely filled lies below the Fermi level [43, 44]. Ag crystallizes in the close-packed face-centred cubic (fcc) structure with a lattice constant of 4.078 Å[37]. With an increase in particle size, the shape of the Ag NPs transition from a icosahedron ($N < 300$) to truncated octahedron ($N \approx 20000$) [27]. For monvalent metals with a fcc crystal structure, the Brillouin zone (BZ) is a polyhedron within which the Fermi surface, which takes up half the volume, will be contained [37, 43]. The Fermi surface of Ag is a distorted sphere which makes contact at the centre of the hexagonal faces of the BZ [41, 44]. Therefore the Fermi surface of Ag is multiply-connected, indicating open orbits [37, 44]. Ag NPs have been integrated into a wide variety of applications due to its unique electrical, optical, catalytic and antibacterial properties [45, 46]. Ag NPs are ideal for the preparation of conductive inks [47, 48] due to its chemical inertness and high conductivity [2]. As described in the previous section, Ag NPs display increased absorption due to the presence of the surface plasmons. Therefore, Ag films have been used for various types of optical sensors, biosensors, as well as surface enhanced Raman scattering [27, 45, 49].

2.1.2 Palladium (Pd)

Palladium is a transition metal that has a atomic electron configuration of [Kr] $5s^0 4d^{10}$ [42, 43]. In the metallic form, a broad conduction band is formed with approximately 0.36 electrons per atom and a narrow d-band with the equivalent number of holes. The Fermi level is positioned at top end of the d-band. [43, 50]. Pd has a close-packed fcc crystal structure with a lattice constant of 3.89 Å[42]. Similarily to the Ag NPs, the shape of the Ag NPs transition from a icosahedron ($N < 100$) to truncated octahedron ($N \approx 6500$) [27]. The Fermi surface of Pd comprises of two hole surfaces and a compensating electron surface [50]. The electron surface centred at Γ is nearly spherical in shape, with bulges extending along [111] and [100] directions. This region will contain the 0.36 electrons per atom. The hole surface forms a sequence of cubic-arranged interconnecting tubes which open along [100] direction. A second hole surface consisting of a small closed region is located at X [44, 50]. Pd NPs have been used as a catalyst for many industrial processes, such as hydrogenation/dehydrogenation reactions, petroleum cracking and catalytic converters

[27, 51]. Pd NPs have the ability to easily absorb hydrogen at room temperature. This has lead to an interest in using Pd films as hydrogen gas detectors [52, 53].

2.2 Metal Nanoparticle Production

There is a particular interest in using metal NPs as the building blocks for new functional materials. The properties of these functional materials are influenced by the interparticle coupling, spatial arrangement and the characteristics of the constituent components [12, 32]. As previously discussed, the properties of the metal NPs are influenced by a set of physical parameters namely, the size, shape and crystal structure. Therefore, metal NPs can be modified in order to possess specific electrical, magnetic, optical and catalytic properties required for a particular application [27, 45]. There are variety of techniques that have been employed for the fabrication of metal NPs which fall into one of two categories; the top-down and bottom-up methods [30, 54]. The decision on which fabrication method should be used will depend on the difficulty, cost and quality of the final product [55]. In this section a brief overview of the most common techniques used for synthesizing metal NPs is given.

2.2.1 Top-Down Methods

Top-down methods involve using external energy to break up solid bulk material into smaller fragments with dimensions in the nanometre range [26, 54, 56]. One way to produce metal NPs is through high-energy ball milling which involves mechanically crushing coarse particles, which are usually in a powder form. A typical ball mill consists of a rotating cylinder and the grinding balls which are either made of a hard steel or ceramic [54, 57]. As the cylinder rotates about it's horizontal axis, the particles will undergo repeated shear deformation due to the crushing and smearing that occurs between the grinding balls and the sides of the cylinder [55, 57]. The advantage of using this method is that it is applicable to large scale NP production as well as being reasonably inexpensive [24, 55]. However, the final product will have a certain amount of surface contamination due to the wearing down of the cylinder and ball materials through the grinding action. Other disadvantages include large size distributions and lack of uniformity in the NP structure [55, 57].

Another top-down method used for the synthesis of nanomaterials is pulsed laser ablation (PLA). In this technique a high powered laser pulse is directed onto the surface of the target

material which can be placed either in a vacuum, gas or liquid [58, 59]. The interaction between the high intensity laser and the surface of the material results in the formation of a luminous ablation plume consisting of the partially ionized material. The system will subsequently undergo a cooling and recombination process which results in the molecules colliding with one another to form NPs [55, 58]. The power density needed to produce the ablation plume will depend on the absorption properties of the sample, laser beam wavelength and the length of time for each pulse [60]. PLA is a relatively straightforward technique in that it only requires a single step to produce the final product which can then be used directly without requiring any further post-processing steps [61]. Another advantage of using this technique is that it allows for large scale production of NPs without the need for specific conditions such as high temperatures and/or pressures, or the use of hazardous chemicals [59, 60]. PLA provides a way to synthesize NPs with high purity and fairly clean surfaces [55], however a drawback to using this technique is that batches of NPs may have a broad size distribution [59].

2.2.2 Bottom-Up Methods

Bottom-up methods involve using atoms or molecules, either in solution or in a gaseous state, as building blocks that assemble to form particles in the nanometre-size range [26, 54, 56]. There is a broad selection of methods used for the bottom up processes which typically fall into two categories: Gas phase methods (vapour phase deposition, spray pyrolysis, etc.); and liquid phase methods (chemical precipitation, sol-gel process, microemulsion, hydrothermal synthesis etc.) [26, 30, 54, 55, 56]. Below a brief discussion will be given on one of the liquid and gas phase methods.

Chemical precipitation is a type of liquid phase synthesis method, which consists primarily of two steps. The first part of this process involves preparing a solution consisting of the metallic compound (*e.g* metal salts, metal oxides, organometallic compounds) dissolved in a solvent [57, 62]. The type of solvent used will depend on the metallic compound, and can range from being polar (*e.g* water, ethanol, methanol) to nonpolar (*e.g* hydrocarbons) [25, 62]. Reducing agents are added to the solution which react with the metallic compounds resulting in the formation of metal atoms [56, 57]. The concentration of metal atoms increases with time until the critical supersaturation point is reached. At this stage nucleation occurs whereby the metal atoms aggregate to form small clusters (i.e. nuclei) [27, 30, 56]. The nuclei rapidly increase in size resulting in the reduction of the concentration of metal atoms

in solution. Nucleation will continue until the concentration of metal atoms falls below the supersaturation minimum [27, 56]. The nuclei continue to grow, provided there is a continuous supply of metal atoms, eventually reaching sizes in the nanometre range [56]. The NPs have highly reactive surfaces, and as such functionalized chemical groups are added directly after nucleation in order to prevent agglomeration [24]. The precipitates are separated from the solution by centrifugation or filtration, washed in order to remove impurities, and then dried at elevated temperatures to form a powder. The second part of this process involves a thermal heat treatment (sintering or annealing) on the metal nanoparticulate powder which will determine the final phase and crystal structure of the particles [62]. The advantage of chemical precipitation is that it allows for a greater degree of control over the particle size, shape and composition [56]. With this method the nanomaterials can be synthesized in a variety of shapes such as rods, cubes, prisms and wires [30, 57]. It is a relatively simple method and suitable for large scale production [30, 56].

Vapour phase deposition methods can be categorized into physical vapour deposition (PVD) and chemical vapour deposition (CVD) [54, 63]. The PVD process involves converting a solid material into the vapour phase through evaporation, while in the presence of an inert gas [63]. The types of sources that can be used for evaporating the solid precursor include sputtering, pulsed laser, thermal energy and electron beams [30, 55]. Through a series of collisions between the evaporated atoms and inert gas molecules, the metal vapour cools down and reaches a supersaturated state [54, 63]. Subsequently, the evaporated metal atoms will undergo homogeneous nucleation and growth thereby forming the metal NPs [30, 55, 63]. The particles are then collected from the walls of the vacuum chamber or substrate [64]. The advantage of PVD is that it can produce high purity samples with very few contaminates due the use of a vacuum environment. PVD allows for a good control over the crystalline structure of the NPs [55, 63]. However, the cost of production can be high due to the intricacy of the equipment needed to create a vacuum environment [63]. In the CVD process, the vapour reactants are transported into the CVD reactor where the molecules are absorbed onto a heated surface. The vapour reactants will undergo thermal decomposition and/or react with other vapours or gases to form stable crystals. The process of deposition involves heterogeneous (on the substrate) and/or homogeneous (in the gas phase) chemical reactions [30, 63]. There are various types of CVD methods such as plasma-assisted CVD, aerosol-assisted CVD and photo-laser CVD, which employ different heating methods to facilitate the deposition reactions [55, 63]. The advantage of using CVD is that it doesn't require as high a vacuum compared to the PVD method, samples can be produced with relatively high purity,

high deposition rates and a wide range of materials can be deposited. The disadvantages of this method is that the precursors need to be volatile near room temperature, and the by-products produced from the reactions can be hazardous [65].

3. Electrical Properties in Disordered Systems

3.1 Percolation Theory

Percolation theory deals with the random placement of geometrical objects in a d-dimensional lattice or continuum [66]. The transport and structural properties of percolation systems depends on these objects forming connections between one another in order to create pathways that spans the system [67].

3.1.1 Lattice Percolation

Two types of lattice percolation can be defined, namely site and bond percolation [68]. If one considers a regular lattice of n-dimensionality space, where each site is randomly occupied with probability p or unoccupied with probability $1 - p$. Two occupied sites are connected if there exists a path consisting of occupied nearest neighbour sites. A cluster of sites is formed through the occupation of neighbouring sites. This is known as site percolation. Bond percolation can be defined in a similar manner. In this case all sites are occupied but the bonds between the sites are randomly occupied with probability q and unoccupied with probability $1 - q$. Similarly, two occupied bonds will belong to the same cluster provided that a path of occupied bonds exists between them. At low concentrations of p (or q), only small isolated clusters will be present in the lattice as shown in figure 3.1a. As the value of p (or q) increases, the clusters will grow in size until a critical concentration is reached. At this point the smaller clusters merge to form one large cluster, also known as an infinite cluster, which consists of occupied sites (or bonds) that span the lattice, as shown in figure 3.1b. This critical concentration is known as the site (or bond) percolation threshold p_{c_s} (or p_{c_b}). Above p_{c_s} (or p_{c_b}) smaller isolated clusters will be incorporated into the infinite cluster thereby increasing its density as shown in figure 3.1c [66, 68, 69, 70].

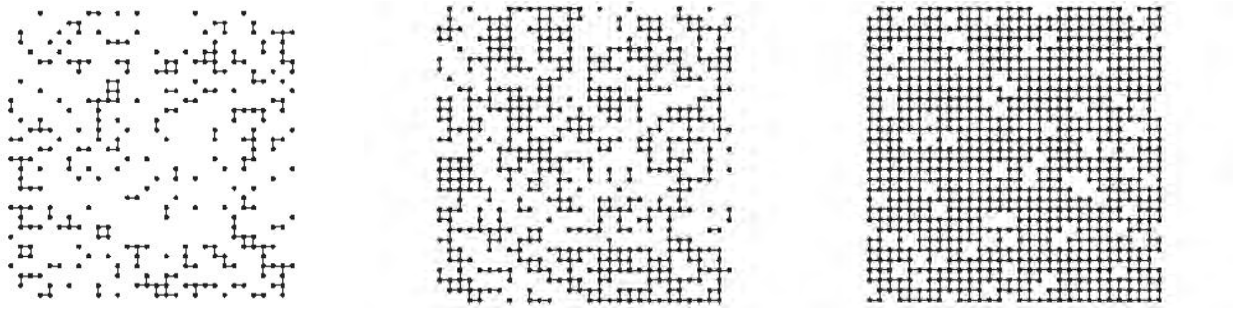

(a) (b) (c)

Fig. 3.1: Diagram illustrating site percolation on a 2-dimensional square lattice for (a) $p < p_{c_s}$, (b) $p = p_{c_s}$ and (c) $p > p_{c_s}$ [71].

The values for p_{c_s} and p_{c_b} have been determined for various 2-dimensional (*e.g* honeycomb, square and triangular) and 3-dimensional lattices (*e.g* diamond, simple cubic, BCC and FCC) [72, 73]. From these calculations it has been observed that the percolation threshold is dependant upon the microscopic features of the lattice i.e. the particular kind of lattice selected and the type of percolation (site or bond) [66, 67, 70]. The occupied and unoccupied sites (or bonds) can represent different objects with specific physical properties (*e.g* conductivity, elasticity, permeability) [67, 70, 74]. For instance, when modelling the fluid permeability in porous materials, the occupied sites will be open to flow while the unoccupied sites are closed to flow [69]. There are a number of properties X of two-phase disordered media that follow a fundamental power law near the percolation threshold. A generalized equation for this power law is given in 3.1 [66, 75],

$$X = S^* \left(p - p_c\right)^j , \tag{3.1}$$

where p is the occupation probability, p_c the percolation threshold, S^* is the proportionality constant for a particular property, and j the critical exponent which controls the behaviour of the properties in the region near to the critical concentration. The critical exponent is universal and depends only on the dimensionality of the system and not on the microstructural detail [15, 67]. The property of universality implies that the critical exponents have the same value for all lattices of the same dimensionality [72].

Random resistor network (RRN) models have been used to describe the electrical conductivity of percolation systems in the region of p_c [76]. If one considers a two-component system where the occupied bonds p represent conductors (*e.g* resistors) with a finite conductivity

σ_1, and unoccupied bonds represents insulators with conductivities equalling to zero. Below p_c, the conductivity of the system σ_m is zero [68, 72]. As p is increased, small clusters of the conducting phase will form throughout the system. The average size of the individual clusters s_{av} increases as more of the conducting phase is added . As the value of p increases above p_c, the system transitions from insulating to conducting. At p_c the infinite cluster forms, at which point the current is able to transverse the system. For values of p just above the critical point, the conductivity will increase gradually. At values of $p >> p_c$ the conductivity will rise sharply until a maximum value is reached at $p = 1$ [20, 72]. The electrical conductivity follows a power law dependence given by [68, 77],

$$\sigma_m = \sigma_1 \left(p - p_c\right)^t, \text{for} \quad p > p_c, \tag{3.2}$$

where t is the critical exponent, p is the fraction of occupied bonds and σ_m, σ_1 and p_c are defined as stated earlier. The value of the critical exponent t for the electrical conductivity σ_m has values ranging between $1.1 - 1.3$ for 2-dimensions, and $1.6 - 2.0$ for 3-dimensions [75, 78]. Equation 3.2 describes the conductivity of the conductor-insulator system for $p > p_c$. For the case where the insulator is replaced with a highly conducting material such as a superconductor, the conductivity of the system will diverge as p_c is approached from below. The conductivity of the superconductor-normal conductor mixture is determined by the properties of the normal conductor [74, 78]. This is described by,

$$\sigma_m = \sigma_2 \left(p_c - p\right)^{-s}, \text{for} \quad p < p_c, \tag{3.3}$$

where σ_2 is the conductivity of the normal conductor. The value of the critical exponent $s = t$ for 2-dimensions and 0.76 for 3-dimensions [72, 77, 78].

3.1.2 Topological Properties of Percolation Structures

It is of interest to know how many objects are needed to form a cluster and at what point these clusters become infinite. Consider the 2D regular lattice described in figure 3.1a, where the fraction of occupied sites p are well below p_c. In this low concentration regime the filled sites form isolated clusters of finite size [72]. The average size of the clusters s_{av} will increase with increasing concentration. s_{av} will remain finite until the concentration approaches p_c, at which point it sharply increases ($s_{av} \to \infty$) [66, 72]. At this point the infinite percolation

cluster forms, thereby transforming the connectivity of the system from short-range to long-range [72, 79]. For concentrations below p_c, s_{av} follows the power law given by equation 3.4, where γ is the critical exponent [15].

$$s_{av} \sim |p_c - p|^{-\gamma} . \tag{3.4}$$

The correlation length ξ is a quantity that characterises the average size of large isolated clusters, both above and below p_c [70, 79]. ξ follows a similar critical behaviour to that of s_{av}, which can be described by,

$$\xi \sim |p - p_c|^{-\upsilon} , \tag{3.5}$$

where the critical exponent is given by υ. ξ will rapidly diverge as p approaches p_c. When p, at low concentrations, is increased toward p_c, neighbouring clusters will coalesce to form larger ones which in turn causes the value of ξ to increase. Above p_c the remaining finite clusters occupy the hole regions inside the infinite cluster. For concentration values where $p > p_c$, the cluster size is reduced and ξ is shown to decrease exponentially in this region. This is due to the remaining isolated clusters being incorporated into the infinite cluster as $p \to 1$ [20, 67, 79]. For any characteristic length scale $L > \xi$, the system will be effectively homogeneous [69, 79]. When $L < \xi$ the percolation system is inhomogeneous and the topological properties depend on L. In this regime both the infinite cluster and the isolated clusters are self-similar [69, 70, 79]. Self-similarity is when sections of the infinite cluster have similar structures at a number of length scales [67, 79].

Above the critical concentration, the system will comprise of a infinite cluster, smaller isolated clusters and unoccupied sites (holes). The probability that a fraction of occupied sites will belong to the infinite cluster is given by the percolation probability P. Therefore, P gives an indication of the change in the volume of the infinite cluster above p_c [15, 66, 72]. P is zero for concentrations below p_c. The behaviour of P just above p_c shows a rapidly rising curve with an infinite slope. P continues to rise sharply as p approaches $p = 1$. This rapid increase in P is due to the formation of the infinite cluster at $p = p_c$, and the incorporation of neighbouring isolated clusters for $p > p_c$. P follows the scaling law,

$$P \sim |p - p_c|^{\beta} , \tag{3.6}$$

where β is the critical exponent [72]. The formation of the infinite cluster causes dramatic changes to the transport properties (*e.g* σ_m) of the system. For concentrations where $p > p_c$, only a certain proportion of the occupied sites (or bonds) that are connected to the infinite cluster will carry an electric current when a voltage is applied across the system. This is known as the backbone of the infinite cluster [67, 69]. The remaining sites (or bonds) that do not not carry any current are dangling clusters known as "dead-ends" which only add to the density of the infinite cluster [79]. Consider the 2D RRN network described in section 3.1.1, and shown in figure 3.2, that has been placed between two electrode plates. The backbone, *i.e* the current-carrying bonds of the infinite cluster is represented by the dark lines, while the dangling clusters are given by the finer lines.

The internal structure of the backbone can be conceptualized using the nodes-links-blobs (NLB) model [78, 80]. According to this model the backbone comprises of several parts; nodes, links and blobs (see figure 3.2). Nodes are particular sites located on the backbone which are linked to at least three different paths. The nodes of the backbone form an irregular superlattice, where the average distance between two neighbouring nodes is ξ [79, 80]. Blobs are regions on the backbone that have multiple connections [69, 78]. Links are singly connected bonds between neighbouring nodes. Links are known as "red bonds" because they will carry the current when a voltage is applied at opposite ends of the infinite cluster. If the red bonds are broken, current will cease to flow through the system. On the other hand, if a bond is broken on a blob the resistance of the system will increase [78, 79, 80]. This model can be used to determine the conductivity and critical exponents of the network [78, 81].

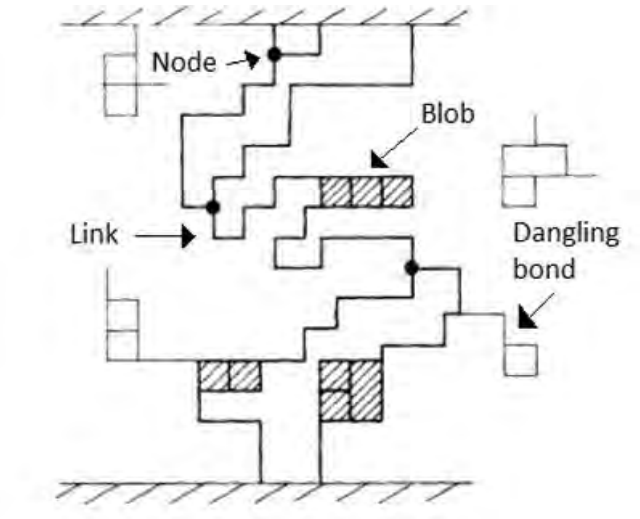

Fig. 3.2: Illustration of the infinite cluster on a 2D square lattice placed between two electrode plates [78].

The conductivity σ_m of the system does not increase rapidly for concentrations just above p_c. Initially when p is increased, the isolated clusters will merge with the infinite cluster. These connections with the infinite cluster may or may not result in forming part of the backbone. If the connection produces a dangling cluster then the overall conductivity of the system is unaffected. If they do form part of the backbone, then new pathways are created for the current to flow which adds to the conductivity of the system [72, 79].

3.1.3 Continuum Percolation

In almost all natural disordered systems, the constituents forming the system are randomly distributed and do not form a regular repeated lattice structure [67, 79]. The critical exponents for various transport properties (*e.g* conductivity, elastic constants) of continuum systems have shown a deviation from the universally accepted values of the discrete lattice models [82, 83]. Due to the complexity of two-phase disordered systems, the critical behaviour is better suited to be described by random continuum models. Scher and Zallen (1970) were able to show a connection between site percolation and the properties of continuum systems [84]. They randomly assigned a volume (or area in 2-dimensions) to each site on the lattice, in this case a sphere with a radius equalling to half the distance between neighbouring sites. The arrangement is such that the neighbouring spheres will touch but

not overlap. The fraction of space taken up by the occupied spheres is given by $\varphi_{cs} = p_c f$, where p is the fraction of occupied spheres and f is the filling factor for the lattice. The critical volume fraction is then given by $\varphi_c = f p_{c_s}$. They found that the value of φ_c was independent of the lattice of the same dimensionality [72, 84]. This model only applies if the constituents of the continuum system fill the media at random, are both spherical, and of similar size [74].

The RRN model mentioned in section 3.1.1 has two states, occupied and unoccupied, with each occupied bond having the same bond "strength" [78, 85]. The non-universal behaviour of the conductivity exponent was shown when the percolating resistor network had a distribution of low-conductance (g) bonds [74, 86]. The distribution of low-conductance bonds of the resistor lattice network is given by the distribution function $h(g)$, where $h(g) \sim g^{-\alpha}$ as $g \to 0$. α lies in the range of $0 < \alpha < 1$ [85]. The non-universal exponent $\bar{t}$ for the conductivity above p_c is given by [74],

$$\bar{t} = \begin{cases} t & \text{if } \alpha < 0 \\ t + \frac{\alpha}{1-\alpha} & \text{if } 0 < \alpha < 1. \end{cases} \tag{3.7}$$

Similarly for a superconductor-normal conductor resistor network the non-universal exponent $\bar{s}$ is given by,

$$\bar{s} = \begin{cases} s & \text{if } \beta < 0 \\ s + \frac{2-\beta}{\beta-1} & \text{if } 1 < \beta < 2. \end{cases} \tag{3.8}$$

The value of t in 2-dimensions is the same as in the discrete lattice model [82]. This distribution of conductances, leading to the non-universal value for the critical exponent is known to occur in the "Swiss-cheese" model (SCM) [81, 86]. The SCM involves placing equally-sized spherical voids at random positions in a homogeneous conducting medium. The spherical voids can overlap with one another. As the concentration of the conductor decreases towards the critical volume fraction, the current is forced to flow through these narrow conducting necks each of which are bounded by three neighbouring voids [74, 78, 85]. The regions with the narrow conducting necks can be represented by a discrete network of resistors [78, 79]. The values of the resistors are dependent on the conducting necks which have a broad distribution of widths δ_N. The value of g corresponding to the width of the necks scales as $g \sim \delta_N^{y+1}$, where $y = \alpha/(1-\alpha)$ [74, 85]. At a critical volume fraction of the voids, the infinite

cluster of the conducting medium will no longer exist and the system is unable to transport current [67, 85]. The conductivity of the percolation continuum system is given by [82, 85],

$$\sigma_m \sim |p - p_c|^{\bar{t}}, \qquad p \geq p_c. \tag{3.9}$$

The SCM can be useful for describing elastic and transport properties of porous media [67]. An extension to the model described above is the inverted SCM. In this case the property of the medium and the voids is rearranged so that the spheres support charge transport but the homogeneous medium in the space between the spheres does not [82]. In a similar manner to the SCM, a discrete lattice network with a distribution of bond "strengths" can be mapped to this system. In this model the centre of the spheres represent the sites while the distance between two neighbouring sites characterize the bonds [85]. There is no change to the critical exponent, t, for the conductivity in the 2- and 3-dimensional cases [82].

Another system that has been suggested to show non-universal behaviour is that of a composite which has a similar arrangement to that of the inverted SCM, where the conducting spheres are embedded in an insulating medium [74, 86]. In this case the conduction mechanism between the conducting particles is controlled by tunnelling. The value of g is given by $g \sim e^{-r/l}$ where r is the radius of the particles. The critical exponent for the conductivity is given by,

$$\bar{t} = t + \left(\frac{a}{l}\right)\left(1 - \frac{l}{a}\right), \tag{3.10}$$

where a is the average nearest distance between two particles and l is the tunnelling distance coefficient [86].

In conclusion, from the few models discussed here, it can be deduced that both universal and non-universal behaviour exists in continuum systems. In these systems the critical transport exponents are related to the parameters of the geometric structure [74], unlike the lattice network models which only depend on the dimensionality of the system. Continuum percolation theory mainly focuses on the connectivity of randomly distributed objects while omitting the more complex behaviour in real continuum systems such as the interparticle charge transport mechanisms and the interaction between the two phases [79].

3.2 Effective Media Theories

Effective media theories (EMT) have been applied to a wide range of inhomogeneous systems to describe the physical properties such as the thermal and electrical conductivity [16] in composites and metal films [87, 88], fluid flow in porous rocks [69] and magnetic permeability in disordered alloys [16]. The Effective medium approximation (EMA) was developed by Bruggeman (1935) and later reinterpreted by Landauer (1952) [14]. Typically an inhomogeneous material (*e.g* composite) will comprise of different constituent phases which can vary in their shape, size and relative orientation which contributes to the randomness of the system. When an external electric field is applied to the material, the properties such as the conductivity, elastic modulus or dielectric function fluctuate within the space [78, 89]. In order to deal with the randomness in the properties, the effective medium model replaces the inhomogeneous medium with an effective uniform medium with properties which closely match those of the inhomogeneous system [69, 90]. Therefore, the effective medium model uses parameters based on the properties of the constituent phases [90].

The EMA can be described by imagining a composite system consisting of a random mixture of metallic and insulating particles with conductivities σ_c and σ_i and volume fraction φ and $1-\varphi$, respectively. The EMA assumes that each particle will be embedded in the uniform effective medium of conductivity σ_m [78, 89]. When an external field E_0 is applied to the effective medium, the field inside the homogeneous medium is uniform [69], but the electric field formed inside each of the constituent particles will in turn cause a deviation in E_0 [14]. In order for the average electric field inside the composite to equal E_0, the total polarization of the two types of particles must equal zero [14, 16]. Assuming the constituent particles are spherical, this will lead to the Bruggeman symmetric effective medium equation [16, 78] for a two-component composite given by,

$$(1-\varphi)\frac{\sigma_i-\sigma_m}{\sigma_i+2\sigma_m}+\varphi\frac{\sigma_c-\sigma_m}{\sigma_c+2\sigma_m}=0. \tag{3.11}$$

The Bruggeman symmetric medium for a two-component composite is illustrated in figure 3.3. In this case the two constituent phases consist of irregularly-shaped grains or particles which have an infinite size range, that are randomly distributed in such a way that the entire medium is filled [87, 91]. Each constituent particle will be in contact with other particles of both phases [92].

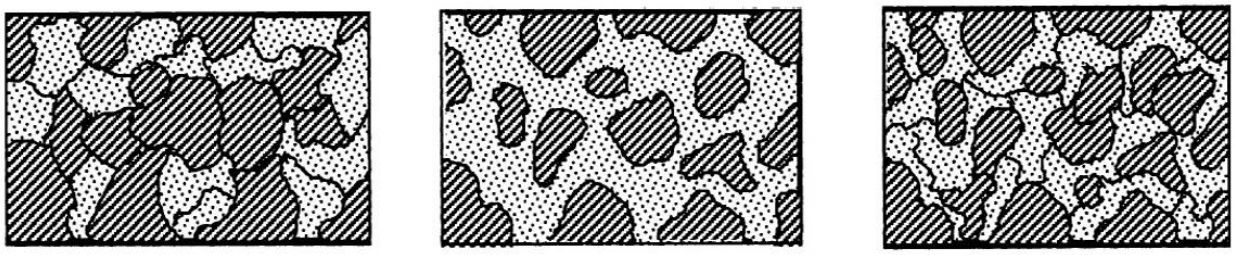

(a) (b) (c)

Fig. 3.3: Visualization of the media showing distributions of two phases with different conductivities: (a) for which the Bruggemans symmetric effective medium, and (b) the Bruggemans asymmetric effective medium theories apply. The distribution shown in (c) is used to describe the GEM (TEPPE) equation [16].

The Bruggeman symmetric medium approximation has two limiting cases [87, 89]. In the first case, which corresponds to a conductor-insulator system, $\sigma_i = 0$ resulting in,

$$\sigma_m = \frac{3}{2}\sigma_c \left(\varphi - \varphi_c\right), \text{for} \quad \varphi > \varphi_c. \tag{3.12}$$

The second case is for a system comprising of a normal metal and superconductor, where $\sigma_c \to \infty$, which leads to,

$$\sigma_m = \frac{1}{3}\sigma_i \left(\varphi_c - \varphi\right)^{-1}, \text{for} \quad \varphi < \varphi_c. \tag{3.13}$$

The Bruggeman EMA predicts a "percolation threshold" of 1/3 indicating a transition from a insulating to conducting phase [68, 78, 93]. The Bruggeman asymmetric medium is illustrated in figure 3.3b. Similarly to Bruggeman symmetric medium, the constituent particles comprising of the two phases will fill the whole composite medium. The difference from the symmetric case is that the constituent particles, of infinite size range, are arranged such that the particles of the one phase will be uniformly surrounded/coated with the other phase [16, 91]. The volume ratio of the uniform coating to the inner core is the same for every particle. In this arrangement there is no conductor-insulator transition as only the phase that coats the particles will be able to percolate [17, 87]. The Bruggeman's asymmetric

equation for a two-component composite is given by [14],

$$\frac{(\sigma_m - \sigma_c)^3}{\sigma_m} = (1-\varphi)^3 \frac{(\sigma_i - \sigma_c)^3}{\sigma_i}. \tag{3.14}$$

The Bruggeman EMT can be extended to other shaped particles *e.g* ellipsoidal [14, 16]. EMT works well for concentrations far from the percolation threshold [68].

3.3 Two-Exponent Phenomenological Percolation Equation (TEPPE)

McLachlan (1987a) has proposed a general effective-media (GEM) equation to describe the conductivity of two-phase media [17, 87]. The GEM equation combines certain aspects from both the Bruggeman effective medium theories and percolation theory in order to describe the conductive behaviour for all volume fractions, including the region near φ_c [87, 88]. The representative medium for which the GEM equation is assumed to be valid is shown in figure 3.3c. In this case the constituent particles are either in contact with the particles of both phases or are completely coated by one phase. This particular scenario is the intermediate between the Bruggeman symmetric and asymmetric media [16, 87]. The GEM equation for a two component system, in terms of the conductivity, is given by,

$$(1-\varphi)\frac{\sigma_i^{1/t} - \sigma_m^{1/t}}{\sigma_i^{1/t} + A\sigma_m^{1/t}} + \varphi\frac{\sigma_c^{1/t} - \sigma_m^{1/t}}{\sigma_c^{1/t} + A\sigma_m^{1/t}} = 0, \tag{3.15}$$

where φ is the volume fraction of the conducting phase, σ_i and σ_c are the conductivities of the insulating and conducting phases and t is the critical exponent. The constant A in equation 3.15 is given by,

$$A = \frac{1-\varphi_c}{\varphi_c}, \tag{3.16}$$

where φ_c is the critical fraction at which the conducting phase forms an infinite cluster [87]. The critical exponent t is related to both φ_c and the shape, orientation and spatial distribution of the constituent particles [16, 17]. The equation given in 3.15 is the general case for an isotropic medium composed of irregularly-shaped particles. The GEM equation

is not derived from any of the models mentioned, but rather a interpolation formula between these equations [87, 94]. The parameters can only be obtained through fitting the GEM equation to experimental data and observing how well it models the system [87].

A limitation to the GEM equation is that it assumes only one critical exponent to describe the scaling behaviour both above and below φ_c, whereas the percolation equations given in 3.2 and 3.3 have distinct exponents for the two regions. As stated in section 3.1.1, $s = t$ for the 2-dimensional case, but for 3-dimensions $s \neq t$. In order for the GEM equation to give an accurate description of the scaling behaviour of the system, it would need to be fitted separately for the two regions [88]. A modified form of the GEM equation has been proposed which introduces a second critical exponent s. This equation, known as the two exponent phenomenological percolation equation (TEPPE) is given by [88, 95],

$$(1-\varphi)\frac{\sigma_i^{1/s} - \sigma_m^{1/s}}{\sigma_i^{1/s} + A\sigma_m^{1/s}} + \varphi\frac{\sigma_c^{1/t} - \sigma_m^{1/t}}{\sigma_c^{1/t} + A\sigma_m^{1/t}} = 0. \tag{3.17}$$

When the critical exponents s and t are equated to 1 and $\varphi_c = 1/3$, equation 3.17 reduces to the Bruggeman symmetric medium equation (equation 3.11). TEPPE takes on the mathematical form of the Bruggeman asymmetric medium equation (equation 3.14) when $\sigma_c \to \infty$ and $\varphi_c = 1$ [93, 95]. Equation 3.17 reduces to the percolation equations given by 3.18 and 3.19 when $\sigma_c \to \infty$, $\sigma_i \to 0$ and $0 < \varphi_c < 1$ [18, 19, 95]:

$$\sigma_m = \sigma_i \left(\frac{\varphi_c}{\varphi_c - \varphi}\right)^s, \text{for} \quad \varphi < \varphi_c, \tag{3.18}$$

$$\sigma_m = \sigma_c \left(\frac{\varphi - \varphi_c}{1 - \varphi_c}\right)^t, \text{for} \quad \varphi > \varphi_c. \tag{3.19}$$

The TEPPE is a smooth interpolation between equation 3.18 and 3.19 when both σ_i and σ_c are finite [81]. The values for the critical exponents in 3-dimensions that have been determined experimentally range between $0.37 < s < 1.28$ and $1 < t < 6.27$ [19], which vary from the widely accepted universal values of $s = 0.87$ and $t = 2$ [81, 83].

3.4 Magneto-transport Properties of Metals

3.4.1 Hall Effect and Magnetoresistance in Bulk Metals

The Hall effect belongs to a group of phenomena known as the galvanomagnetic effects [96]. It was discovered by E.H. Hall in 1879 [97]. The theory of the Hall effect involves describing the motion of a electric charge with a particular velocity, moving under the combined influences of the periodic potential due to the ionic lattice and the force of an externally applied magnetic field [98, 99, 100]. The principle of the Hall effect in metals is shown in figure 3.4.

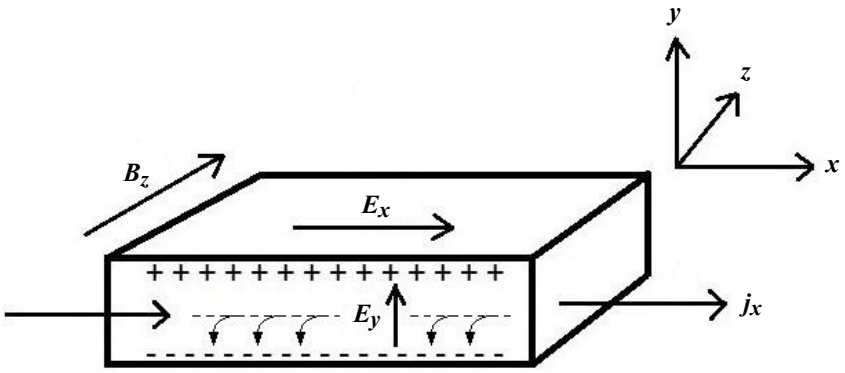

Fig. 3.4: Diagram illustrating the Hall Effect.

The underlying idea of the Hall effect experiment is to measure the steady-state deflection of a current passing through a material when a uniform magnetic field is applied perpendicular to the current flow [101]. Consider the isotropic metal slab shown in figure 3.4 across which an electric field E_x is applied resulting in a electric current density j_x to flow along the specimen in the x-direction. The current density is given by equation 3.20, where n is the concentration of electrons, m is the mass of the electron, e is the electric charge ($-1.6 \times 10^{-19} C$) carried by a single electron and v_x is the electrons drift velocity [44, 102]. The parameter τ known as the relaxation time, is the average time for which an electron can travel before it is scattered

through interactions with phonons and/or impurities [42, 103].

$$j_x = nev_x = \frac{ne^2\tau E_x}{m} \tag{3.20}$$

When a magnetic field B_z is placed perpendicular to the direction of the current flow, the conduction electrons will experience a Lorentz force F_B given by [44, 102],

$$F_B = -ev_xB_z. \tag{3.21}$$

A moving electron that experiences the Lorentz force will follow a path along the Fermi surface defined by the intersection of a plane perpendicular to B_z [43, 98]. The electron will complete a circular orbit provided that no scattering occurs through the interaction with ion cores and other conduction electrons [44, 98]. Therefore the electrons are deflected towards the y-direction along their constant energy orbits, with no net displacement in the x-direction [43, 98]. The frequency of the electrons motion around its orbit is known as the cyclotron frequency ω_c which is given by [99, 100],

$$\omega_c = \frac{eB_z}{mc}, \tag{3.22}$$

where c is the speed of light. Initially, the electrons are deflected in the negative y-direction resulting in a build-up of charge on one side of the sample while at the same time a positive ion surplus is formed on the opposite side [37, 42]. As the positive and negative charges continues to build up on opposite sides of the sample, a transverse electric field E_y is produced across the sample such that it is perpendicular to the direction of j_x and B_z. This is known as the Hall field and is given by [42, 103],

$$E_y = -\omega_c\tau E_x = -\frac{eB_z\tau}{m}E_x. \tag{3.23}$$

Charge will continue to accumulate on opposite sides of the sample until the force due to E_y is large enough to counteract the Lorentz force on each conduction electron [43, 44],

$$eE_y = -ev_xB_z. \tag{3.24}$$

At this point the steady-state is established and any further drift of the electrons in the y-direction is prevented. Therefore the current will again flow in the x-direction without interference from B_z and E_y [44, 98, 103]. By combinding equations 3.20 and 3.24 a relation for v_x in terms of j_x and n is given by,

$$E_y = -\frac{1}{ne} B_z j_x. \tag{3.25}$$

The Hall coefficient given by equation 3.26, is a material parameter that characterises the efficiency of generating an electric field that is perpendicular to both the magnetic field and electric current [101, 104].

$$R_H = -\frac{1}{ne} \tag{3.26}$$

The Hall effect in metals is fairly small compared to semiconductors. This is attributed to metals having a larger carrier density that shows minimal change with temperature, and therefore a small value for v_x. As a result the value of R_H is small [43, 105]. The voltage that is produced by the Hall effect is small and therefore larger magnetic fields are required in order to observe a noticeable signal [106, 107]. The electrical conductivity σ is given by,

$$\sigma = ne\mu, \tag{3.27}$$

where μ is the conductivity mobility which is defined as the electron drift velocity per unit field [102, 106]. This expression is valid provided that Ohm's law is obeyed and σ is independent of the applied electric field [102]. Substituting equation 3.27 into 3.26 one obtains an expression for the Hall mobility μ_H given by,

$$\mu_H = |R_H|\, \sigma. \tag{3.28}$$

In addition to the Hall effect, there are a number of other electrical transport properties that are affected when a uniform magnetic field is applied to a current carrying conductor. One such effect is the change in resistivity ρ which can no longer be represented by a scalar quantity but instead by a tensor (equation 3.29) where the individual components are functions

of the applied magnetic field [44, 98].

$$\rho = \begin{bmatrix} \rho_{xx} & \rho_{xy} & \rho_{xz} \\ \rho_{yx} & \rho_{yy} & \rho_{yz} \\ \rho_{zx} & \rho_{zy} & \rho_{zz} \end{bmatrix} \tag{3.29}$$

The Hall effect in a metal system is associated with $\rho_{yx}(B)$, also known as the Hall resistivity, which is given by [99, 108],

$$\rho_{yx} = \frac{E_y}{j_x} = B_z R_H. \tag{3.30}$$

The changes in ρ in the x-, y- and z-directions are known as the magnetoresistance [101, 106]. There are two types of magnetoresistance that can be measured. When the magnetic field is aligned with the z-direction, as shown in figure 3.4, the resistivity ρ_{ii} of the current flowing along the x- and y-directions will change. This is known as the transverse magnetoresistance and is given by,

$$\frac{\Delta\rho}{\rho(0)} = \frac{\rho_{xx}(B) - \rho_{xx}(0)}{\rho_{xx}(0)}, \tag{3.31}$$

and

$$\frac{\Delta\rho}{\rho(0)} = \frac{\rho_{yy}(B) - \rho_{yy}(0)}{\rho_{yy}(0)}, \tag{3.32}$$

where $\rho_{ii}(0)$ and $\rho_{ii}(B)$ is the electrical resistivity when $B = 0$ and $B \neq 0$, respectively [44, 98]. In the transient state the resistivity of the sample will change due to the Lorentz force and the transverse electrostatic eE_y force acting on the charge carriers [109]. Once the system reaches a steady-state it will resume normal current flow along the x-direction with no further influences from these forces. Therefore in an ideal metal the transverse magnetoresistance is zero [103, 109]. If the magnetic field is aligned parallel to the current flow, then the change in resistivity along the x-direction can be measured. This is known as the longitudinal magnetoresistance and is given by [44, 98],

$$\frac{\Delta\rho}{\rho(0)} = \frac{\rho_{zz}(B) - \rho_{zz}(0)}{\rho_{zz}(0)}. \tag{3.33}$$

In this case the resistivity does not change along the x-direction due to there being no Lorentz force acting on the longitudinal current [103, 109].

3.4.2 Low- and High-Field Galvanomagnetic Properties of Metals

The theory given in section 3.4.1 is based on the free-electron model where it assumes a single carrier type with each electric charge having a constant τ and effective mass m^* [42, 109]. In addition to this the Fermi surface was assumed to have a isotropic spherical shape [109] that allowed only closed electron orbits [14]. This approximation is suitable for simpler metals such as the alkali [110], but not in other metals where there is greater complexity in their zone structure and in the geometry of their Fermi surface [37]. As stated in the previous section, in an ideal metal there is no $\Delta\rho/\rho(0)$ and R_H is a constant which depends on the carrier concentration [44, 103]. The occurrence of $\Delta\rho/\rho(0)$ in more complex metals is due to the distribution of τ and m^* values in the electron gas which leads to a range of carrier drift velocities [103, 109]. As a result the transverse forces acting on the charge carriers will be disproportionate [103, 106]. Therefore the current flowing in the x-direction is reduced and the resistance increases [109]. R_H has shown to have a slight temperature dependence in dilute metal alloys, and the concentration and type of impurity will further affect its behaviour [98, 111, 112].

The galvanomagnetic properties have been experimentally shown to deviate from the ideal behaviour. These properties are sensitive to the sample crystallinity, structure of the Fermi surface, field strength and whether the metal is compensated (equal concentrations of holes and electrons) or not [44, 98, 100]. Under certain conditions the galvanomagnetic properties can provide insight into the electronic structure of the metal [44, 100], as well as the dominant processes (*i.e* scattering) that influence the electrons motion [106]. The galvanomagnetic measurements fall into one of five categories of which three are classical and two are quantal effects [41, 106]. For the purpose of this study only the classical limits are considered. The different regions are defined in terms of $\omega_c\tau$.

In the low-field condition, $\omega_c\tau << 1$, the electron can only transverse a minute fraction of the total cyclotron orbit during its lifetime between collisions [98, 103]. In this condition the scattering processes will dominate the electrons motion compared to the Lorentz force which is a inconsequential perturbation. Therefore the topological features of the electrons orbit are not displayed. The galvanomagnetic properties are dependent on the electrons velocity v,

effective mass m^* and anisotropic relaxation time τ over the Fermi surface [98, 99, 106]. In the classical high-field region, $\omega_c\tau >> 1$, the scattering processes are a negligible perturbation compared to the effect of the Lorentz force on the electrons motion [99, 100, 106]. In this region the electrons lifetime between collision events is longer compared to the time needed to complete a cyclotron orbit [98, 106]. Therefore the electron is able to complete a number of orbits before it is scattered [103]. The galvanomagnetic properties in this region will depend on the geometric features of the Fermi surface [99, 106]. The low-field condition is usually obtained for measurements performed at high temperatures and/or on samples with a large amount of impurities and imperfections [98]. In order to attain the high-field condition, measurements need to be performed at high magnetic fields, very low temperatures in order to minimize the thermal scattering of carriers, and on highly pure samples [99, 100]. Since it is difficult to attain high-field measurements, most experiments at low to intermediate temperatures are carried out in the intermediate-field region where $\omega_c\tau \sim 1$ [98, 106]. In this region the galvanomagnetic properties can be explained by a mixture of both low- and high-field effects [41, 106].

The behaviour of ρ_{yx}, R_H and $\Delta\rho/\rho(0)$ as a function of B-field strength for a polycrystalline metal at a constant temperature is shown in figures 3.5a, 3.5b and 3.5c, respectively. Based on equation 3.30, the value of R_H can be determined from the gradient of the ρ_{yx} *vs.* B graph. In the low-field condition, $\Delta\rho/\rho(0) \propto B^2$ while at the same time $\rho_{yx} \propto B$ which results in R_H remaining constant in this regime [44, 99]. This condition holds for both single and polycrystalline materials [113]. As the system transitions into the intermediate field condition, ρ_{yx} is no longer proportional to the applied field, and as such R_H will increase with increasing B-field. The behaviour of $\Delta\rho/\rho(0)$ and R_H in the high-field region in single crystalline materials is dependent on the type of orbit (open or closed) and whether or not the metal is compensated. In the case of polycrystalline metals, $\Delta\rho/\rho(0) \propto B$ while ρ_{yx} resumes the linear dependence with increasing B-field resulting in R_H remaining constant at high magnetic field strengths [99, 113].

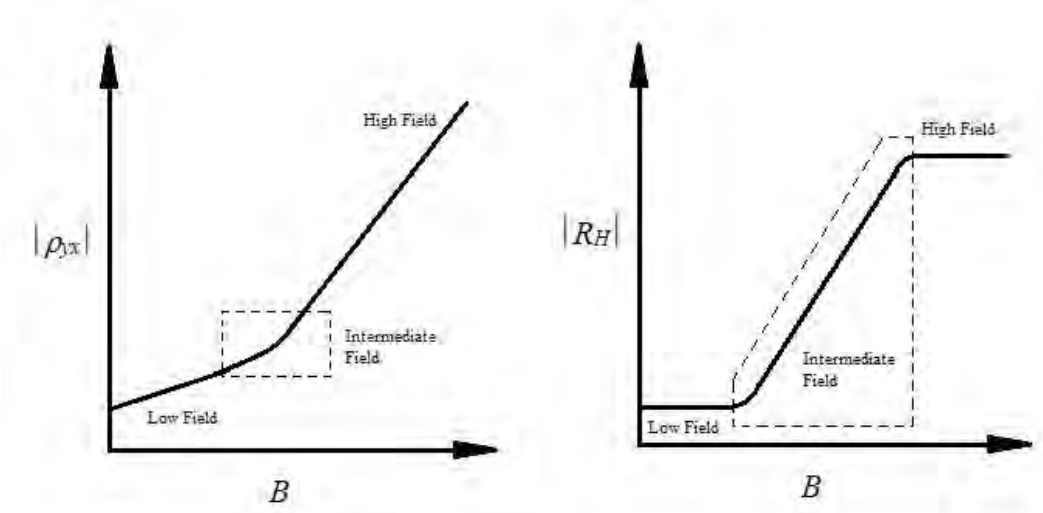

(a) (b)

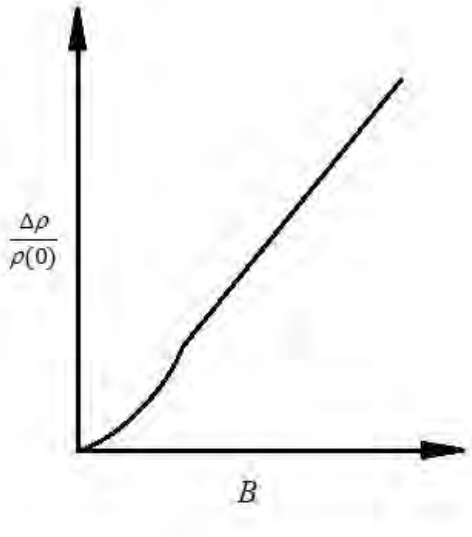

(c)

Fig. 3.5: A representation of the dependence of (a) ρ_{yx}, (b) R_H and (c) $\Delta\rho/\rho(0)$ on the applied magnetic field in a polycrystalline metal when the system approaches the low-field/high-field transition. [113].

4. Experimental Procedure

4.1 Sample Preparation

4.1.1 Materials

The silver (Ag) nanopowder was purchased from Sigma-Aldrich, Steinheim, Germany. The Ag nanoparticles (NPs) had an average particle size ≤ 100 nm as specified by the supplier, and were organically coated with polyvinylpyrrolidone (PVP) which acted as a dispersing agent. The palladium (Pd) nanopowder was supplied by MK_{NANO}, Mississauga, Canada. According to the supplier, the average cluster size of the Pd NPs was 400 nm. The metal NP inks were prepared using ETHOCEL^{TM} ethyl cellulose polymer (The Dow Chemical Company) as a binder and Butyl CELLOSOLVE^{TM} acetate (Dow) as the organic vehicle. ETHOCEL Std.45 polymer was used which contains an ethoxyl content of $48.0 - 49.5\%$ and a viscosity range of $41 - 49$ mPa·s. The ethyl cellulose polymer has a structure of repeating anhydroglucose units, with each unit having three reactive hydroxyl sites. Apart from acting as a binder, ethyl cellulose helps to stabilize the metal NP network and also acts as a rheological modifier [114]. Butyl CELLOSOLVE^{TM} acetate or ethylene glycol n-butyl ether acetate, was used as the solvent due to its slow evaporation rate and low surface tension which helps to improve the adhesion and wetting of the ink to the substrate [115]. In addition to this, a series of acrylic-based inks were prepared in order to compare the screen printing compatibility between solvent- and water-based inks [1]. The water-based inks were prepared using an acrylic emulsion as a binder and reagent grade propan-1, 2-diol (propylene glycol) as a thinner.

4.1.2 Preparation of Nanoparticle Inks

The inks were prepared by dissolving 7wt% of ETHOCEL^{TM} ethyl cellulose polymer in 93wt% of the Butyl CELLOSOLVE^{TM} acetate. The binder solution had a "jelly-like" consistency. The metal nanopowder was added in small increments until all the powder was mixed into the binder solution. In order to investigate the effect of the ink composition on the electrical properties of the printed layers, the metal NPs were mixed with the binder solution in different weight ratios. The metal NP content used in preparing the different inks

in ETHOCEL^{TM} are shown in table 4.1. Upon visual inspection the inks appeared to display viscoelastic behaviour. In order to evaluate the printability of the ink, the contact angle was measured for the different compositions. The contact angles of the inks were measured using the static sessile drop method [116, 117]. A drop of ink was deposited onto a glass slide and a digital image taken of the drop profile using a webcam connected to a computer. The image analysis program, ImageJ, was used to measure the angle between the solid/liquid interface and the liquid/air interface. It was observed that the contact angle was between $25 - 30°$ and that it decreased with decreasing metal particle concentration. Solvent was added to the mixture in order to improve the consistency of the inks and to maintain similar contact angles.

Table 4.1: The particle concentrations used in preparing the metal NP inks.

Material	Binder	Particle Concentration (wt%)
Silver	Ethyl cellulose	35, 40, 42.5, 45, 50, 55, 60, 70
	Acrylic	40, 50, 55, 60, 70
Palladium	Ethyl cellulose	25, 28, 30, 35, 40, 50, 60, 70
	Acrylic	70

The acrylic inks were prepared in a similar manner as above with the metal nanopowder being added in small additions into the acrylic binder. Propylene glycol was added in order to improve the consistency of the ink for printing. The water-based inks comprised of a series of Ag inks and a Pd ink with particle concentrations shown in table 4.1. The contact angle of the inks were measured using the same method as above. The value was found to be between $22.5 - 44°$ for the Ag inks and $36.25°$ for the Pd ink.

4.1.3 Screen Printing

The metallic inks were printed using an ATMA AT-60PD semi-automatic flatbed screen printer shown in figure 4.1a [118]. Screens made from SEFAR monofilament polyester fibre with a mesh count of 150 lines/cm and thread diameter of 31μm (supplied by Register Screens (Pty) Ltd), were used for printing. During the production process of the screen, woven polyester mesh is stretched and glued to an aluminium frame while being held under tension [119]. A photopolymeric emulsion that is sensitive to ultra violet (UV) light is applied to both sides of the screen. A transparency with the intended design (film positive) is placed onto the screen which is then exposed to a UV light source. The areas that are exposed to

light become hardened whereas the unexposed areas with the stencil design are impervious to light and remains soft. The unexposed areas are washed off leaving them open to ink flow [119, 120]. These areas are indicated by the yellow features on the screen mounted in the screen printing equipment as shown in figure 4.1a.

(a)

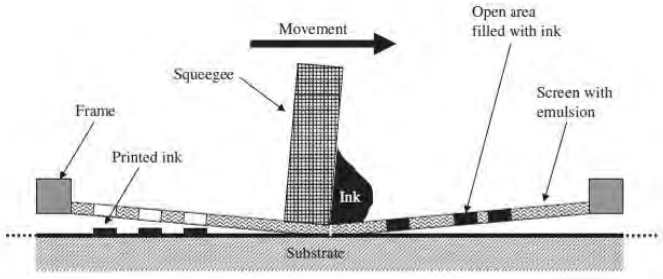

(b)

Fig. 4.1: (a) Photograph of the ATMA AT-60PD semi-automatic flatbed screen printer with mounted screen. (b) Schematic of the screen printing process [121].

As illustrated in figure 4.1b, during a print cycle, the ink is placed onto the screen in front of the squeegee. The squeegee is pressed downward onto the screen with a particular force

causing the screen to deform thereby bringing it into contact with the substrate [121, 122]. The ink is forced to flow through the open areas onto the substrate as the squeegee is drawn horizontally across the screen [2, 121]. The ink will adhere to the substrate as soon as contact is made. Immediately after the squeegee has moved over the region the screen mesh will lift away from the substrate leaving behind the ink pattern [123]. After one printing stroke the floodbar pushes the remaining ink in the opposite direction to that of the squeegee's movement, but with less pressure, so that the ink is at the initial position. A polyurethane squeegee with a hardness of 70 Shore A was used for printing. The double stroke print mode was used in order to ensure a uniform layer with good coverage. The printed samples were 1×1 cm^2 in area with a layer thickness of approximately $10 - 15\mu$m which was observed from microscopy. For all samples, plain white 80 gsm paper, with no pre-treatment, was used as the substrate. On average, each ink produces $15 - 20$ prints with 8 devices per print that was available for characterization. The prints were allowed to dry under ambient conditions for a minimum of 48 hours before any tests were performed.

4.2 Structural Characterisation of the Metal Nanoparticles

The shape, size and crystallinity of the metal nanopowders were observed using Transmission Electron Microscopy (TEM) in the bright field mode. A spatula tip of the metal powder was placed into a microtube 2/3 filled with ethanol. The NPs were dispersed in the solution by placing the microtube into a sonicating waterbath at room temperature for approximately 15 minutes. An aliquote of the solution was taken using a micropipette and placed onto a carbon coated copper grid. The grids were allowed to dry for 20 minutes before inserting into the TEM. The metal NPs were observed using a JEOL JEM-2100 TEM with a Lanthanum Hexaboride (LaB_6) cathode filament and an acceleration voltage of 200 kV.

4.3 Structural Characterisation of the Printed Layers

The surface and nanoparticle microstructure of the printed layers was imaged using Scanning Electron Microscopy (SEM). The samples were cut into 1×1 cm^2 squares and placed onto a stub coated with carbon adhesive tape. These samples were imaged using the FEI HELIOS

NanoLab 650 and the FEI Nova NanoSEM 230 operating in the secondary and backscattered electron imaging modes. Cross sections of the printed layers were prepared using Argon (Ar) ion beam polishing and focused ion beam (FIB) milling. These techniques involve the removal of material from the sample surface in order to view the microstructural cross section. The basic operation principle involves bombarding the target area of a specimen with accelerated ions resulting in the surface atoms being ejected. This process is known as sputtering. When an ion impacts on a surface it will penetrate the solid provided that it has sufficient energy to overcome the repulsive energy barrier formed by the surface atoms [124]. As the ion penetrates the solid it is deflected and will lose kinetic energy along the way through elastic and inelastic interactions with the atoms of the solid [125]. Elastic collisions result in the transfer of kinetic energy of the ion to the target atoms which can result in the displacement of the atoms from their equilibrium positions [126]. This can in turn cause further displacement resulting in a cascading effect which eventually leads to sputtering of the atoms near the surface [124, 125]. The ion will continue to undergo a series of collisions and deflections until its kinetic energy is insufficient to overcome the internal energy barriers at which point the ion will come to a rest [124]. Inelastic collisions produce secondary electrons, ionization and electromagnetic radiation [126]. Ar^+ ion beam polishing is advantageous in that large cross sections can be obtained with minimal distortion of the polished surface. The disadvantage of using this technique is that it requires a longer time to prepare a sample compared to the FIB, and preferential thinning will occur in composite materials whose individual components have different hardnesses [127]. FIB milling is a fast and reliable technique that can produce samples within $2 - 4$ hours, and allows for precise cutting of the target area. The disadvantages of this technique is due to ion implantation, damage caused by the Ga^+ ion beam, and the limited size of the cross sections [128].

4.3.1 Argon Ion Beam Polishing

The cross sections of the printed metal layers were prepared for SEM observation, with a JEOL SM-09020CP cross section polisher. Samples were cut into 0.5×0.5 cm^2 squares and placed between two glass slides with epoxy resin. The resin was cured at 141°C for approximately 5 minutes. The samples were cut to size using a diamond cutter in order to fit into the $11(\mathrm{W}) \times 10(\mathrm{L}) \times 2(\mathrm{T})$ mm^3 sample holder. The sample was mounted into the polisher with a shielding plate positioned directly above the sample surface in such a way that the target area was left exposed. The chamber was evacuated and a broad Ar^+ ion

beam with a diameter of 500 μm was used to irradiate from above the shielding plate onto the unmasked area of the sample. The shielding plate protects a portion of the sample from the abrasive Ar^+ ion beam while leaving the unmasked region to be milled [129, 130]. This resulted in producing a polished cross section that was parallel to the flat cross section of the shielding plate [131]. Figure 4.2 shows an illustration of the principle of the cross section polisher. The Ar^+ ion beam had an accelerating voltage of between $2-6$ kV and a milling speed of 100 μm/h. The sample holder was swung at $\pm 30^\circ$ around a axis perpendicular to sample cross section in order to ensure uniform milling [132] and prevent beam striations due to variation in the hardness of the composite materials [127]. The samples were then placed onto a stub and coated with a $10-15$ nm layer of carbon. The samples were observed with a JEOL JSM-7100F Analytical Field Emission SEM.

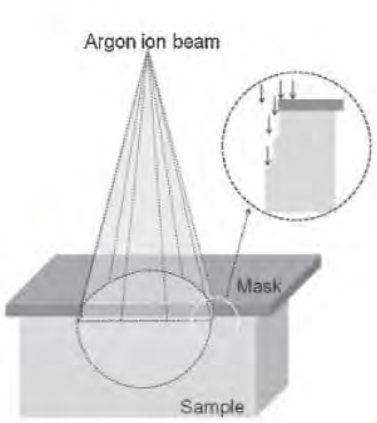

Fig. 4.2: Illustration showing the principle of cross section polisher [132]

4.3.2 Focused Ion Beam Milling

Cross sections for TEM imaging were prepared using FIB milling. SEM imaging and cross section preparation were carried out on a FEI Helios NanoLab 650 DualBeam^{TM} FIB/SEM system. The instrument is equipped with a Tomahawk ion column which uses a gallium (Ga) liquid metal ion source and a Elstar^{TM} field emission SEM (FESEM). The FIB ion column has a similar arrangement and operation to that of the SEM in that a focused beam of charged particles is rastered over the specimen in order to generate signals for imaging. The

difference is that the FIB uses a Ga^+ ion beam instead of an electron beam [133, 134]. The Ga liquid metal ion source (LMIS) consists of a Ga reservoir connected to a tungsten needle [125]. During operation, the Ga will flow from the reservoir towards the tip of the tungsten needle which sits above the extractor [126, 135]. A strong electric field is applied to the needle tip which ionizes the Ga [135] resulting in the formation of a liquid Ga cone [136]. Ga^+ ions are emitted from the liquid Ga cone and accelerated down the FIB column towards the sample. The extracted Ga^+ ions are replenished by the continuous flow of liquid Ga towards the tip, thus ensuring a constant ion current [125]. The FIB Ga^+ ion beam operates at a voltage between $500V - 30kV$, with beam currents varying between $0.1pA - 65nA$. The FIB is equipped with a gas injection system (GIS) which allows for the deposition of metals (W, Al, Pt and carbon) and insulators onto the sample surface via FIB assisted chemical vapour deposition (FIB-CVD). The precursor gas containing the element intended to be deposited, is injected from a nozzle onto the target area of the sample where it is absorbed on the surface [128]. The Ga^+ ion beam is rastered over the deposited layer which causes the gas to decompose [134]. The volatile by-product is desorbed from surface and removed through the vacuum system while the desired product remains on the surface forming a thin film [136]. When the ion beam rasters over the sample surface a number of secondary particles (electrons, neutral atoms and ions) are emitted [126]. Secondary electrons are used for imaging during the milling procedure.

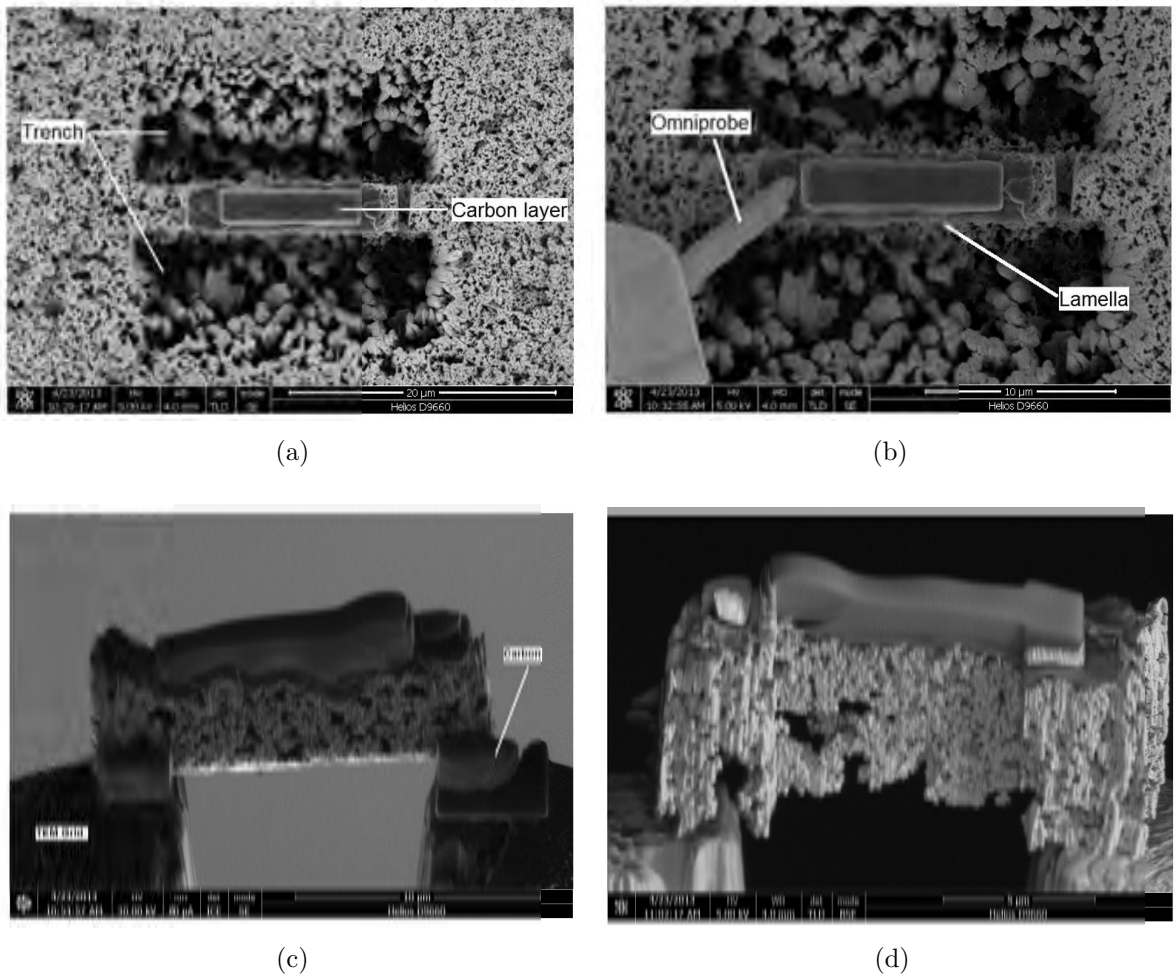

Fig. 4.3: Series of SE and BSE images showing the steps during the lamella preparation. (a) Trenches milled on either side of the protective carbon layer, (b) Omniprobe tip welded to the lamella, (c) lamella mounted onto the TEM half grid, and (d) milling of lamella.

The printed layers were cut into 1×1 cm^2 squares and placed onto a FIB sample holder with carbon tape. The TEM samples were prepared using the *in situ* lift-out technique [125]. This technique involves removing a thin slice (lamella) from the bulk sample via a nanomanipulator and transferring it to a TEM half grid. This is followed with additional milling and thinning in order to achieve an electron transparent lamella required for TEM analysis [125, 137]. Figure 4.3 shows the steps taken to prepare the thin lamella. Prior to the start of milling a strip of carbon with a layer thickness of 2 μm and area of 1×1 cm^2, was deposited onto the target area in order to protect the top surface from damage and spurious sputtering during milling [134]. Trenches were milled on either side of the carbon strip using a high Ga^+ ion beam current (figure 4.3a). One side of the lamella was cut free from the

trench walls with the ion beam. During the "lift-out" stage, the Omniprobe tip was welded to the detached edge of the lamella by depositing carbon along the contact region (figure 4.3b). The sample was tilted at a 45° angle relative to the ion beam and the base and remaining side of the lamella was cut free. The lamella was then lifted out with the Omniprobe and mounted onto a TEM half grid by depositing carbon between the sample and surface of the grid (figure 4.3c). The bridge between the Omniprobe tip and lamella was cut off using the ion beam. The lamella was then milled, alternating sides after each milling step (figure 4.3d). Milling was continued until the sample thickness was approximately 100 nm. The printed layers showed a high degree of porosity which was as a result of the solvent ($27.9 - 69.75$wt% of the ink) evaporating and leaving behind voids between the NP network. The porosity was further compounded during the milling and polishing steps due to preferential etching in the regions where the voids are present. In order to reduce this the sides of the lamella were coated with carbon before each milling step in order to fill the voids within the layer and maintain the structural integrity of the NP microstructure. A weaker beam with a voltage of 5 kV and current of 1.6 nA, was used in the final polishing steps in order to minimize damage and deformation of the sample. High resolution TEM imaging was performed on a JEOL JEM-ARM 200F operating in the bright field mode at 200 kV. Electron diffraction analysis were performed on selected areas of the TEM samples.

4.4 Electrical Characterisation

The electrical transport properties of the printed layers were characterised using impedance spectroscopy and Hall Effect measurements. Information about the conductivity, mobility, carrier concentration and carrier type can be determined directly from Hall effect measurements. Impedance spectroscopy is useful in separating out electrical responses (interfacial capacitance, charge transfer resistance) from various nanostructural features (grain boundaries, interfaces between particles) found in the system [54].

4.4.1 Hall Effect Measurements

The magneto-transport properties of the printed metal layers were measured using the LakeShore 75013 SCSM Hall Effect Measurement System (HMS). A schematic of the experimental set-up is shown in Figure 4.4 [138]. The main components of the system are the

sample module (Lake Shore 75013 SCSM), electromagnet, computer and instrumentation console which included the magnet power supply (Lake Shore 642). The electromagnet that was used has a 4 inch-pole diameter with a maximum magnetic flux density of 1.04 Tesla. A precision current source (Keithley 6220) which is capable of supplying a constant *dc* current from between 0.1 fA to 105 mA was used. Current and voltage measurements were performed with a picoammeter (Keithley 6485) and nanovoltmeter (Keithley 2182A). A digital signal processing (DSP) gaussmeter (475, Lake Shore) was used to measure the magnetic field. The HMS has fully integrated software that controls the operation of the individual instruments as well as the magnetic flux density during data acquisition. The system is capable of measuring resistance, Hall voltage, magnetoresistance and current-voltage curves [138].

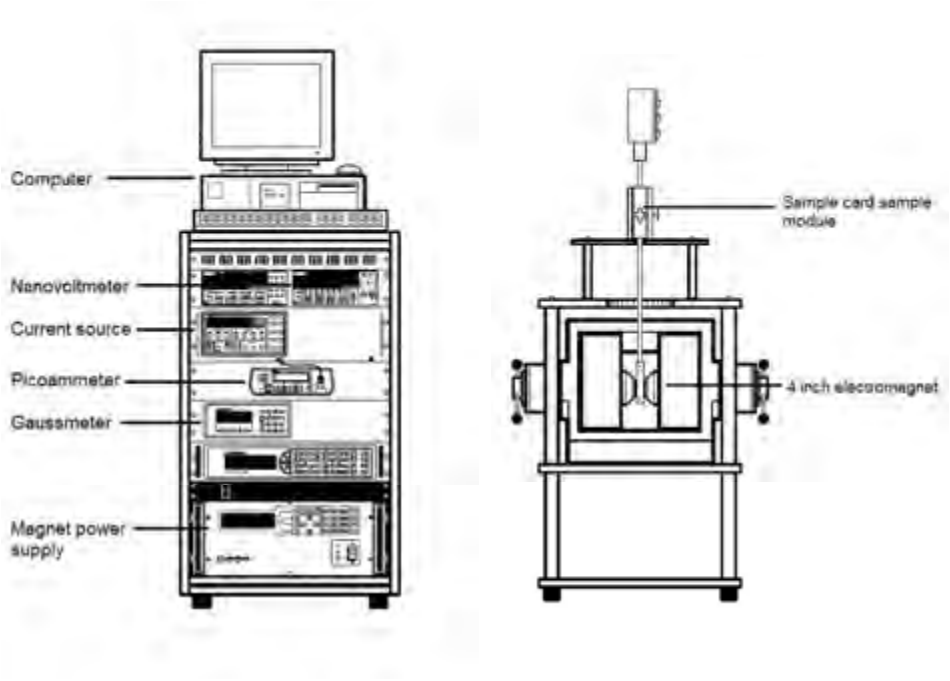

(a) (b)

Fig. 4.4: Illustration of the LakeShore 75013 SCSM Hall Effect measurement system. (a) Computer and instrument console and (b) electromagnet and sample card module [138]

The resistivity and Hall effect measurements were performed in the van der Pauw geometry. This technique can be used on any arbitrarily shaped sample provided that it is a homogenous, isotropic material that is flat and of uniform thickness [104, 139]. The dimensions of the probes need to be sufficiently small compared to the peripheral length of the sample.

The four probes can be placed randomly along the sample, however, they do need to be placed as near to the edge as possible [139]. Figure 4.5 shows the configuration for measuring the resistivity and Hall voltage in the van der Pauw geometry. In both cases current is forced through the sample, either with or without a magnetic field applied perpendicularly to the sample, and the corresponding voltage is measured. For resistivity measurements the current is forced through adjacent terminals (eg, 1 and 2) and the voltage measured across the opposite adjacent terminals (eq. 3 and 4). Hall effect measurements are performed by forcing current through the two diagonally opposite terminals (eg. 1 and 3) and the voltage measured on the other opposite terminals (eg. 2 and 4). Both the polarity of the field and current were reversed in order to improve the accuracy of the results and to eliminate large offset voltages caused by variation in the sample temperature and non-symmetric placement of the contacts [140, 141].

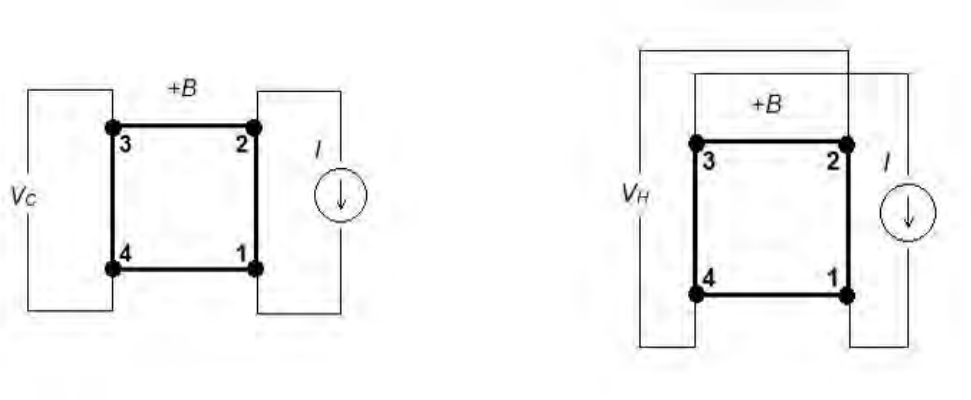

(a) (b)

Fig. 4.5: Measurement configuration for the (a) resistivity and (b) Hall voltage in the van der Pauw geometry.

The Hall software [138] first calculates two resistivities, ρ_A and ρ_B, given by equations 4.1 and 4.2 respectively:

$$\rho_A = \frac{\pi f_A t}{\ln(2)} \left\{ \frac{V^+_{12,43} - V^-_{12,43} + V^+_{23,14} - V^-_{23,14}}{I^+_{12} - I^-_{12} + I^+_{23} - I^-_{23}} \right\}, \tag{4.1}$$

and

$$\rho_A = \frac{\pi f_B t}{\ln(2)} \left\{ \frac{V^+_{34,21} - V^-_{34,21} + V^+_{41,23} - V^-_{41,23}}{I^+_{34} - I^-_{34} + I^+_{41} - I^-_{41}} \right\}. \tag{4.2}$$

V^+_{ijkl} is the voltage measured across terminals k and l, with k being positive, while a positive

current flows into terminals i and j. The resistance R^{+}_{ijkl} is given by V_{kl}/I_{ij} which is the voltage measured across terminals k and l, while a positive current flows into i and out of j. The units for voltage are in volts, current in amperes and the thickness t in meters. f_A and f_B are geometrical factors that are a function of the resistance ratios Q_A and Q_B given by equations 4.3 and 4.4 respectively:

$$Q_A = \left(\frac{R^{+}_{12,43} - R^{-}_{12,43}}{R^{+}_{23,14} - R^{-}_{23,14}}\right) = \left(\frac{V^{+}_{12,43} - V^{-}_{12,43}}{I^{+}_{12} - I^{-}_{12}}\right)\left(\frac{I^{+}_{23} - I^{-}_{23}}{V^{+}_{23,14} - V^{-}_{23,14}}\right), \tag{4.3}$$

and

$$Q_B = \left(\frac{R^{+}_{34,21} - R^{-}_{34,21}}{R^{+}_{41,23} - R^{-}_{41,23}}\right) = \left(\frac{V^{+}_{34,21} - V^{-}_{34,21}}{I^{+}_{34} - I^{-}_{34}}\right)\left(\frac{I^{+}_{41} - I^{-}_{41}}{V^{+}_{41,23} - V^{-}_{41,23}}\right). \tag{4.4}$$

If the values of Q_A or Q_B are greater than 1, then the reciprocal is taken instead. The relationship between f and Q is given by,

$$\frac{Q-1}{Q+1} = \frac{f}{\ln(2)}\cosh^{-1}\left\{\frac{1}{2}\exp\left[\frac{\ln(2)}{f}\right]\right\}. \tag{4.5}$$

If the values for ρ_A and ρ_B are not within $\pm$ 10% then the sample may be too inhomogeneous to be analysed using this method. If there is agreement then the average resistivity is given by,

$$\rho_{av} = \frac{\rho_A + \rho_B}{2}. \tag{4.6}$$

The resistivity at different field strengths was measured and calculated using the above method in order to obtain the average magnetoresistivity $\rho_{av}(B)$ at each field point. The Hall coefficient was determined in a similar way to the zero-field resistivity in that two initial values, R_{HC} and R_{HD}, were calculated using equations 4.7 and 4.8 respectively:

$$R_{HC} = \frac{t}{B}\frac{V^{+}_{31,42}(+B) - V^{-}_{31,42}(+B) + V^{-}_{31,42}(-B) - V^{+}_{31,42}(-B)}{I^{+}_{31}(+B) - I^{-}_{31}(+B) + I^{-}_{31}(-B) - I^{+}_{31}(-B)}, \tag{4.7}$$

and

$$R_{HD} = \frac{t}{B}\frac{V^{+}_{42,13}(+B) - V^{-}_{42,13}(+B) + V^{-}_{42,13}(-B) - V^{+}_{42,13}(-B)}{I^{+}_{42}(+B) - I^{-}_{42}(+B) + I^{-}_{42}(-B) - I^{+}_{42}(-B)}. \tag{4.8}$$

If the values of R_{HC} and R_{HD} agree within $\pm$ 10% then the average Hall coefficient is given

by,

$$R_{Hav} = \frac{R_{HC} + R_{HD}}{2}. \tag{4.9}$$

The Hall mobility was calculated using equation 4.10, where ρ_{av} is the either the zero-field resistivity or the magnetoresistivity, depending on the type of measurement,

$$\mu_H = \frac{|R_{Hav}|}{\rho_{av}}. \tag{4.10}$$

A sample of 1×1 cm^2 in size was placed in the centre of the sample card and electrical contact was made with tungsten needle probes placed at the four corners (figure 4.6). The sample card has 20 gold plated fingers which align with the card edge connector found at the bottom end of the sample module. The sample card was inserted into the card edge connector and a dark cover placed over it. This was performed in order to ensure that no light induced effects would occur during the measurement. The sample module was positioned such that the sample card lies between the poles of the 1 T magnet. The distance between the magnet poles was kept at 4 cm throughout the experiments. The quality of each of the four contacts was assessed by measuring the I-V curves at zero magnetic field between two pairs of contacts (R13, 13 and R24, 24). At least two pairs of contacts need to show ohmic behaviour in order for the sample to be acceptable for Hall effect measurements. Variable magnetic-field Hall measurements were performed at an average ambient temperature of 18°C. The sheet resistivity (ρ_s) was determined for the zero field point. In order for the measured values of ρ_s to be valid, the ASTM compliance check for the van der Pauw sample was performed. Therefore the sample should have a thickness that is less than 1 mm and a length that is greater than 15 times its thickness [138].

Fig. 4.6: Photograph of the sample card used for the Hall Effect measurements.

4.4.2 Impedance Spectroscopy

The measurement of the impedance (Z) of the printed layers and it's phase angle (θ) were carried out using a Hewlett-Packard Model 4192A Low Frequency (LF) Impedance Analyser (Agilent Technologies, USA) shown in figure 4.7a. The experimental set-up comprised of the impedance analyser connected to a personnel computer equipped with data acquisition software developed in LabVIEW, and an interface cable. The samples were cut into 1×1 cm^2 squares and placed onto a sample holder shown in figure 4.7b, which was specially designed and constructed for this work. The probes were attached to the clamps found on the test fixture. Data was collected across a frequency range of 5 Hz $-$ 13 MHz with a frequency step size of 1500 Hz. The measurement range of |Z| and θ is 0.0001 Ω to 1.2999 MΩ and -180° to +180° respectively. Both |Z| and θ have a basic accuracy of 0.1% [142]. Due to the limitations of the machine, samples with impedances greater than 1.3 MΩ were unable to be measured. Therefore, impedance measurements were restricted to particle loadings that were above or in the region of the percolation threshold. All impedance measurements were performed under ambient conditions.

(a)

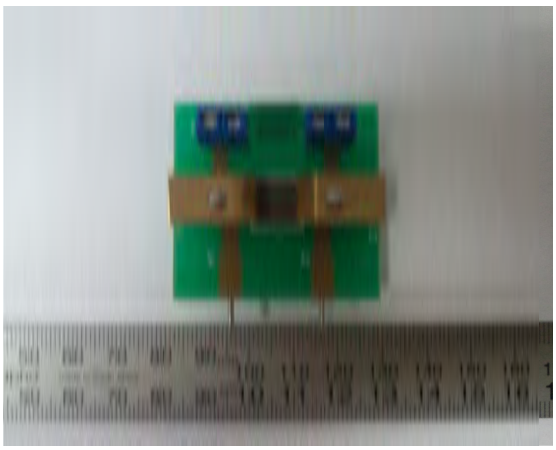

(b)

Fig. 4.7: (a)Hewlett-Packard (Model 4192) LF Impedance analyser. (b) Sample holder.

5. Results and Analysis

5.1 Morphological Characterisation

5.1.1 Morphology of the Metal Nanoparticles

Low-magnification TEM micrographs of the silver (Ag) (figure 5.1a) and palladium (Pd) NPs (figure 5.2a) show both metals to be polydispersed with average particle sizes varying between $20-50$ nm for the Ag NPs and $50-100$ nm for the Pd NPs. The shape of the Ag NPs tends to be more spherical or slightly elongated, whereas the Pd NPs are faceted. HRTEM images shown in figure 5.1b and 5.2b show a series of fine parallel lines known as lattice fringes which extend to the edge of the particles. The lattice fringes are a result of the incident electron beam being diffracted by rows of atoms that repeat periodically, but are differently orientated over various regions in the sample [143, 144]. The presence of the lattice fringes indicates crystallinity in both metals. The spacing between the fringes can be measured provided that the image is of a high enough resolution [145]. Alternatively, the diffraction pattern can be analysed which provides information about the crystal structure and lattice constants [144]. As stated in section 4.3.2, one requirement for HRTEM measurements is that the area being analysed needs to be electron transparent. Electron diffraction analysis was performed using the HRTEM and will be discussed in the following section.

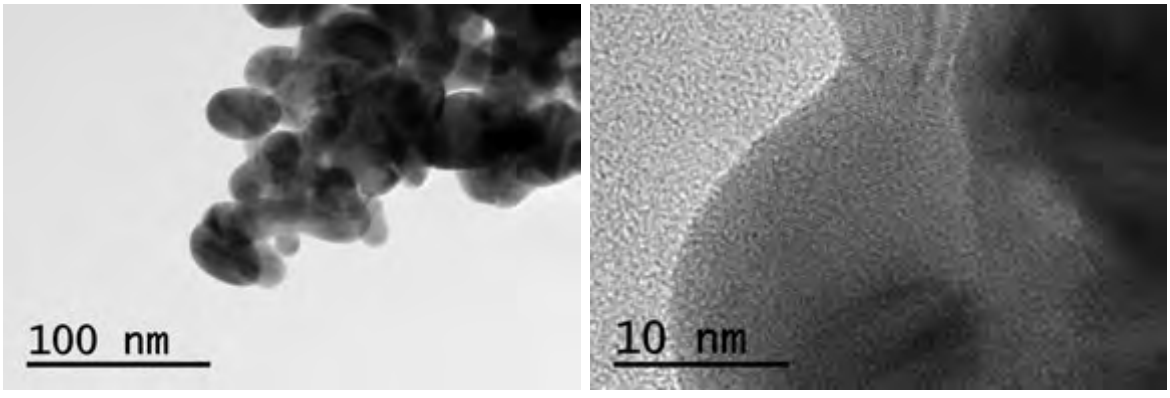

(a) (b)

Fig. 5.1: (a) TEM micrograph of the Ag NPs. (b) HRTEM micrograph of the Ag NPs showing lattice fringes.

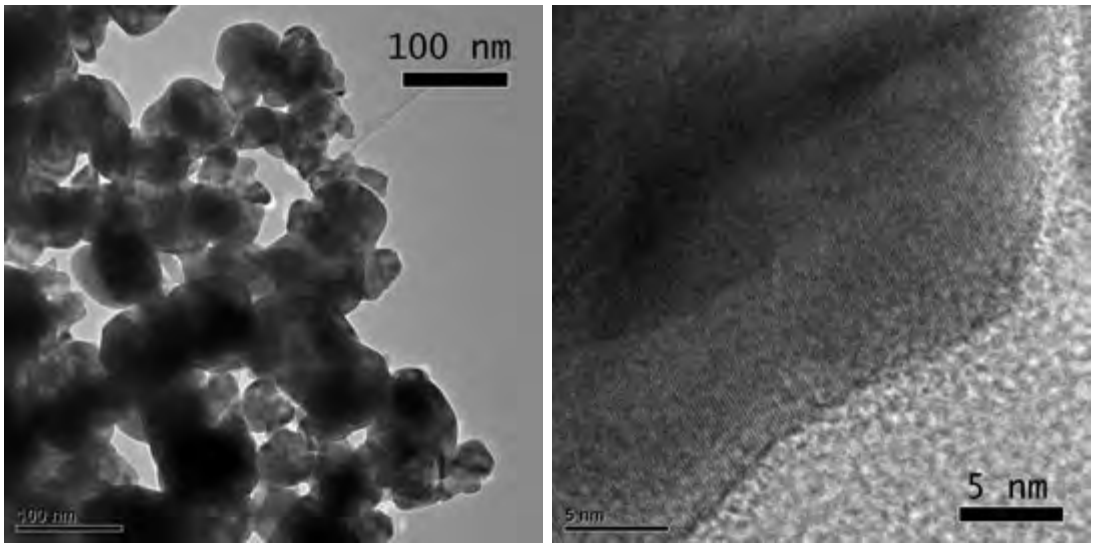

(a) (b)

Fig. 5.2: (a) TEM micrograph of the Pd NPs. (b) HRTEM micrograph of the Pd NPs showing lattice fringes.

5.1.2 Morphology of the Printed Layers

Figure 5.3a and 5.3b shows the top surface SEM micrographs of the printed layers containing 70wt% Ag and 70wt% Pd, respectively, in the acrylic binder. The Ag acrylic ink displayed good printability producing a homogeneous layer consisting of NP clusters of varying size that are densely packed together. The layer resembles a "cauliflower" structure. In comparison, the Pd ink with the same particle concentration and the same binder produced a layer which sparsely covered the substrate with small NP clusters. The paper fibres indicated by the white arrows in figure 5.3b, can be seen to protrude through the nanoparticulate layer. This indicates that only a small amount of the NPs were deposited during the printing process. The poor printability of the Pd ink can be attributed to the phase separation of the NPs from the liquid vehicle that was observed during the preparation of the ink. In the printing process, when the ink was placed onto the screen, the solvent would appear on the rim of the ink. As a result it can be assumed that the part of the ink with a higher amount of Pd NPs would dry faster than that containing more solvent, causing the NPs to coalesce. Therefore after one printing stroke of the squeegee, there is only a thin layer of Pd NPs which remains at the open stencil area.

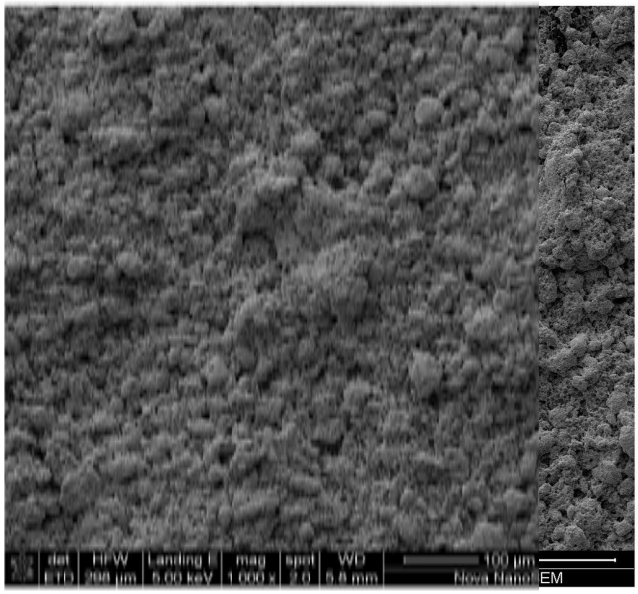

(a)

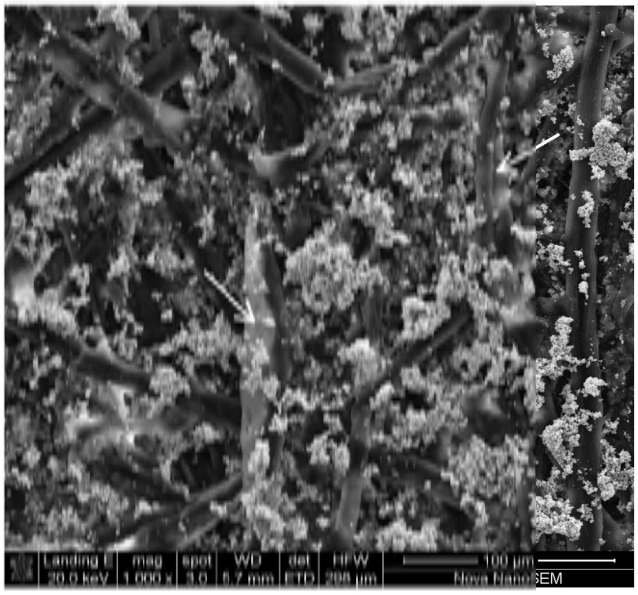

(b)

Fig. 5.3: Secondary electron (SE) images showing the surface of the printed (a) Ag and (b) Pd layers in acrylic binder, containing a particle loading of 70 wt%. The arrows in (b) indicate the paper fibres.

Figure 5.4 and 5.5 shows the top surface SEM micrographs of the printed Pd and Ag layers using ETHOCEL^{TM} as binder, at two different particle weight fractions. At a particle loading of 35wt% Ag (figure 5.4a), the particles agglomerate to form dense isolated clusters that are dispersed over the substrate. At this low particle loading the Ag clusters vary in size. In contrast it can clearly be seen that the aggregation of the Pd NPs is structurally different to that of the Ag NPs in that they form "chain-like" structures. This is observed at a particle loading of 25wt% Pd (figure 5.5a), where the Pd NPs aggregate to form chains of particles that extend over the paper fibres. In both cases at low particle loadings, the printed layers show poor coverage with paper fibres indicated by the arrows in 5.4a and 5.5a, seen to protrude through the layer. As the particle loading of Ag is increased to 70wt%, neighbouring smaller clusters are incorporated into larger ones forming an almost uniform layer (figure 5.4b). In the case of the Pd layer at a particle loading of 70wt%, the chains coalesce to form a more compact structure (figure 5.5b) which has a high degree of porosity.

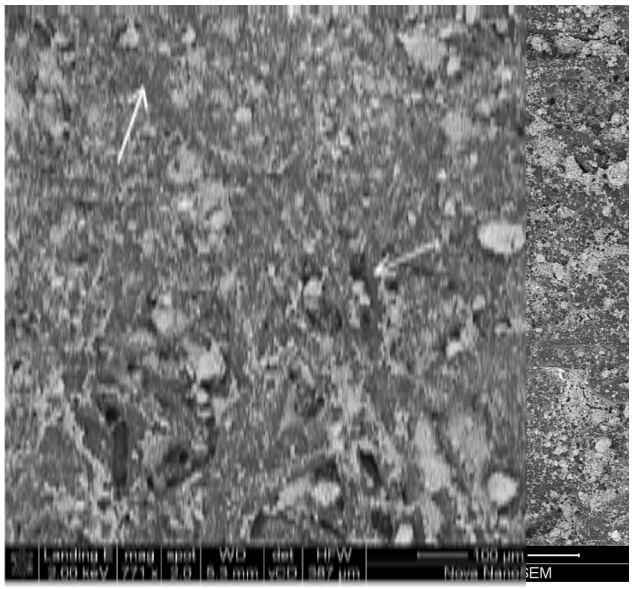

(a)

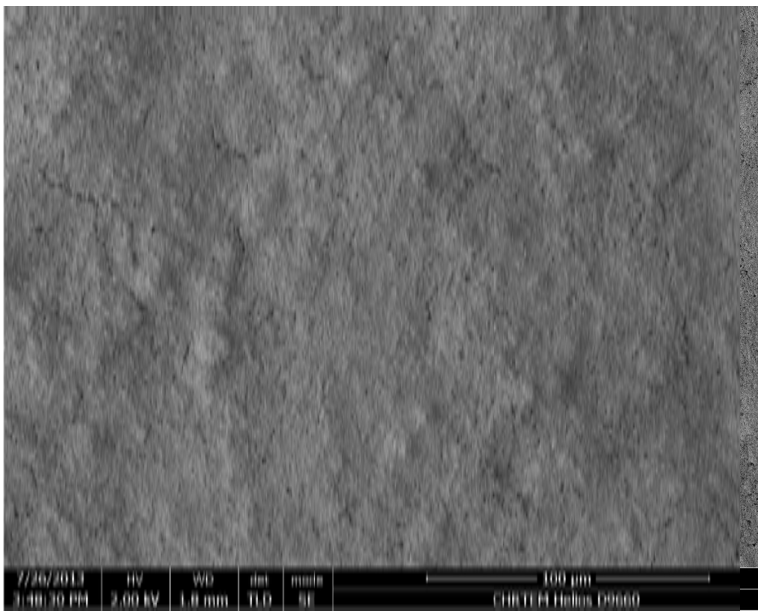

(b)

Fig. 5.4: Backscattered electron (BSE) and SE images showing the printed Ag layers for (a) 35 wt% and (b) 70 wt% particle loading in ETHOCEL^{TM}. Paper fibres are indicated by arrows.

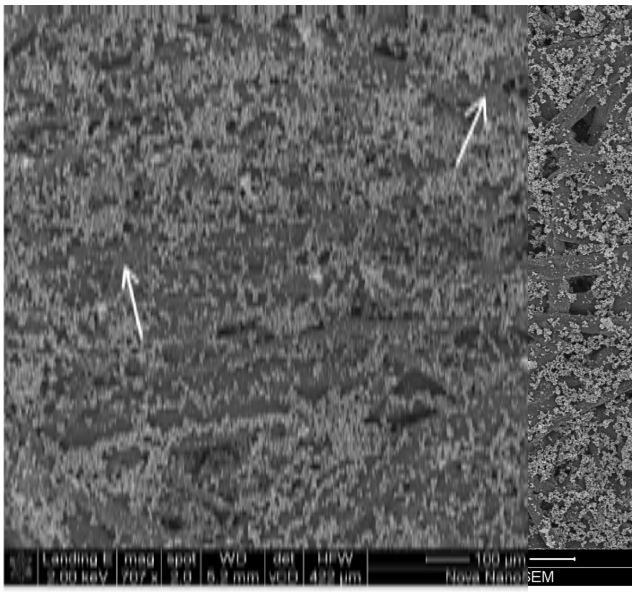

(a)

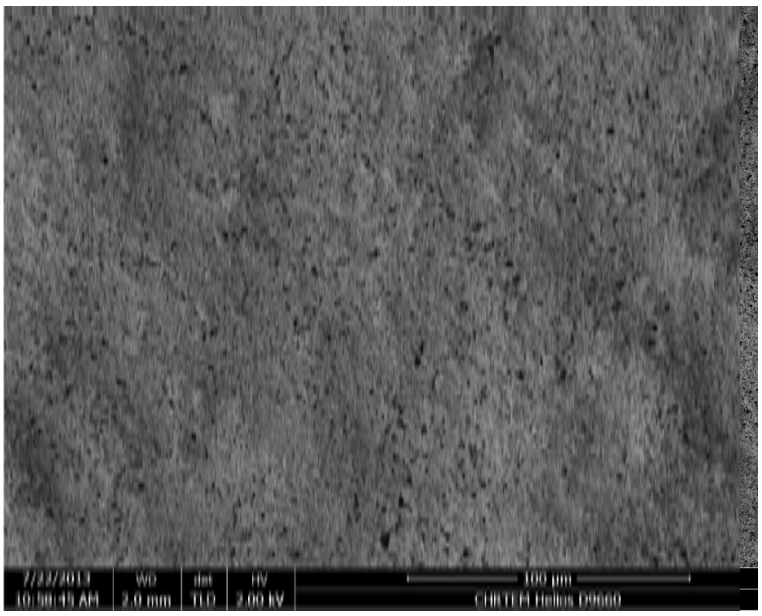

(b)

Fig. 5.5: BSE and SE images showing the printed Pd layers for (a) 25 wt% and (b) 70 wt% particle loading in ETHOCEL^{TM}. Paper fibres are indicated by arrows.

Figure 5.6 and 5.7 shows the SEM micrographs of cross-sections of the printed Ag and Pd layers (in ETHOCEL^{TM}) prepared using Ar ion beam polishing. The cross-sectional view of the 70 wt% Ag layer shows large irregular shaped structures with smaller aggregates dispersed

in between (figure 5.6a). At a higher magnification (figure 5.6b) the larger structures are observed to be agglomerates of smaller aggregates. The aggregates of the larger structures appear to be isolated, but at this magnification finer structures cannot easily be resolved. The cross sectional view of the Pd layer (figure 5.7a) shows that the porosity and chain-like aggregation of particles, which is also visible on the surface micrographs of the sample, are reflected throughout the layer. At a higher magnification (figure 5.7b), it is observed that the size of the voids in the Pd layer are greater than 1μm compared to that of the Ag layer, which is more densely packed and where the voids are much smaller. Even at high particle loadings the Pd layer does not form a compact structure and connections are made through chains of particles forming loops, instead of dense agglomerates.

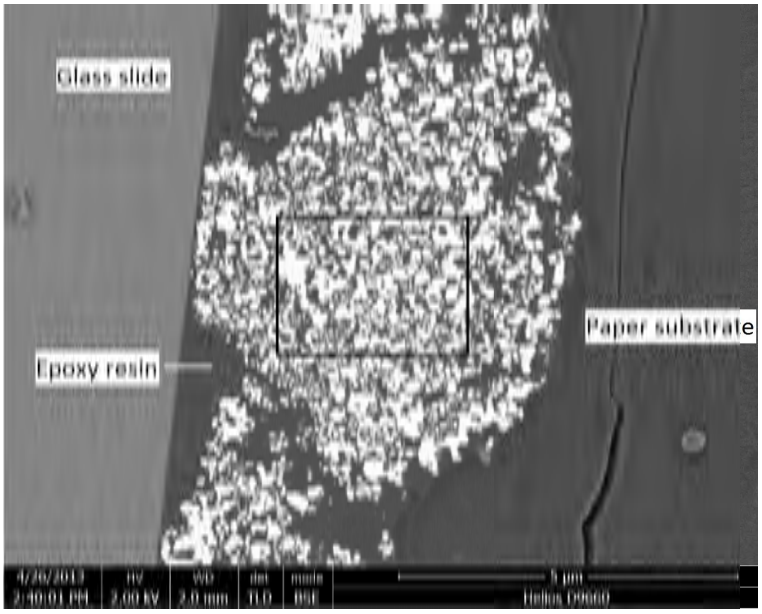

(a)

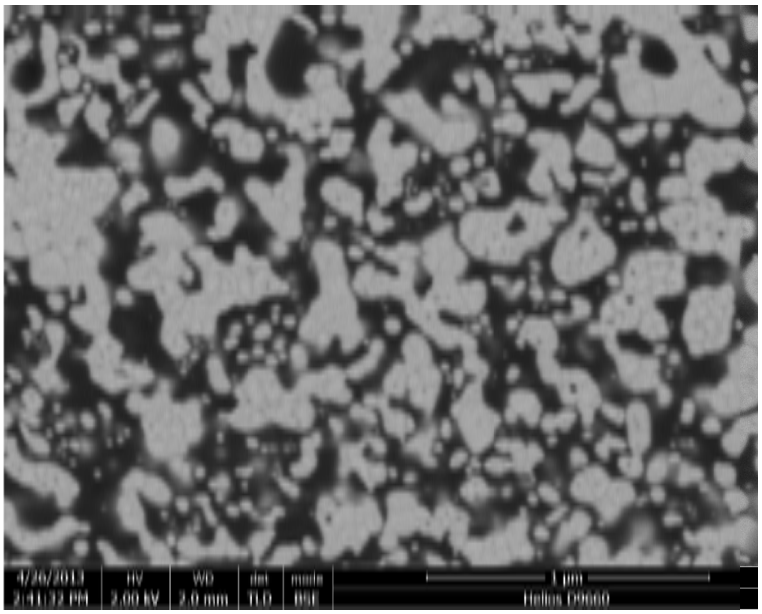

(b)

Fig. 5.6: (a) BSE image of the Argon ion beam polished cross sections of the printed 70wt% Ag layer. (b) Higher magnification image of the region indicated by the square in (a).

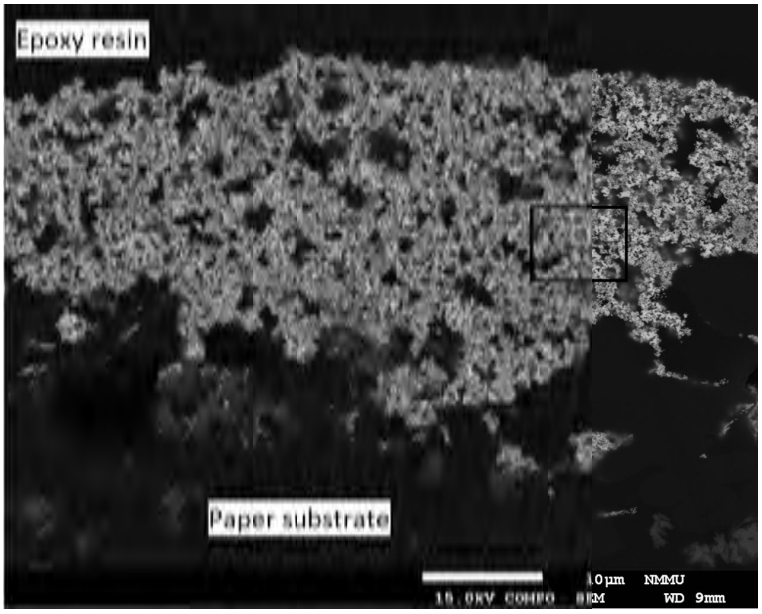

(a)

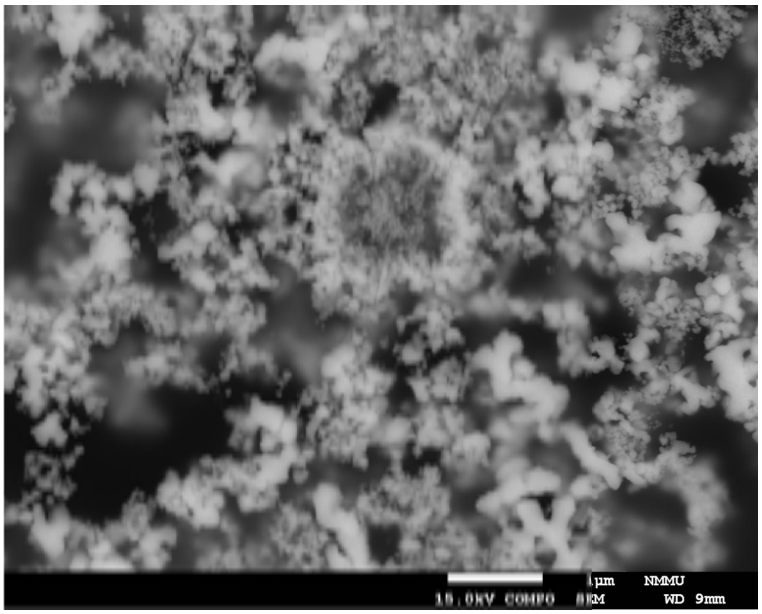

(b)

Fig. 5.7: (a) SE images of the Argon ion beam polished cross sections of the printed 70wt% Pd layer. (b) Higher magnification image of the region indicated by the square in (a).

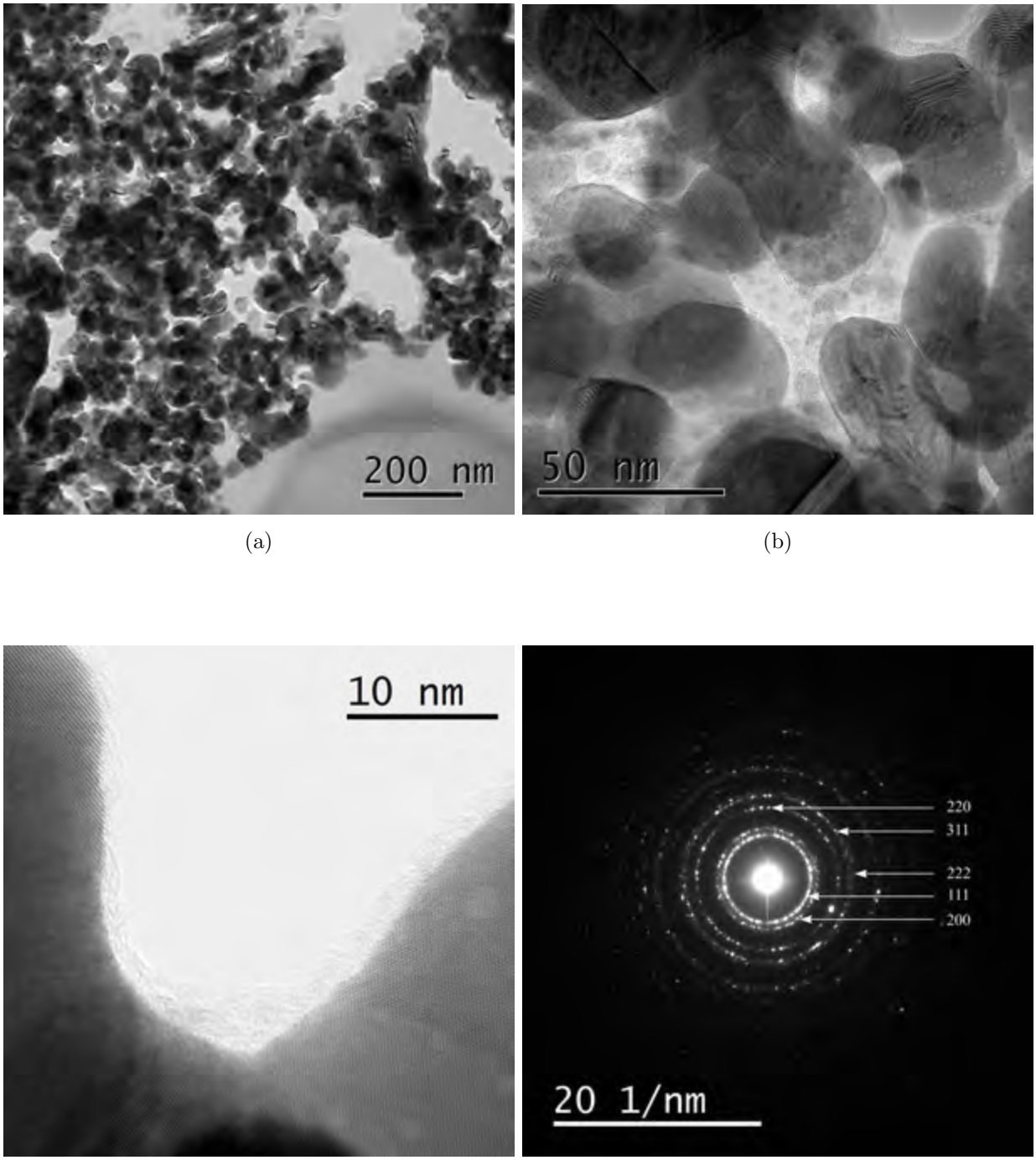

(a) (b)

(c) (d)

Fig. 5.8: (a-b) Low and (c) high-resolution TEM images showing a cross-sectional slice from the printed Ag layers. (d) Selected area diffraction (SAD) ring pattern of the Ag layer.

Figure 5.8a-5.8b and 5.9a-5.9b shows the HRTEM cross-sections of the Ag and Pd layers (in ETHOCEL^{TM}) prepared using FIB. There is a noticeable difference in the packing density of the metal NPs in the two samples. The Ag NPs tend to overlap and tightly aggregate with one another resulting in regions of dense clusters that are bridged with smaller NP agglomerates. In addition to this the individual Ag NP are not clearly distinguishable due to their densely packed structure. In the case of the Pd cross-section, the NPs form interconnected "chain-like" structures that look similar to beads on a string, which result in a more loosely packed microstructure. As a result the clusters tends to have larger unoccupied spaces between the chains of Pd NPs, compared to the Ag NPs which have a more condensed cluster with fewer openings. This pattern of aggregation persists even in the more densely packed regions of the sample. The amorphous regions found along the surface of the particles is most likely the carbon that was deposited during the milling of the lamella. As described in section 4.3.2, carbon was deposited on either side of the lamella in order to fill in the gaps between the nanoparticulate network which provided mechanical stability during the polishing steps. However, as can be seen from the low resolution TEM images, a large portion of the material was lost except for the more densely packed regions which remained intact. Figure 5.8c and 5.9c show the HRTEM image of two touching NPs for Ag and Pd, respectively. Especially for Ag the interparticle junction can clearly be seen where the orientation of the lattice planes changes. Both metal NPs show long range crystalline order which extend right up until the edge of the particles. The variation in the contrast seen in the TEM micrographs are due to the crystal planes aligning in different orientations inside the metal NPs, therefore showing the polycrystallinity of the NPs [146]. The faceted surface of the Pd NPs are more clearly shown at the higher resolution, as well as the smooth surface of the Ag NPs.

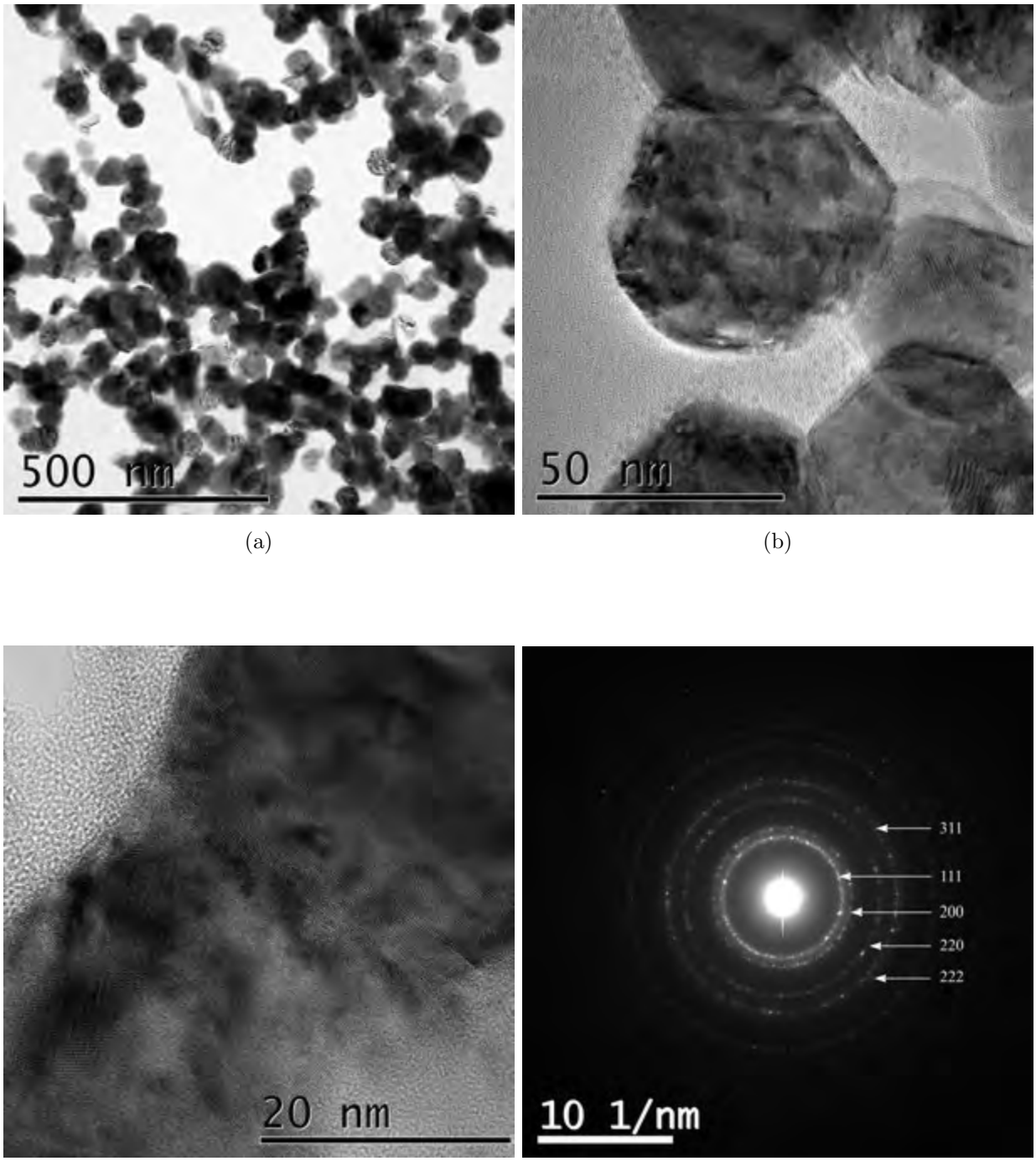

(a) (b)

(c) (d)

Fig. 5.9: (a-b) Low and (c) high-resolution TEM images showing a cross-sectional slice from the printed Pd layers. (d) SAD ring pattern of the Pd layer.

The crystalline nature of the Ag and Pd NPs was shown using electron diffraction in the TEM. Figure 5.8d and 5.9d shows the selected area diffraction (SAD) pattern for the printed Ag and Pd layers, respectively. The diffraction pattern for both metals show concentric rings with various radii which is a feature of a polycrystalline material, but also reflects an agglomeration of crystalline particles [147]. Each ring comprises of a number of spots that appear due to Bragg reflection occurring from the planes of the crystalline lattice [144]. The lattice constant a for Ag and Pd was calculated from the diffraction ring pattern by measuring the radii of the rings and applying equation 5.1, where d_{hkl} is the interplanar spacing of the individual lattice planes (hkl):

$$d_{hkl} = \frac{a}{\sqrt{h^2 + l^2 + k^2}}. \tag{5.1}$$

The analysis of the electron diffraction images was performed using the imaging software, DigitalMicrograph^{TM} (Gatan, Pleasanton, CA, USA). The diffraction rings were indexed according to the fcc crystal structure in which both Ag as well as Pd crystallizes, therefore the SAD pattern shows reflections from the (hkl) planes that are either all odd or all even [148]. Table 5.1 summarizes the results of the measured lattice constants for the first 5 diffraction rings for both metals. The uncertainty for the measured lattice constant was determined using propagation of uncertainty [149]. The lattice constants for Ag and Pd determined from the diffraction patterns agree within experimental uncertainty to their theoretical values.

Table 5.1: The lattice spacing for Ag and Pd NPs.

Lattice plane	Lattice constant a (Å)	
	Silver	Palladium
111	4.11 ± 0.17	3.88 ± 0.09
200	4.12 ± 0.07	3.87 ± 0.08
220	4.14 ± 0.14	3.87 ± 0.08
311	4.12 ± 0.06	3.85 ± 0.06
222	4.12 ± 0.08	3.86 ± 0.06
Theoretical	4.09	3.89

5.2 Electrical Characterisation

5.2.1 Percolative Behaviour of the Printed Layers

The sheet resistivity (ρ_s) of the printed layers was measured for the various particle loadings. The sheet conductivity (σ_m) was calculated by taking the inverse of ρ_s. The data was plotted and analysed using Origin 9.0 Pro (OriginLab Corporation, Northhampton, USA). Figure 5.10 shows the dependency of σ_m on the weight fraction (φ) of the Ag and Pd NPs in inks produced with ETHOCEL^{TM} as binder. For the analysis weight fraction was used instead of volume fraction because the exact volume occupied by the NP-binder mixture could not easily be quantified due to the high surface roughness of the paper substrate. Typical percolation behaviour, as described in section 3.3, was observed for both metal systems, where initially σ_m increased slowly with increasing particle loading up until a critical concentration, at which point a large increase in σ_m is observed. Above this critical concentration, σ_m does not change significantly with increasing particle loading. The experimental data was fitted with the TEPPE (equation 3.17) using the orthogonal distance regression (ODR) iteration algorithm. Values for the sheet conductivity of the insulator σ_i and conductor σ_c, critical weight fraction φ_c and critical exponents s and t were determined from the fit. The results from the fitted data are summarized in table 5.2. The uncertainties shown in figure 5.10 and all subsequent graphs are the standard deviation of the mean [149] based on an average of 15 samples for each particle loading. The percolation threshold for Ag was found to occur at a particle loading of 0.43 ± 0.01 which was higher compared to Pd which occurred at 0.3 ± 0.003. The critical exponents s and t, for both the Ag and Pd systems were found to be slightly out of range with those reported for other conductor-insulator systems i.e $0.37 < s < 1.28$ and $1 < t < 6.27$ [19].

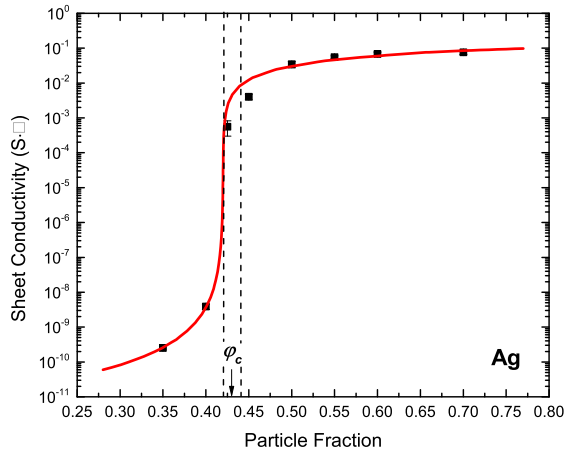

(a)

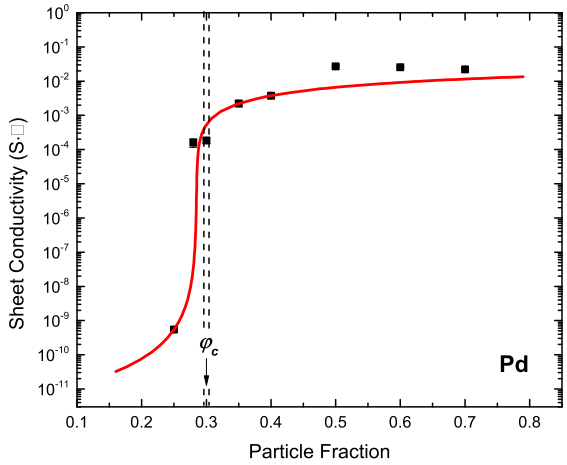

(b)

Fig. 5.10: Dependence of sheet conductivity on weight fraction for the (a) Ag and (b) Pd inks with ETHOCEL^{TM} binder. The solid lines represents the fitted data using equation 3.17.

Table 5.2: Fit parameters obtained from fitting the data shown in Fig.5.10a and 5.10b using equation 3.17.

Material	σ_i (pS $\cdot$ □)	σ_c (S $\cdot$ □)	φ_c	s	t
Silver	5.55 ± 3.62	0.137 ± 0.007	0.43 ± 0.01	2.13 ± 0.34	0.98 ± 0.02
Palladium	5.06 ± 1.62	0.0173 ± 0.0006	0.300 ± 0.003	2.22 ± 0.15	0.983 ± 0.003

Similar percolative behaviour was observed in the Ag ink prepared with the acrylic binder, as shown in figure 5.11. The largest change in σ_m occurs between $50 - 55$wt%. The 70wt% Pd ink in the acrylic binder could not be measured due to the poor printability [1].

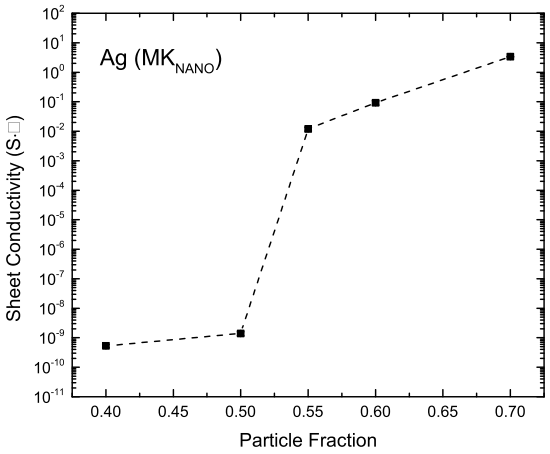

Fig. 5.11: Weight fraction dependence of the sheet conductivity for the printed Ag ink prepared with acrylic binder. The dashed line is given as an indication of the trend in the data.

5.2.2 I-V Characersitics of the Metal Layers

The I-V curves of the printed Ag and Pd (in ETHOCEL^{TM}) layers for different particle loadings are shown in figure 5.12 and 5.13, respectively. The I-V curves for the layers containing 42.5wt% Ag and 25wt% Pd were replotted on a different scale and are shown in the inset of figures5.12a and 5.13a, respectively. At particle loadings below φ_c, current is reduced and the I-V curves, shown in figure 5.12a and 5.13a, deviate from Ohm's law resulting in a curve displaying non-linear symmetric diode-like behaviour [150]. The printed layers with particle concentrations nearest to φ_c tend to have I-V curves that deviate between non-linear and linear behaviour depending on the particular sample measured and where the contacts are positioned. This was observed for the printed layers with particle loadings of 28wt% Pd and 42.5wt% Ag. As the particle loading is increased above φ_c the current increases by approximately 6 orders of magnitude and the I-V curves (figure 5.12b and 5.13b) are linear for similar voltage ranges measured. The slopes of the I-V curves become shallower in a systematic way with increasing particle loading, indicating an increase in the

conductivity.

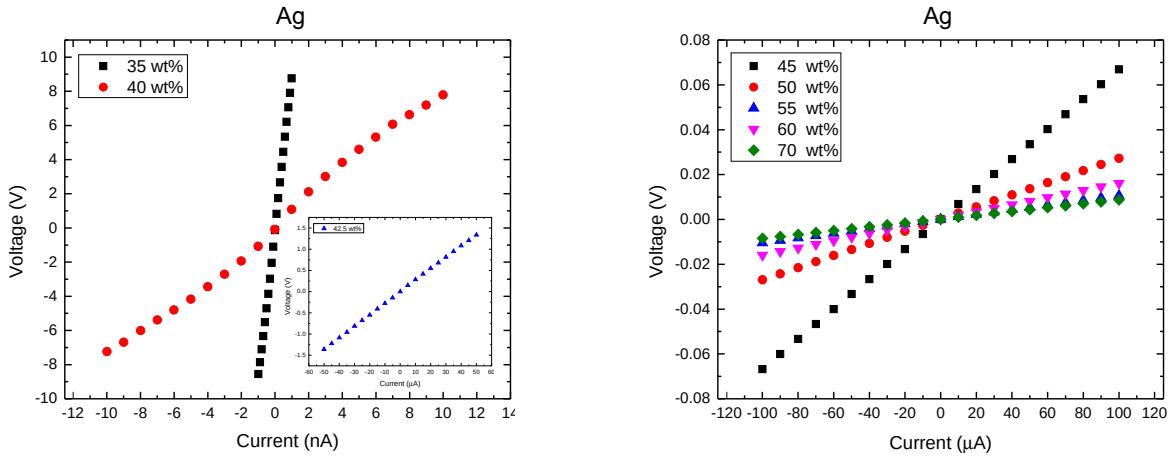

(a) (b)

Fig. 5.12: I-V curves of Ag layers at different particle fractions (a) below φ_c and (b) above φ_c. The graph inset shows the I-V curve for the 42.5wt% printed layer.

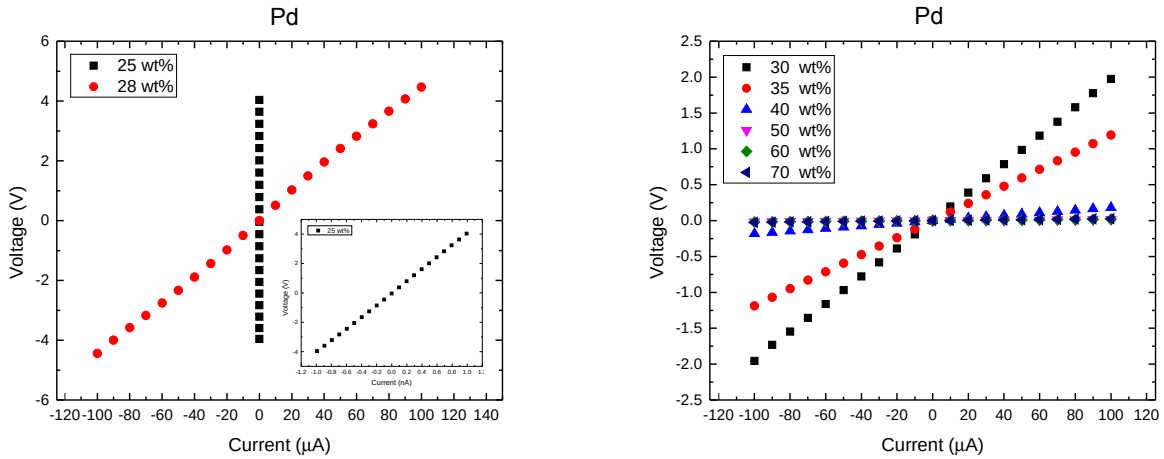

(a) (b)

Fig. 5.13: I-V curves of Pd layers at different particle fractions (a) below φ_c and (b) above φ_c. The graph inset shows the I-V curve for the 25wt% on a different scale.

5.2.3 Hall Effect Measurements

The sheet Hall coefficients (R_{HS}) and effective Hall mobilities (μ_H) for the various particle loadings (in ETHOCEL$^{\mathrm{TM}}$) were obtained from the Hall effect measurements. The magnitude of the Hall coefficient was used as there was not a clear dominant carrier type observed for either metal. The dependence of R_{HS} on the magnetic field for the Ag and Pd layers of different concentrations is shown in figure 5.14a and 5.15a, respectively. In both cases very little change is observed with increasing field strength for each particle concentration, indicating that the systems remains in the low-field limit up to 1 T. Figure 5.14b and 5.15b show R_{HS}, measured at 0.1, 0.5 and 1T, plotted against particle loading for the Ag and Pd systems. For both metals systems, R_{HS} decreases with increasing particle loading with the largest change ($\sim$ 10 orders of magnitude) seen when moving through φ_c. The value of R_{HS} is observed to increase with decreasing field strength, but for the most part the values of R_{HS} for each particle loading lies within the experimental uncertainty with increasing field strength, as shown in figure 5.14a and 5.15a.

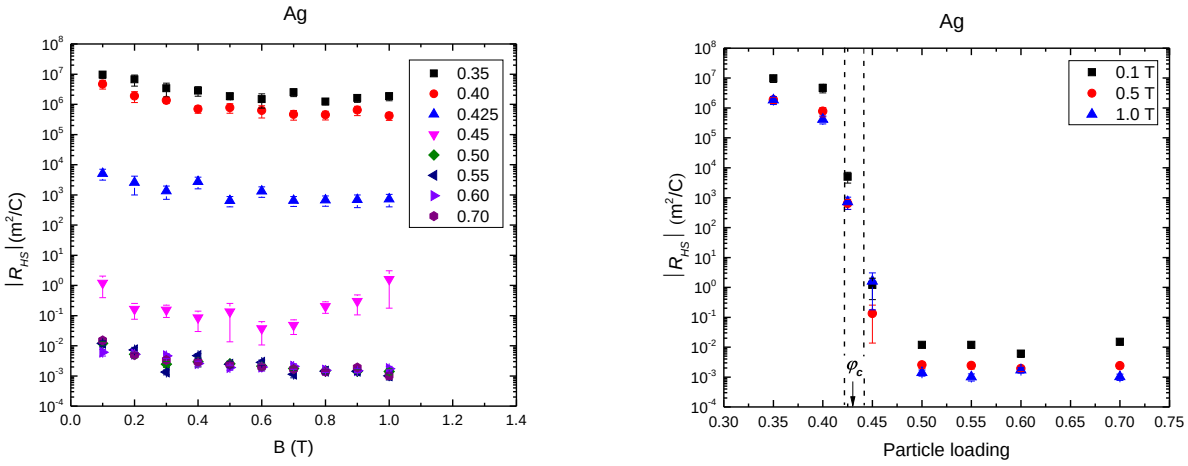

(a) (b)

Fig. 5.14: Sheet hall coefficient versus magnetic field (a) and particle loading (b) for the printed Ag layers. The particle fractions for the printed Ag inks are indicated by the key in (a).

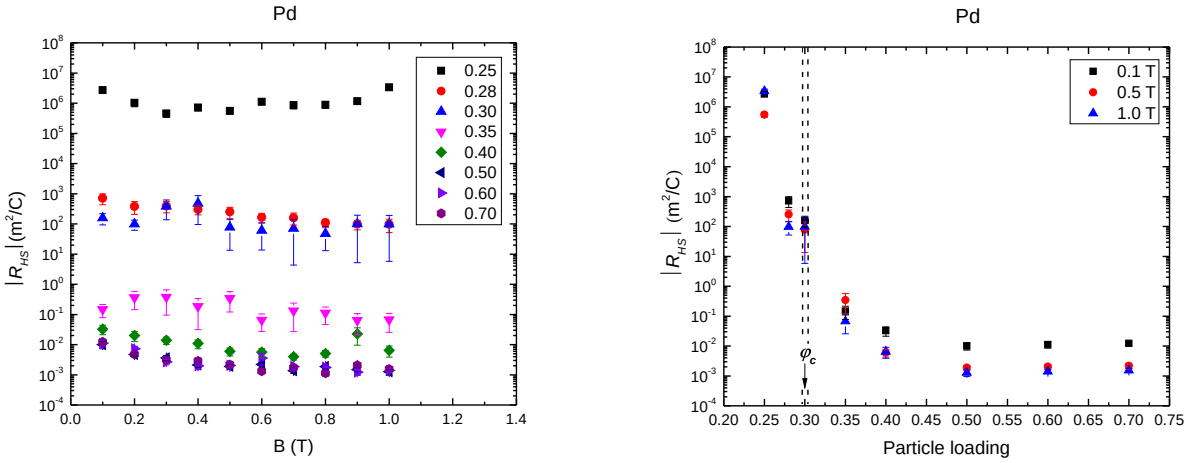

(a) (b)

Fig. 5.15: Sheet hall coefficient versus magnetic field (a) and particle loading (b) for the printed Pd layers. The particle fractions for the printed Pd inks are indicated by the key in (a).

Figure 5.16a and 5.17a show the effective Hall mobilities μ_H plotted as a function of magnetic field for the Ag and Pd systems, respectively. In general, μ_H decreases with increasing magnetic field. A maximum in μ_H is observed at particle loadings nearest to φ_c. This occurs at 42.5 wt% for the Ag system and at 28 wt% for the Pd system. At particle loadings further away from φ_c, μ_H decreases by approximately 2 orders of magnitude. Figure 5.16b and 5.17b shows the graphs of μ_H as a function of particle loading. For both metal systems, μ_H increases as the particle loading is increased from low φ towards φ_c. The value of μ_H increases up to a maximum, after which it falls off with increasing particle concentration. In a similar manner to the previous graphs, the maximum in μ_H occurs at a particle loading of 42.5 wt% for the Ag system and at 28 wt% for the Pd system which both fall within the region of φ_c. As the particle loading is increased above φ_c, μ_H is shown to rapidly decrease in magnitude up until particle concentrations of 45 wt% for Ag and 40 wt% for Pd. Further increase in the particle loading results in very little change being observed in μ_H.

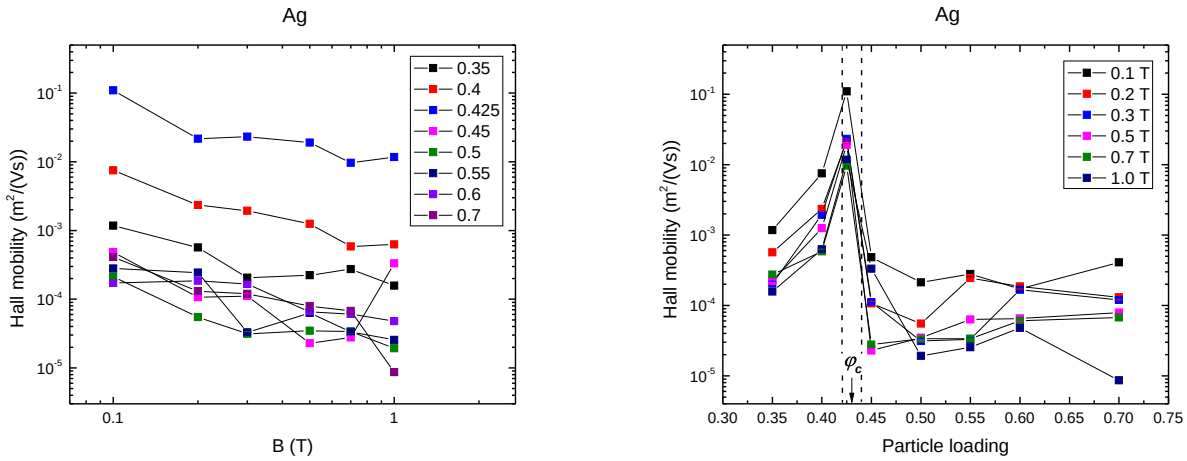

(a) (b)

Fig. 5.16: Effective Hall mobility versus (a) magnetic field and (b) particle loading for the printed Ag layers. The particle fractions for the printed Ag inks are indicated by the key in (a).

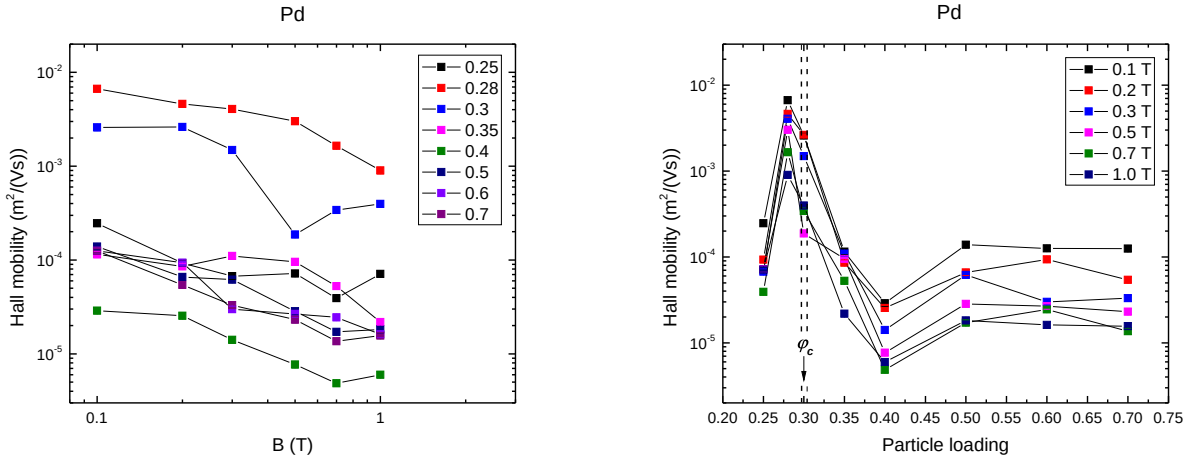

(a) (b)

Fig. 5.17: Effective Hall mobility against (a) magnetic field and (b) particle loading for the printed Pd layers. The particle fractions for the printed Pd inks are indicated by the key in (a).

5.2.4 Impedance Spectroscopy

The impedance of the printed metal layers were carried out using the experimental set-up described in section 4.4.2. The typical impedance curves of the Ag and Pd layers prepared using ETHOCEL^{TM} as binder, for particle fractions below and above φ_c are shown in figure 5.18c, 5.18a and 5.19a, 5.19c, respectively. Particle fractions below φ_c showed a large decrease in the impedance with frequency. For particle fractions above φ_c, the change in impedance with frequency was relatively small ($\sim 1\Omega$). The measured impedance and phase data was used to calculate the real (Re) and imaginary (Im) components of the impedance [151]. The Cole-Cole plots or complex plane impedance diagrams were generated by plotting the Im(Z) against Re(Z). These components are given by,

$$\mathrm{Re}(Z) = |Z| \cos(\theta), \tag{5.2}$$

and

$$\mathrm{Im}(Z) = |Z| \sin(\theta). \tag{5.3}$$

For particle loadings below φ_c, both the Ag and Pd layers displayed a semicircular arc as shown in figure 5.18d and 5.18b. However, the Cole-Cole plots for particle loadings above φ_c produced a curved line as can be seen in figure 5.19b and 5.19d for the Ag and Pd layers, respectively.

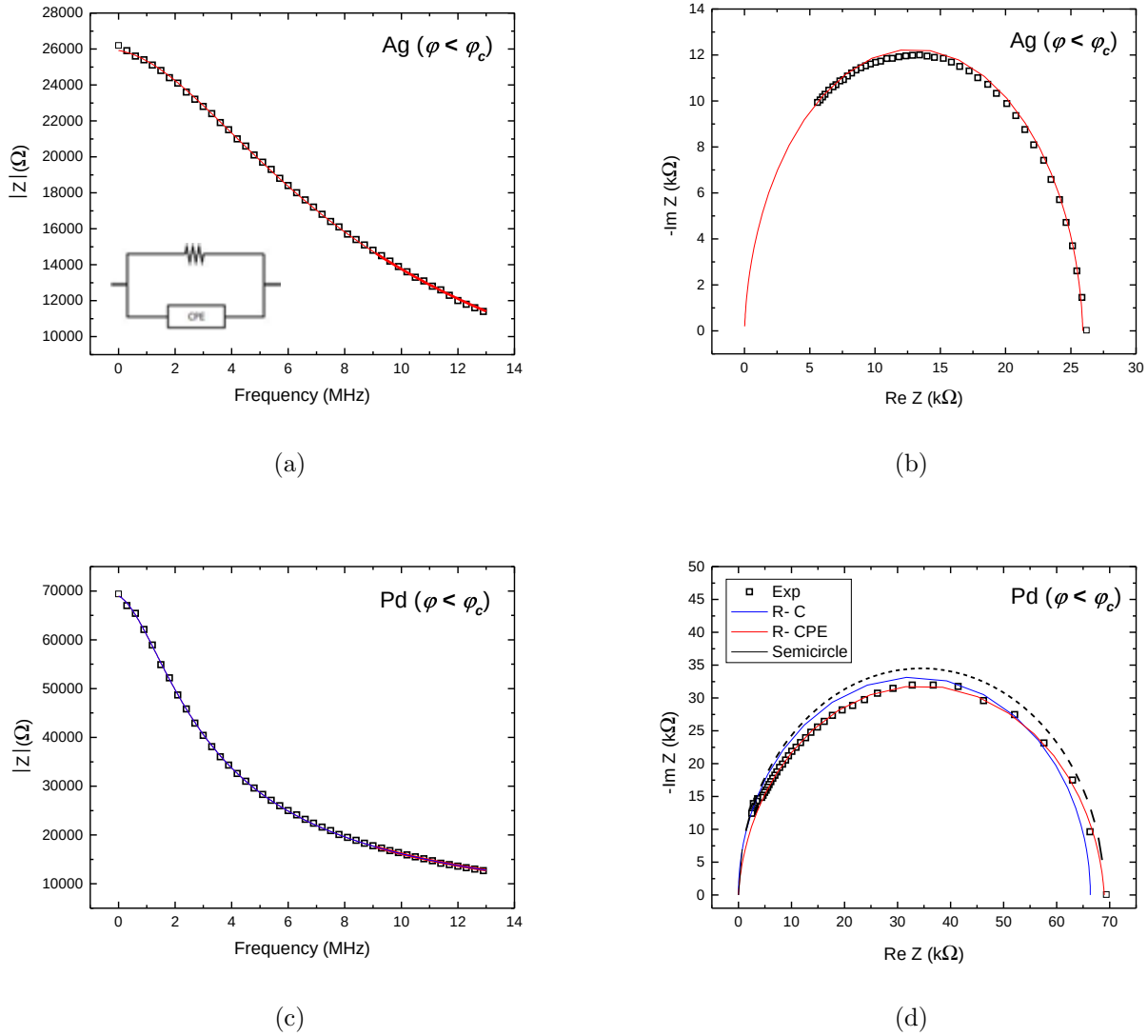

Fig. 5.18: The characteristic impedance against frequency and cole-cole plots for the Ag (a-b) and Pd (c-d) layers ETHOCEL^{TM} at particle fractions below φ_c. The equivalent circuit used to fit the data is shown in the inset of (a). The solid red and blue lines indicates the fitted data using the $R-CPE$ and $R-C$ models respectively; and the dashed line represents an ideal semicircle.

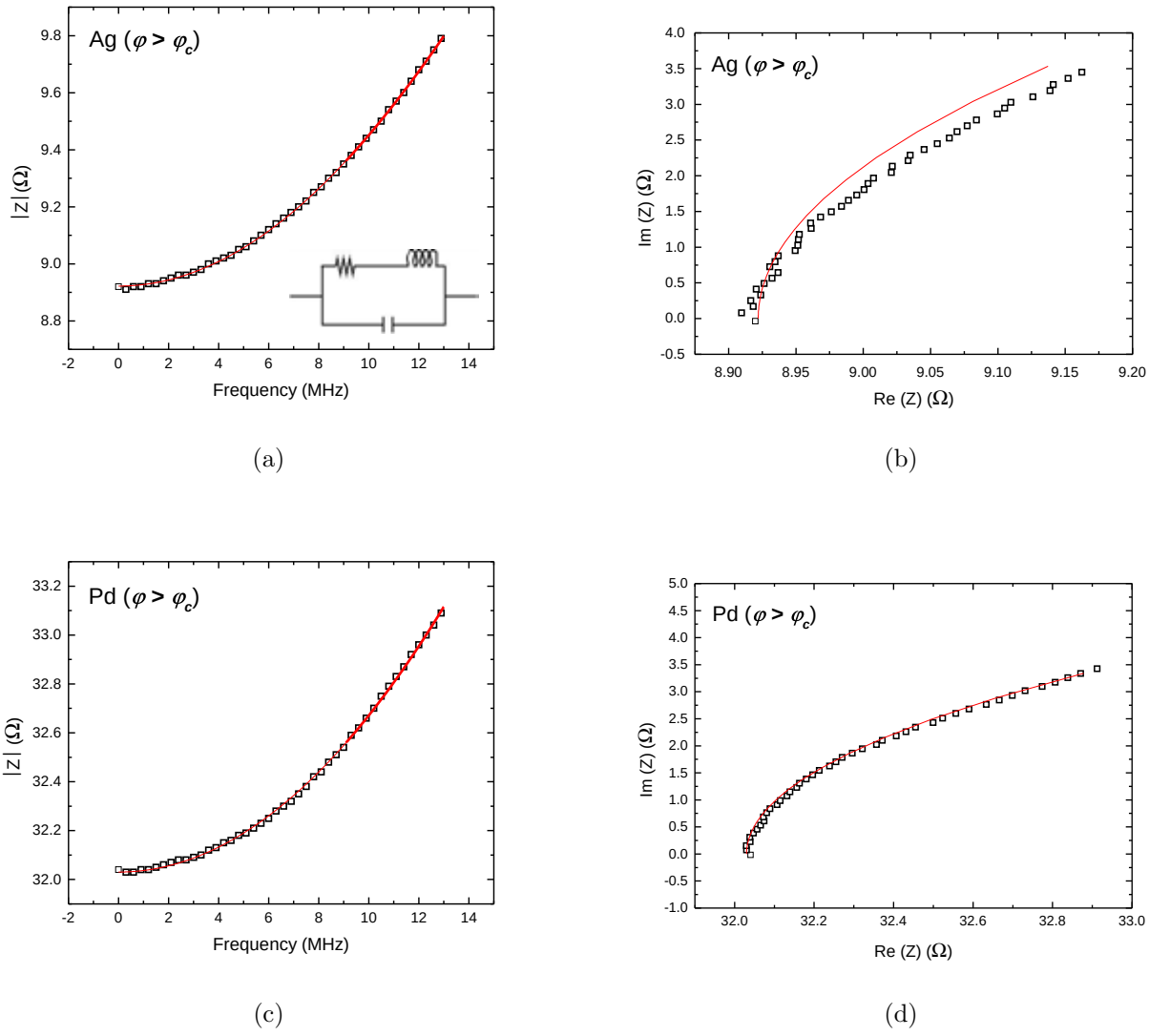

Fig. 5.19: The characteristic impedance against frequency and cole-cole plots for the Ag (a-b) and Pd (c-d) layers in ETHOCEL^{TM}, at particle fractions above φ_c. The equivalent circuit used to fit the data is shown in the inset of (a). The solid line indicates the fitted data using the $RL - C$ model.

Equivalent circuit analysis was performed in order to model the impedance data using discrete components. The theoretical electrical response of various circuits was simulated over a frequency range from 0.001 Hz to 19 MHz using Zview 3.3c (Scribner Associates, Inc.), and compared with the experimental data. This was carried out in order to choose circuit models that best described the impedance for printed layers with particle fractions above and below φ_c. The impedance data plots for particle fractions below φ_c can be represented

by the circuit shown in the inset of figure 5.18c, which consists of a resistor (R) connected in parallel to a constant phase element (CPE). The impedance of this circuit is defined by equations 5.4 to 5.6, where ω is the angular frequency, Q is the pre-factor of the CPE and n its exponent which can vary between 0 and 1 [152]:

$$Z_{Re} = \frac{R(1 + RQ\omega^n \cdot cos(\frac{n\pi}{2}))}{1 + 2RQ\omega^n \cdot cos(\frac{n\pi}{2}) + (RQ\omega^n)^2}, \tag{5.4}$$

$$Z_{Im} = -\frac{R^2Q\omega^n \cdot sin(\frac{n\pi}{2})}{1 + 2RQ\omega^n \cdot cos(\frac{n\pi}{2}) + (RQ\omega^n)^2}, \tag{5.5}$$

$$|Z| = \sqrt{Z_{Re}^2 + Z_{Im}^2}. \tag{5.6}$$

If the exponent $n = 1$ then the CPE behaves as an ideal capacitor. The CPE becomes purely resistive when $n = 0$ [153]. The capacitance (C) can be calculated from the Q value, provided that the value of n or the product of R and C is close to 1 [152, 154]:

$$C = R^{\frac{1-n}{n}}Q^{\frac{1}{n}}. \tag{5.7}$$

The Q and n values obtained for the Ag and Pd layers below φ_c are given in table 5.3. The R values plotted against particle loading is shown in figure 5.20. The value of n for both metallic layers was close to 1, indicating a more capacitive behaviour.

Table 5.3: Values for Q and n obtained from the impedance spectra for $\varphi < \varphi_c$, fitted by equation 5.6.

Material	Particle Concentration (wt%)	Q (pF)	n
Silver	42.5	2.91 ± 1.00	0.96 ± 0.01
Palladium	28	2.28 ± 0.51	0.96 ± 0.01
	30	2.87 ± 0.70	0.95 ± 0.01

The impedance of the printed layers with particle fractions above φ_c can be represented by the circuit shown in the inset of figure 5.19c, which consists of a series resistor-inductor pair placed in parallel with a capacitor. The impedance versus frequency plots were fitted using,

$$|Z| = \sqrt{\left(\frac{R^2 + \omega^2L^2}{\left(1 - \omega^2LC\right)^2 + \omega^2C^2R^2}\right)}. \tag{5.8}$$

All data was plotted and analysed using Origin 9.0 (OriginLab Corporation, Northhampton, USA). Non-linear curve fitting was performed using the Levenberg-Marquardt algorithm. The parameters obtained from fitting the impedance data were used to generate a set of data points for the Re(Z) and Im(Z) components of the equivalent circuits. The Cole-Cole plots in figure 5.18d and 5.19b show the experimental data (open squares) plotted with the simulated data (red solid line). The proposed model of R in parallel with a CPE showed good correlation with the impedance data. The reason for choosing the CPE instead of an ideal capacitor for the equivalent circuit model can be shown by comparing these two circuits. In a similar manner as above, the parameters were obtained from fitting the impedance plot in figure 5.18c using equation 5.9 for the parallel $R - C$ circuit model,

$$|Z| = \frac{R}{\sqrt{1 + (\omega CR)^2}}, \tag{5.9}$$

which was then used to generate the curve represented by the blue line in figure 5.18d. A notable deviation in the data from the ideal $R-C$ behaviour is observed, and in comparison with an ideal semicircle (dashed line), it is seen that the data is indicative of a depressed arc.

The R, C and L values obtained from the fitted impedance data were plotted as a function of particle loading, as can be seen in figure 5.20a and 5.20b for the Ag and Pd layers in ETHOCEL$^{\text{TM}}$, respectively. C is observed to increase with increasing particle loading for both the Ag and Pd layers. Conversely, R decreases with increasing particle loading. In both systems there is a large change in R and C when moving across the region of φ_c. At particle loadings above φ_c very little change is observed in R and C. Both metal systems display similar behaviour, however there are differences in their values for R, C and L. The Pd layers showed a higher resistance compared to the Ag layers. The C values for particle loadings above φ_c are greater by at least one order of magnitude in the Ag layers. No significant change was observed in the L as the particle loading increased for both metal systems. However the inductance for the Ag layers was found to be slightly lower than that of the Pd layers.

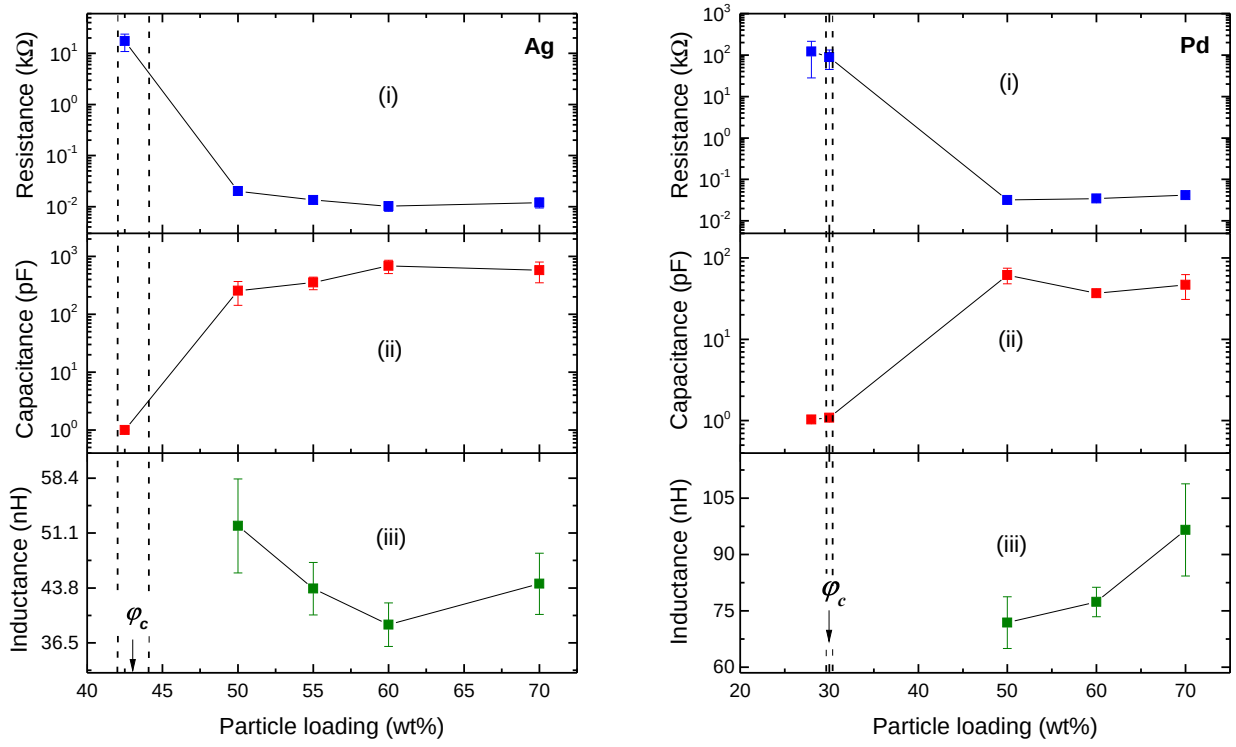

(a) (b)

Fig. 5.20: Resistance, capacitance and inductance as a function of particle loading for the (a) Ag and (b) Pd layers prepared using ETHOCEL^{TM} as binder. The solid lines are a guide to the eye.

6. Discussion

The aim of this research is to investigate the percolative behaviour in printed Ag and Pd nanoparticulate systems, as well as to observe how the structural and electrical properties are influenced by varying the concentration of the metallic and insulating phases. The process by which the metal NPs assemble to form the final microstructure in the printed layer is dependent on the size and shape of the metal NPs, and on the inter-particle and NP-binder interactions [155]. Metallic inks were formulated with different metal NP-binder concentrations and screen-printed onto paper. As described in section 4.1.2, the metal NP inks were prepared with two different binders in order to compare their printability. From the SEM micrographs in figure 5.3, the acrylic-based inks containing the Ag NPs showed good printability, however this was not the case for the 70wt% Pd ink which was unable to produce a uniform layer. Therefore this lead to the decision to use the solvent based inks to produce the samples for this investigation.

6.1 Electron Microscopy

The first part of this study aimed to characterise the nanoparticulate structure of the printed layers using electron microscopy. The selected area diffraction (SAD) analysis performed in the TEM (figure 5.8d and 5.9d) revealed the Ag and Pd NPs to have an fcc crystal structure, however both metals displayed differences in their overall shape as well as polydispersity in their size. The Ag NPs tend to be more spherical and/or slightly elongated in shape (figure 5.8b), whereas the Pd NPs are faceted (figure 5.9d). As mentioned in section 2.1, the variation in the shape and size of the NPs will influence the surface energy and surface-to-volume ratio which in turn can alter the chemical and physical properties of the NPs. These slight changes in the morphology can effect the way in which the metal NPs interact with one another and with the binder. The printed layers consists of the metal NPs whose properties are similar to that of the bulk metal, the polymer binder which provides mechanical support and voids which remain after the solvent evaporates. The latter two regions are insulating for electrons passing through the layer. Figure 6.1 shows a schematic of the main structural features observed in the printed Ag and Pd layers as well as the possible pathways along which charge can flow. The Ag NPs aggregate forming dense clusters (figure 5.6b) resulting in a more compacted layer with a small amount of porosity (figure 5.4b). However, the

Pd NPs tend to form "chain-like" structures (figure 5.7b) which then aggregate resulting in a more loosely-packed microstructure (figure 5.5b). The differences in the microstructural features of the Ag and Pd layers translate to variations observed in their electrical properties which will be discussed below.

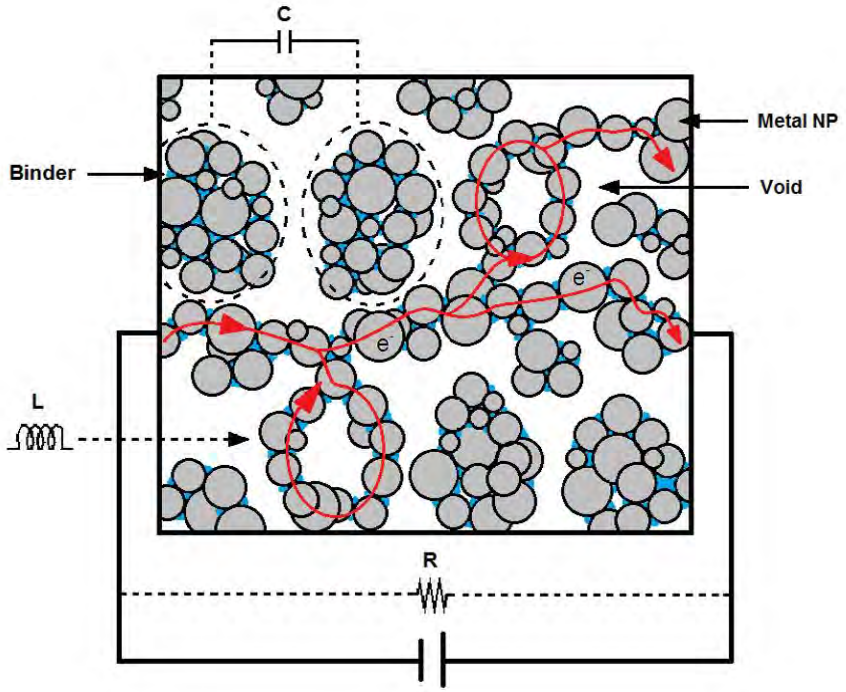

Fig. 6.1: Diagram illustrating a hypothetical model for the microstructure of the printed metal layers. The red arrow indicates the possible paths along which charge will flow through the nanoparticulate network.

6.2 Conductivity of the Metal Layers

The conductivity data shown in figure 5.10 for various particle concentrations displayed percolative behaviour for both metal systems, where the sheet conductivity σ_m was observed to change by 5 orders of magnitude in the region of the critical concentration. The percolation threshold φ_c was found to be larger in Ag, occurring between 43 ± 1 wt%, compared to Pd which was found to be between 30 ± 0.3 wt%. The variation in the value of φ_c can be attributed to the particular way the NPs aggregate to form the final microstructure. The printed layers comprising of 35 wt% Ag and 25 wt% Pd both have σ_m of the order of

10^{-10} S·□. However, from the top surface SEM images of the printed Ag and Pd layers in figure 5.4a and 5.5a, respectively, it is observed that the "chain-like" structures of the Pd NPs occupy a larger area compared to the dense Ag NP clusters which are sparsely scattered over the sample, and have fewer connections with neighbouring clusters. Therefore, connections between neighbouring clusters of Pd NP chains can be made more easily resulting in the formation of the infinite cluster at a lower particle concentration, which will span the sample. The critical exponents for conductivity reported in table 5.2 for the Ag and Pd systems were not in agreement with those predicted for a 3-dimensional network ($s = 0.87$ and $t = 2$) [75, 78], thus indicating non-universal behaviour. However, both the Ag and Pd layers have relatively similar values for s and t which suggests that the nature of the NPs and the microstructure of the metallic layers do not seem to have a significant influence on the critical exponents. The s values for both the Ag and Pd systems were found to be much higher than the values of $s = 0.37 - 1.28$ determined for other composite systems. However the t values for both metallic systems were closer in agreement with those values of $t = 1 - 6.27$ reported in the literature [19]. The deviation of the critical exponents could be due to differences in the preparation method and the spatial arrangement of the NPs in the layers. Factors such as the surface roughness of the substrate and lack of post-printing processing (*e.g* compression, sintering) resulted in the layers having a certain degree of porosity. The NPs in these nanoparticulate networks are never directly in contact with one another due to irregularities in their shape, size and the presence of binder or air near the boundary interface. Yet there is still a finite conductivity observed below φ_c which may be due to interparticle tunnelling [156, 157]. This could contribute to the non-universal conductivity exponents observed in the printed layers.

6.3 I-V Characteristics

There are three distinct regions that can be observed in the conductivity graphs shown in figure 5.10: the highly conducting region for particle loadings $\varphi > \varphi_c$, the insulating region for $\varphi < \varphi_c$ and the transition region where $\varphi = \varphi_c$ [12, 158]. The I-V curves shown in figure 5.12b and 5.13b for the Ag and Pd layers with particle concentrations $\varphi > \varphi_c$, all display Ohmic behaviour. In this region the conductivities of the metal layers are large, and tend to show very little change in their values with increasing particle concentration. At these high particle fractions a continuous metal NP pathway is formed that spans the sample, and as a result metallic conduction will dominate [12, 159]. The metallic behaviour will persist

down until the particle concentration of $\varphi = \varphi_c$. The large drop in conductivity near to φ_c is due to the break-up of the infinite cluster which results in fewer pathways along which the current can flow. Below φ_c, the I-V curves for the Ag and Pd layers (figure 5.12a and 5.13a), show a deviation from linearity. In this region the current is reduced due to the disappearance of the sample-spanning cluster. The conduction is nonmetallic and occurs via tunnelling or thermally activated hopping processes [160, 161]. The type of conduction mechanism will be dependent on the temperature, distance between NP clusters, the amount of binder, geometry of the NP clusters and particle loading [159, 161, 162].

It has been observed that the I-V curves for both the Ag and Pd printed layers with particle concentrations in the region of φ_c show a larger deviation from linearity compared to particle concentrations where $\varphi << \varphi_c$. This can be seen in figure 5.12a and 5.13a for particle concentrations of 42.5 wt% Ag and 28 wt% Pd, respectively. Similar behaviour has been described for particle concentrations close to φ_c in metal-polymer nanocomposites [159]. This indicates that near φ_c, charge transport is not simply a linear superposition of the behaviour in the two limiting cases. The degree of this deviation varies between the samples measured within the same particle loading. The reason for these differences can be attributed to the positioning of the contacts to the sample and the sample production. At particle loadings near to φ_c, the printed layer is not entirely homogeneous as there are regions that are unoccupied. This is as a result of the deposition of the metallic ink onto the substrate that is a random process. If at least one of the contacts are placed such that they are not connected to the infinite cluster, this will lead to the nonlinear behaviour seen in the I-V curves. This can also account for the larger variation and uncertainty observed in the conduction properties as the particle concentration approaches φ_c.

6.4 Hall Effect Parameters

As mentioned in section 3.4, the Hall effect in metals is relatively small due to their high carrier density. It can be seen in figure 5.14a and 5.15a, for both the Ag and Pd layers, R_{HS} showed no significant change in magnitude as the magnetic field strength was increased. The behaviour of R_{HS} with applied field is consistent with the diagrams given in figure 3.5a for a polycrystalline metal in the low-field condition [98, 106]. Since the printed layers are relatively disordered and were measured at higher temperatures, it can be concluded that all measurements were performed in the low-field condition. Under this condition the electrons

are unable to complete a single cyclotron orbit and could get scattered into another orbit type [43]. R_{HS} showed a mixture of both "+" and "−" values with no clear dominant carrier type for different particle loadings. However, previous studies which looked at the Hall effect in Ag and Pd thin films [47, 163, 164, 165] all showed a negative R_{H} which is also negative in the bulk polycrystalline samples [98]. One major difference between this study and the latter is that a heat treatment was performed on the metal films before measurements were taken. The heating of these films would promote coalescence between the metal particles [166] as well as to reduce the effects of the boundaries separating particles [164]. The dependence of R_{HS} on particle loading, shown in figure 5.14b and 5.15b for the Ag and Pd layers, both displayed percolative behaviour. A large decrease in R_{HS} is observed as φ_c is approached from the insulating side, but for values of $\varphi >> \varphi_c$ the concentration of free carriers will reach a saturation point where very little change is observed. The behaviour of R_{HS} can be understood from equation 3.26 which shows R_{HS} to be inversely proportional to the carrier concentration. As the particle concentration of the printed layers is increased, the carrier density will increase and at the same time R_{HS} decreases. The magnetoresistance measurements on the Ag and Pd layers were inconclusive and did not reveal any significant change with increasing magnetic field strength or particle loading. The possible reasons this are similar to those stated for the sign anomaly in R_{HS}.

The magnetic field dependence of the Hall mobility μ_H is shown in figure 5.16a and 5.17a for the Ag and Pd layers, respectively. For both cases, μ_H decreases with increasing magnetic field strength. This inversely proportional relationship between μ_H and the applied magnetic field is given by,

$$\mu_H = \frac{\sigma E_y}{B_z j_x}. \tag{6.1}$$

Similarly, μ_H has shown a dependence on the particle concentration for both metal systems. This behaviour is shown in figure 5.16b and 5.17b for Ag and Pd, respectively. In general, μ_H tends to decrease with increasing particle loading. However, an anomaly is observed in the region of φ_c where there is a sharp increase in μ_H which reaches a maximum for particle concentrations of 42.5 wt% Ag and 28 wt% Pd. The peak in μ_H near φ_c may be explained by the differences observed in the nanoparticulate structure when the particle loading is varied. For very small particle concentrations (figure 5.4a and 5.5a) the layer comprises of discrete metal NP clusters and/or chains that are dispersed uniformly over the substrate. As the particle loading is increased towards φ_c, additional conductive paths

begin to form as connections are made between neighbouring clusters and/or chains. At the same time there are areas that remain unoccupied which separate these conductive pathways. Therefore, the electrons are confined to move along these conductive paths. However, further investigation is needed in order to understand the mobility mechanisms influencing this behaviour. The further reduction in μ_H seen above φ_c could be attributed to the open areas becoming occupied as the particle loading is increased (figure 5.4b and 5.5b) and hence, more conductive pathways are available for the electrons to be scattered into. The lower value of μ_H seen at higher particle loadings could be due to the introduction of more mobile charges and interparticle junctions which act as scattering centres that impede the charge transport. The value of μ_H for the Pd layers was found to be smaller than the Ag layers by at least one order of magnitude. As discussed previously, the conductivity is slightly higher in the Ag layers which stems from the manner in which the NPs assemble to form the final microstructure. This variation in magnitude is expected since μ_H is proportional to the conductivity σ as shown in equation 6.1.

Similar behaviour in μ_H near φ_c has been observed in gold (Au) layers produced via sputtering onto a glass substrate [166]. The thickness of the Au layers was varied by adjusting the length of the sputtering time. The dependence of volume resistivity on the Au layer thickness showed the largest change to occur at a sputtering time of 50 s. At approximately this sputtering time the system reaches the percolation threshold and the sample-spanning cluster is formed. The dependence of μ_H on deposition time at a field strength of 0.2 T is shown in figure 6.2a for the Au layers. For comparison the graphs of μ_H versus particle loading at the same field strength were plotted for the Ag and Pd layers as shown in figure 6.2b. When comparing the two graphs, it can be seen that μ_H for both systems shows a large drop in the region of φ_c as indicated by the arrows in figure 6.2. However, based on the data given in figure 6.2a one is unable to determine whether μ_H decreases for sputtering times well below 50 s. Once the Au system has passed through φ_c, μ_H slowly increases with increasing sputtering time. In the case of the Ag and Pd systems, μ_H tends to fluctuate with no significant change observed.

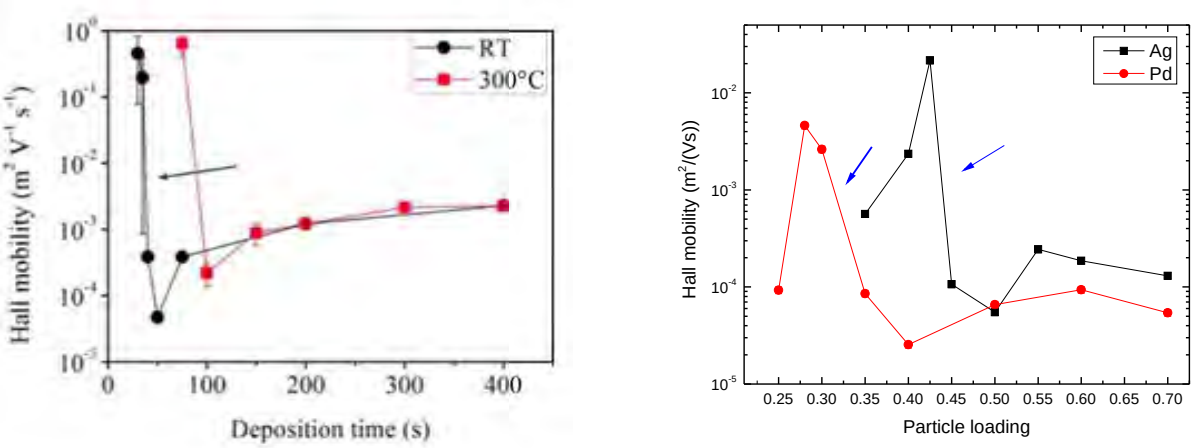

(a) (b)

Fig. 6.2: Graphs showing the dependence of μ_H on (a) deposition time for Au layers prepared via sputtering onto a glass substrate [166], and (b) particle loading for the Ag and Pd layers. The data shown in (a) and (b) was measured using a field strength of 0.2 T.

6.5 Impedance Spectroscopy of Metal Layers

The macroscopic impedance spectrum displayed by the printed metallic layers can be fitted with analytical functions for impedance obtained from circuit models using discrete components (R, C and L). By fitting these functions to the impedance spectrum, values can be extracted for the discrete components which are representative of particular microstructural features of the nanoparticulate layers. In this way one is able to determine the individual contribution to the overall impedance due to the metal NPs and their assembly into higher order structures. The typical complex impedance plots for the Ag and Pd layers in figures 5.18d and 5.19b, showed a significant change in the overall response when moving from the insulating to conducting regions. The total response for particle concentrations where $\varphi > \varphi_c$ produced a curved line with very little change in the real and imaginary components of the impedance. For particle concentrations where $\varphi \leq \varphi_c$, a depressed semi-circle was observed which is apparent when a semi-circle is superimposed onto the Cole-Cole plot (dashed line) in figure 5.18d, where the centre of the circle produced by the experimental data lies below the real axis. The variation in the behaviour of the impedance response is indicative of a change in the microstructure and therefore the mode of charge transport between the two

regions. As a result the equivalent circuits used to fit the characteristic impedance plots are different for the high and low particle loadings.

The equivalent circuit that best describes the impedance response for low particle fractions ($\varphi \leq \varphi_c$) is comprised of an ideal resistor R in parallel with a constant phase element (CPE), as shown in the inset of figure 5.18a. The capacitor C was replaced with a CPE as it produced a better fit to the data. This can be seen in figure 5.18d where the Cole-Cole plot was fitted with the $R-C$ (blue line) and $R-CPE$ (red line) equivalent circuit models. In this particular case the CPE element was used to describe the frequency dependent behaviour of a non-ideal capacitor [154]. The value of C was then calculated using equation 5.7. For high particle fractions ($\varphi > \varphi_c$) the system can be modelled by the equivalent circuit shown in the inset of figure 5.19a, which comprises of a series resistor R and inductor L circuit in parallel with a capacitor C. Figure 6.1 indicates the different contributions to the overall impedance response based on the structures observed in the nanoparticulate layer. R is the total resistance summed over a sample-spanning conductive path with contributions originating from the bulk NP, physical contact between particles and with the probes [167, 168]. L is related to the tendency of the metal NPs to form loops. As can be seen in figure 5.7 and 5.6, these loops are more pronounced in the Pd layers compared to the Ag layers. The overall capacitance C of the system can be viewed as a network of series and parallel capacitors arising from the interaction between neighbouring NP clusters in the Ag layers, and "chains-like" NP aggregates in the Pd layers. There will also be a contribution to C from the interaction between the metal clamps and the NPs.

Due to the limitations of the impedance analyser, only particle concentrations whose resistances were smaller than 1.3 MΩ could be measured. Therefore, the smallest concentrations that were able to be measured were 42.5 wt% Ag, 28 and 30 wt% Pd. In figures 5.20a(i) and 5.20b(i), the resistance is shown to decrease with increasing particle loading for both metal systems. In addition to this the Pd layers were observed to have larger R values compared to the Ag layers at similar particle concentrations. In the case of particle loadings near to φ_c, the R values for the Pd and Ag layers differed by a factor of 10. A possible reason for this behaviour could be due to do the contact resistance between particles and the number of conductive paths available for current to travel along. Current will tend to flow along paths which are the least resistive [169]. The Ag layers comprising of dense NP clusters which aggregate together with increasing φ to form a more compact structure have more conductive paths along which charge can flow. In the case of the Pd layer, the "chain-like" structures aggregate to produce a highly porous microstructure which is more limited in the

number of pathways available for the current to travel along. Differences in the packing structure of the metal NPs may result in a wider range of contact resistance values in the Pd layers compared to the Ag layers. The graphs in figure 5.20a(ii) and 5.20b(ii), show C to increase with φ. This behaviour can be explained using the formula for a parallel plate capacitor [170] given by,

$$C = \frac{\epsilon_0 \epsilon_r A}{d}, \tag{6.2}$$

where A is the effective area of the metal NPs, ϵ_0 and ϵ_r are the permittivity of vacuum and the material respectively. As the particle concentration is reduced to values where $\varphi \leq \varphi_c$, the aggregates of NP clusters and/or chains reduce in size and are therefore further spaced apart. As a result A decreases while d increases which in turn will cause the value of C to decrease. At higher particle loading the size of the NP clusters and/or chains will grow while at the same time reducing the average distance between neighbouring aggregates. Therefore, A will increase while d decreases which causes C to increase. The SEM micrographs in figure 5.6 and 5.7, show the Ag NP clusters to have a larger surface area and smaller distances between neighbouring clusters, compared to the "chain-like" structures of Pd NPs which are more loosely-packed in the layer. These differences may account for the higher value of C observed in the Ag layers. The graphs in figure 5.20a(iii) and 5.20b(iii), show very little change in L with particle loading for both the Ag and Pd layers. The higher L values observed in the Pd layers could be due to the presence of the ring like structures seen in figure 5.7b.

7. Conclusion

Ag and Pd inks were formulated and successfully screen printed on paper. The *ac* and *dc* electrical properties of the printed nanoparticulate layers, with varying NP concentrations, were characterised and correlated with the microstructural features of the layer. Observations made from the electron microscopy measurements revealed differences in the morphology of the Ag and Pd layers, especially at low particle loadings. A more tightly packed Ag layer was formed due to the individual NPs assembling into dense clusters, whilst the Pd NPs aggregated into "chain-like" structures resulting in a more loosely packed layer, with the "chains" of particles clustering together to form "loops" which were more pronounced at higher particle loadings. One reason for the microstructural variation seen between the Ag and Pd layers could be due to the Ag NPs being coated with polyvinylpyrrolidone (PVP). From this it can be seen that the surface properties of the metal NPs play an important role in determining how they interact with one another and with the binder. In addition to this, variations observed in the shape of the Ag and Pd NPs could also be a contributing factor. Further investigation would look at changing the surface chemistry of the NP by using different chemical functional groups, as well as using NPs of various shapes to produce different microstructural features in the layer.

One particular problem that was encountered when using paper as a substrate is that it has a high surface roughness which makes it difficult to accurately determine the thickness of the printed layers, especially for low particle loadings. In addition to this, during the deposition of the ink the smaller NP clusters tended to fill the "grooves" between the paper fibres. Therefore, connections between neighbouring clusters would only be made once the NPs have filled these "grooves". This ultimately would have had a large affect on how quickly the infinite cluster formed with increasing particle loading. In order to improve on this, substrates with low surface roughness should be used.

The observable differences in the packing arrangement of the NPs in the printed layers has provided insight into how quickly the behaviour of the system changes from insulating to metallic with increasing particle loading. The TEPPE which was successfully used to fit the conductivity data, showed that the Pd layers reached φ_c at a lower particle loading compared to the Ag layers. The Pd "chain-like" structures are able to extend over a larger area of the substrate which implies that less material is needed to make connections with a nearest neighbour. In the case of the Ag layers, connections between neighbouring clusters

are formed as the size of the clusters increases which as a result requires higher particle concentrations. The values obtained for the critical exponents (s, t) for both metal systems were not in good agreement with those predicted theoretically or the values determined experimentally for other systems. The change from insulating to metallic behaviour in the metal systems was further emphasized by the I-V characteristics of the printed layers which displayed non-ohmic behaviour for particle loadings below φ_c and ohmic behaviour above φ_c. Since the main focus of this research was on the global connectivity of the system (i.e. macroscopic properties) which governs the electrical conduction through the layer, further work will be required to understand the charge transport processes at the microscopic level, that influence the electrical conduction through the NP network.

The Hall effect parameters (i.e. R_{HS}, μ_H) for both metal systems displayed significant changes as the particle loading was varied. The R_{HS} values for the Ag and Pd layers showed typical percolation behaviour where a large change was observed in the region of φ_c. Furthermore, an abrupt increase in μ_H is seen in the Ag and Pd layers with particle concentrations near to φ_c, however the values drop off for particle loadings further away. This anomaly is not fully understood and could be due to the changes in the microstructure and/or charge transport mechanism near to φ_c. For particle loadings well above φ_c, R_{HS} and μ_H are unchanging. Future work would look at exploring various models which could be used to describe the dependence of R_{HS} and μ_H on the particle concentration. The Hall effect in the printed metals layers was very small which was due to the measurements being carried out at RT in low magnetic fields. Under these experimental conditions and together with the layers being relatively disordered, the charge transport would be dominated by scattering processes. In addition to this the measurements were inconclusive with regard to the sign of the charge carrier. These issues could be minimized by performing the experiment using stronger magnetic fields and lower temperatures. A requirement when measuring the Hall effect using the van der Pauw technique is that the sample should be homogeneous with no holes and of uniform thickness. Based on the electron microscopy images it has been shown that the layers have a certain degree of porosity, and are not uniform due to the uneven substrate. One way to observe how the degree of disorder affects the results is to compare with a more homogeneous sample. This can be done through post-processing techniques (eg. calendering, heat treatments) which would create a more uniform layer.

From the impedance spectroscopy analysis it has been shown that a simple $R-CPE$ circuit can be used to represent the printed layers with metal NP fractions below φ_c. For particle fractions above φ_c, both metal systems can be described by a series $R-L$ circuit in parallel

with C. By measuring the discrete components, which represent the structural features (i.e. NP clusters, chains and loops) observed in the nanoparticular layers, gave an indication of how the system changes with varying particle loading. For both the Ag and Pd layers, the values of R and C as a function of particle loading showed similar trends whereby a large change was observed near to φ_c. However, the value of L showed only a slight variation with increasing particle loading. The Ag layers were found to have a larger capacitance and smaller resistance and inductance compared to the Pd layers. This could be due to the differences observed between the Ag and Pd layers in the number of conductive paths available as well as how tightly packed the layer was. The inability of the impedance spectrometer to measure samples with resistances greater than 1.3 MΩ meant that there was no information for the very low particle loadings. In order to get a clearer understanding of how the metal systems change with particle loading, future measurements would require more sensitive equipment which is able to measure at lower frequencies (< 5 Hz) and over a wider impedance range.

From the results the Ag and Pd inks have shown to produce good conductive layers. The percolation studies gave incite into the minimum compositions needed to produce reasonable conductive layers. However, in order for these conductive inks to be viable in printed electronics, further efforts should be made to reduce the particle loading as well as finding alternative substrates. In understanding how the charge transport is affected by the arrangement of the NP network, one can then in future tailor the shape, size and surface morphology of the metal NPs as well as control the manner in which they assemble in order to optimize their function and produce a desired effect in electronic devices.

References

[1] U Männl, C van den Berg, B Magunje, M Härting, DT Britton, S Jones, MJ van Staden, and MR Scriba. Nanoparticle composites for printed electronics. *Nanotechnology*, 25(9):094004, 2014.

[2] Rita Faddoul, Nadge Reverdy-Bruas, and Anne Blayo. Formulation and screen printing of water based conductive flake silver pastes onto green ceramic tapes for electronic applications. *Materials Science and Engineering: B*, 177(13):1053 – 1066, 2012.

[3] Mi-Young Lee, Myung-Won Lee, Ji-Eun Park, Jong-Seung Park, and Chung-Kun Song. A printing technology combining screen-printing with a wet-etching process for the gate electrodes of organic thin film transistors on a plastic substrate. *Microelectronic Engineering*, 87(10):1922–1926, 2010.

[4] Wei Wu, Shuanglei Yang, Shaofeng Zhang, Hongbo Zhang, and Changzhong Jiang. Fabrication, characterization and screen printing of conductive ink based on carbon@ ag core–shell nanoparticles. *Journal of colloid and interface science*, 427:15–19, 2014.

[5] Jolke Perelaer, Patrick J Smith, Dario Mager, Daniel Soltman, Steven K Volkman, Vivek Subramanian, Jan G Korvink, and Ulrich S Schubert. Printed electronics: the challenges involved in printing devices, interconnects, and contacts based on inorganic materials. *Journal of Materials Chemistry*, 20(39):8446–8453, 2010.

[6] David T Britton, M Härting, et al. Printed nanoparticulate composites for silicon thick-film electronics. *Pure and applied chemistry*, 78(9):1723–1739, 2006.

[7] Rita Faddoul, Nadège Reverdy-Bruas, and Joséphine Bourel. Silver content effect on rheological and electrical properties of silver pastes. *Journal of Materials Science: Materials in Electronics*, 23(7):1415–1426, 2012.

[8] Karl Skucha, Zhiyong Fan, Kanghoon Jeon, Ali Javey, and Bernhard Boser. Palladium/silicon nanowire schottky barrier-based hydrogen sensors. *Sensors and Actuators B: Chemical*, 145(1):232–238, 2010.

[9] Alexander Kamyshny, Matti Ben-Moshe, Shai Aviezer, and Shlomo Magdassi. Ink-jet printing of metallic nanoparticles and microemulsions. *Macromolecular Rapid Communications*, 26(4):281–288, 2005.

[10] In-Keun Shim, Young Il Lee, Kwi Jong Lee, and Jaewoo Joung. An organometallic route to highly monodispersed silver nanoparticles and their application to ink-jet printing. *Materials Chemistry and Physics*, 110(2):316–321, 2008.

[11] M Härting, J Zhang, DR Gamota, and DT Britton. Fully printed silicon field effect transistors. *Applied Physics Letters*, 94(19):193509, 2009.

[12] Amir Zabet-Khosousi and Al-Amin Dhirani. Charge transport in nanoparticle assemblies. *Chemical reviews*, 108(10):4072–4124, 2008.

[13] Y Srinivasa Rao. Studies on electrical properties of polymer thick film resistors. *Microelectronics international*, 24(1):8–14, 2007.

[14] Rolf Landauer. Electrical conductivity in inhomogeneous media. In *Electrical transport and optical properties of inhomogeneous media*, volume 40, pages 2–45. AIP Publishing, 1978.

[15] Ian J Youngs. Exploring the universal nature of electrical percolation exponents by genetic algorithm fitting with general effective medium theory. *Journal of Physics D: Applied Physics*, 35(23):3127, 2002.

[16] A Celzard, JF Mareche, and G Furdin. Modelling of exfoliated graphite. *Progress in Materials Science*, 50(1):93–179, 2005.

[17] DS McLachlan. Measurement and analysis of a model dual-conductivity medium using a generalised effective-medium theory. *Journal of Physics C: Solid State Physics*, 21(8):1521, 1988.

[18] David S McLachlan, Cosmas Chiteme, Cheol Park, Kristopher E Wise, Sharon E Lowther, Peter T Lillehei, Emilie J Siochi, and Joycelyn S Harrison. Ac and dc percolative conductivity of single wall carbon nanotube polymer composites. *Journal of Polymer Science Part B: Polymer Physics*, 43(22):3273–3287, 2005.

[19] David S McLachlan and Godfrey Sauti. The ac and dc conductivity of nanocomposites. *Journal of Nanomaterials*, 2007(1):15, 2007.

[20] VI Roldughin and VV Vysotskii. Percolation properties of metal-filled polymer films, structure and mechanisms of conductivity. *Progress in organic coatings*, 39(2):81–100, 2000.

[21] Godfrey Sauti and David S McLachlan. Impedance and modulus spectra of the percolation system silicon–polyester resin and their analysis using the two exponent phenomenological percolation equation. *Journal of materials science*, 42(16):6477–6488, 2007.

[22] Jin Z Zhang. Ultrafast studies of electron dynamics in semiconductor and metal colloidal nanoparticles: Effects of size and surface. *Accounts of chemical research*, 30(10):423–429, 1997.

[23] L Jos De Jongh. Physical properties of metal cluster compounds. model systems for nanosized metal particles. *Metal Clusters in Chemistry*, pages 1434–1453, 1999.

[24] Helmut Goesmann and Claus Feldmann. Nanoparticulate functional materials. *Angewandte Chemie International Edition*, 49(8):1362–1395, 2010.

[25] Kenneth J Klabunde and Ryan Richards. *Nanoscale materials in chemistry*, volume 1035. Wiley Online Library, 2001.

[26] Gunter Schmid. Metals. *Nanoscale Materials in Chemistry*, pages 15–59, 2001.

[27] Younan Xia, Yujie Xiong, Byungkwon Lim, and Sara E Skrabalak. Shape-controlled synthesis of metal nanocrystals: Simple chemistry meets complex physics? *Angewandte Chemie International Edition*, 48(1):60–103, 2009.

[28] Emil Roduner. Size matters: why nanomaterials are different. *Chemical Society Reviews*, 35(7):583–592, 2006.

[29] CN Ramachandra Rao, Giridhar U Kulkarni, P John Thomas, and Peter P Edwards. Metal nanoparticles and their assemblies. *Chemical Society Reviews*, 29(1):27–35, 2000.

[30] Clemens Burda, Xiaobo Chen, Radha Narayanan, and Mostafa A El-Sayed. Chemistry and properties of nanocrystals of different shapes. *Chemical reviews*, 105(4):1025–1102, 2005.

[31] Peter P Edwards, Roy L Johnston, and CNR Rao. On the size-induced metal-insulator transition in clusters and small particles. *Metal Clusters in Chemistry*, pages 1454–1481, 1999.

[32] Tapan K Sau, Andrey L Rogach, Frank Jäckel, Thomas A Klar, and Jochen Feldmann. Properties and applications of colloidal nonspherical noble metal nanoparticles. *Advanced Materials*, 22(16):1805–1825, 2010.

[33] Kenneth J Klabunde and Ravichandra S Mulukutla. 7 chemical and catalytic aspects of nanocrystals. *Nanoscale Materials in Chemistry*, page 223, 2001.

[34] Olga Koper and Slawomir Winecki. 8 specific heats and melting points of nanocrystalline materials. *Nanoscale Materials in Chemistry*, page 263, 2001.

[35] Klaus Sattler. The energy gap of clusters, nanoparticles, and quantum dots. *Handbook of Thin Films Materials, Nanomaterials and Magnetic Thin Films*, 5:61–97, 2002.

[36] Mostafa A El-Sayed. Some interesting properties of metals confined in time and nanometer space of different shapes. *Accounts of chemical research*, 34(4):257–264, 2001.

[37] JM Ziman. Electrons and phonons: The theory of transport phenomena in solids clarendon, 1960.

[38] Bernd von Issendorff and Ori Cheshnovsky. Metal to insulator transitions in clusters. *Annu. Rev. Phys. Chem.*, 56:549–580, 2005.

[39] Mei Chen, Binghui Wu, Jing Yang, and Nanfeng Zheng. Small adsorbate-assisted shape control of pd and pt nanocrystals. *Advanced Materials*, 24(7):862–879, 2012.

[40] Andrea R Tao, Susan Habas, and Peidong Yang. Shape control of colloidal metal nanocrystals. *Small*, 4(3):310–325, 2008.

[41] John M Ziman. The physics of metals. *The Physics of Metals, by JM Ziman, Cambridge, UK: Cambridge University Press, 2011*, 1, 1969.

[42] Charles Kittel and Paul McEuen. *Introduction to solid state physics*, volume 8. Wiley New York, 1976.

[43] John Sydney Dugdale and JS Dugdale. *The electrical properties of metals and alloys*. E. Arnold, 1977.

[44] AB Cracknell and Kee Choon Wong. Fermi surface. its concept, determination, and use in the physics of metals. 1973.

[45] Mohd Abdul Majeed Khan, Sushil Kumar, Maqusood Ahamed, Salman A Alrokayan, and Mohammad Saleh AlSalhi. Structural and thermal studies of silver nanoparticles and electrical transport study of their thin films. *Nanoscale research letters*, 6(1):1–8, 2011.

[46] Protima Rauwel, Erwan Rauwel, Stanislav Ferdov, and Mangala P Singh. Silver nanoparticles: Synthesis, properties, and applications. *Advances in Materials Science and Engineering*, 2015, 2015.

[47] Aleksandar B Menicanin, Ljiljana D Zivanov, Goran M Stojanovic, Natasa M Samardzic, and Danijela V Randjelovic. Transport parameters of inkjet printed nanoparticle silver on polyimide substrate measured at room and liquid nitrogen temperatures. *Electron Devices, IEEE Transactions on*, 60(9):2963–2967, 2013.

[48] Thi Thi Nge, Masaya Nogi, and Katsuaki Suganuma. Electrical functionality of inkjet-printed silver nanoparticle conductive tracks on nanostructured paper compared with those on plastic substrates. *Journal of Materials Chemistry C*, 1(34):5235–5243, 2013.

[49] S Iravani, H Korbekandi, SV Mirmohammadi, and B Zolfaghari. Synthesis of silver nanoparticles: chemical, physical and biological methods. *Research in pharmaceutical sciences*, 9(6):385, 2014.

[50] FM Mueller, AJ Freeman, JO Dimmock, and AM Furdyna. Electronic structure of palladium. *Physical Review B*, 1(12):4617, 1970.

[51] Byungkwon Lim, Majiong Jiang, Jing Tao, Pedro HC Camargo, Yimei Zhu, and Younan Xia. Shape-controlled synthesis of pd nanocrystals in aqueous solutions. *Advanced Functional Materials*, 19(2):189–200, 2009.

[52] Tao Xu, MP Zach, ZL Xiao, D Rosenmann, U Welp, WK Kwok, and GW Crabtree. Self-assembled monolayer-enhanced hydrogen sensing with ultrathin palladium films. *Applied Physics Letters*, 86(20):203104, 2005.

[53] Thomas Kiefer, Luis Guillermo Villanueva, Frédéric Fargier, Frédéric Favier, and Jürgen Brugger. The transition in hydrogen sensing behavior in noncontinuous palladium films. *Applied Physics Letters*, 97(12):121911, 2010.

[54] Robert W Kelsall, Ian W Hamley, Mark Geoghegan, and John Wiley. *Nanoscale science and technology*. Wiley Online Library, 2005.

[55] Farid Bensebaa. *Nanoparticle technologies: from lab to market*, volume 19. Academic Press, 2012.

[56] Lu Lu, Igor Sevonkaev, Ajeet Kumar, and Dan V Goia. Strategies for tailoring the properties of chemically precipitated metal powders. *Powder Technology*, 261:87–97, 2014.

[57] Stefan Sepeur. *Nanotechnology: technical basics and applications*. Vincentz Network GmbH & Co KG, 2008.

[58] F Bozon-Verduraz, R Brayner, Valerii Veniaminovich Voronov, Nikolai Aleksandrovich Kirichenko, Aleksandr Vladimirovich Simakin, and Georgii Airatovich Shafeev. Production of nanoparticles by laser-induced ablation of metals in liquids. *Quantum Electronics*, 33(8):714–720, 2003.

[59] Khaled Habiba, Vladimir I Makarov, Brad R Weiner, and Gerardo Morell. Fabrication of nanomaterials by pulsed laser synthesis. *Manufacturing Nanostructures, One Central Press, Manchester, UK*, 2014.

[60] Peter Schaaf. *Laser processing of materials: fundamentals, applications and developments*, volume 139. Springer Science & Business Media, 2010.

[61] Dimitri Batani, Tommaso Vinci, and Davide Bleiner. Laser-ablation and induced nanoparticle synthesis. *Laser and Particle Beams*, 32(01):1–7, 2014.

[62] Wei-Hong Zhong. *Nanoscience and nanomaterials: synthesis, manufacturing and industry impacts*. DEStech Publications, Inc, 2012.

[63] Hari Singh Nalwa. *Handbook of Nanostructured Materials and Nanotechnology, Five-Volume Set*. Academic Press, 1999.

[64] Juh Tzeng Lue. Physical properties of nanomaterials. *Encyclopedia of nanoscience and nanotechnology*, 10(1), 2007.

[65] Jong-Hee Park and TS Sudarshan. *Chemical vapor deposition*, volume 2. ASM international, 2001.

[66] Hans Leuenberger. The application of percolation theory in powder technology. *Advanced Powder Technology*, 10(4):323–352, 1999.

[67] MB Isichenko. Percolation, statistical topography, and transport in random media. *Reviews of modern physics*, 64(4):961, 1992.

[68] Scott Kirkpatrick. Percolation and conduction. *Reviews of modern physics*, 45(4):574, 1973.

[69] M Sahini and M Sahimi. *Applications of percolation theory*. CRC Press, 1994.

[70] Paul Heitjans and Jörg Kärger. *Diffusion in condensed matter*. Springer, 2005.

[71] Daniel E Browne, Matthew B Elliott, Steven T Flammia, Seth T Merkel, Akimasa Miyake, and Anthony J Short. Phase transition of computational power in the resource states for one-way quantum computation. *New Journal of Physics*, 10(2):023010, 2008.

[72] Richard Zallen. *The physics of amorphous solids*. John Wiley & Sons, 1983.

[73] BI Shklovskiĭ and AL Efros. Percolation theory and conductivity of strongly inhomogeneous media. *Soviet Physics Uspekhi*, 18(11):845, 1975.

[74] Ce-Wen Nan. Physics of inhomogeneous inorganic materials. *Progress in Materials Science*, 37(1):1–116, 1993.

[75] C-W Nan, Y Shen, and Jing Ma. Physical properties of composites near percolation. *Annual Review of Materials Research*, 40:131–151, 2010.

[76] Vladimir M Shalaev. *Nonlinear optics of random media: fractal composites and metal-dielectric films*. Number 158. Springer, 2000.

[77] JP Clerc, G Giraud, JM Laugier, and JM Luck. The electrical conductivity of binary disordered systems, percolation clusters, fractals and related models. *Advances in Physics*, 39(3):191–309, 1990.

[78] David J Bergman and David Stroud. Physical properties of macroscopically inhomogeneous media. *solid state physics*, 46:147–269, 1992.

[79] Pavel Šmilauer. Thin metal films and percolation theory. *Contemporary Physics*, 32(2):89–102, 1991.

[80] Tsuneyoshi Nakayama and Kousuke Yakubo. *Fractal concepts in condensed matter physics*, volume 140. Springer, 2003.

[81] Junjie Wu and DS McLachlan. Percolation exponents and thresholds obtained from the nearly ideal continuum percolation system graphite-boron nitride. *Physical Review B*, 56(3):1236, 1997.

[82] BI Halperin, Shechao Feng, and PN Sen. Differences between lattice and continuum percolation transport exponents. *Physical review letters*, 54(22):2391, 1985.

[83] Wen-Zhong Cai, Shan-Tung Tu, and Jian-Ming Gong. A physically based percolation model of the effective electrical conductivity of particle filled composites. *Journal of composite materials*, 40(23):2131–2142, 2006.

[84] Harvey Scher and Richard Zallen. Critical density in percolation processes. *The Journal of Chemical Physics*, 53(9):3759, 1970.

[85] Shechao Feng, BI Halperin, and PN Sen. Transport properties of continuum systems near the percolation threshold. *Physical Review B*, 35(1):197, 1987.

[86] Isaac Balberg. Recent developments in continuum percolation. *Philosophical Magazine Part B*, 56(6):991–1003, 1987.

[87] David S McLachlan, Michael Blaszkiewicz, and Robert E Newnham. Electrical resistivity of composites. *Journal of the American Ceramic Society*, 73(8):2187–2203, 1990.

[88] MAJ Michels. Scaling relations and the general effective-medium equation for isolator-conductor mixtures. *Journal of Physics: Condensed Matter*, 4(15):3961, 1992.

[89] David Stroud. The effective medium approximations: Some recent developments. *Superlattices and microstructures*, 23(3):567–573, 1998.

[90] MPJ Van Staveren, HB Brom, and LJ De Jongh. Metal-cluster compounds and universal features of the hopping conductivity of solids. *Physics reports*, 208(1):1–96, 1991.

[91] CM Mari and G Dotelli. How to forecast the electrical behaviour of ionic conductor composites? *Journal of materials science*, 36(5):1141–1147, 2001.

[92] DS McLachlan. Equation for the conductivity of metal-insulator mixtures. *Journal of Physics C: Solid State Physics*, 18(9):1891, 1985.

[93] David S McLachlan. Analytical functions for the dc and ac conductivity of conductor-insulator composites. *Journal of Electroceramics*, 5(2):93–110, 2000.

[94] DS McLachlan. A quantitative analysis of the volume fraction dependence of the resistivity of cermets using a general effective media equation. *Journal of applied physics*, 68(1):195–199, 1990.

[95] Junjie Wu and D.S. McLachlan. Percolation exponents and threshold in two nearly ideal anisotropic continuum systems. *Physica A: Statistical Mechanics and its Applications*, 241(12):360 – 366, 1997. Proceedings of the Fourth International Conference on Electrical Transport and Optical Properties of Inhomogeneoous Media.

[96] R.S. Popovic. *Hall Effect Devices: Magnetic Sensors and Characterization of Semiconductors*. Series in Sensors. Taylor & Francis, 1991.

[97] E. H. Hall. On a new action of the magnet on electric currents. *American Journal of Mathematics*, 2(3):pp. 287–292, 1879.

[98] Colin M Hurd. Hall effect in metals and alloys. 1972.

[99] W. A. Reed and E. Fawcett. High-field galvanomagnetic properties of metals. *Science*, 146(3644):pp. 603–610, 1964.

[100] E Fawcett. High-field galvanomagnetic properties of metals. *Advances in Physics*, 13(50):139–191, 1964.

[101] Radivoje S Popovic. *Hall effect devices*. CRC Press, 2010.

[102] Ernest Henry Putley. *The Hall effect and related phenomena*, volume 88. Butterworths London, 1960.

[103] G. Burns. *Solid state physics*. Academic Press, 1985.

[104] Kasper A Borup, Eric S Toberer, Leslie D Zoltan, George Nakatsukasa, Michael Errico, Jean-Pierre Fleurial, Bo B Iversen, and G Jeffrey Snyder. Measurement of the electrical resistivity and hall coefficient at high temperatures. *Review of Scientific Instruments*, 83(12):123902, 2012.

[105] D.D. Pollock. *Physical Properties of Materials for Engineers*. Taylor & Francis, 1993.

[106] Some General Input-output Rules Governing. The hall effect and its applications. 1980.

[107] E. Ramsden. *Hall-Effect Sensors: Theory and Application*. Elsevier Science, 2011.

[108] Colin M Hurd. The dynamics of electrons in metals: low-temperature effects. In *The Hall Effect in Metals and Alloys*, pages 5–50. Springer, 1972.

[109] DKC Macdonald and K Sarginson. Galvanomagnetic effects in conductors. *Reports on progress in physics*, 15(1):249, 1952.

[110] EH Sondheimer. The theory of the galvanomagnetic and thermomagnetic effects in metals. *Proceedings of the Royal Society of London. Series A. Mathematical and Physical Sciences*, 193(1035):484–512, 1948.

[111] RD Barnard. The true low-field hall coefficient of high-purity coefficient of high-purity silver and silver containing low-density defects at low temperatures. *Journal of Physics F: Metal Physics*, 7(4):673, 1977.

[112] MD Wilding. The hall effect in palladium and dilute iron-palladium alloys. *Proceedings of the Physical Society*, 90(3):801, 1967.

[113] Colin M Hurd. The hall effect in limiting cases. In *The Hall Effect and Alloys*, pages 51–92. Springer, 1972.

[114] Dow Cellulosics. Ethocel: Ethylcellulose polymers technical handbook. *TDC Company (Ed.), Dow Cellulosics*, page 28, 2005.

[115] Dow. Butyl cellosolve acetate solvent: Technical data sheet. *TDC Company (Ed.), Dow*, page 2, 2004.

[116] J.K. Spelt, Y. Rotenberg, D.R. Absolom, and A.W. Neumann. Sessile-drop contact angle measurements using axisymmetric drop shape analysis. *Colloids and Surfaces*, 24(23):127 – 137, 1987.

[117] Renate Frch, Holger A. Schnherr, and Tobias A. Jenkins, editors. *Appendix C: Contact Angle Goniometry*, pages 471–473. Wiley-VCH Verlag GmbH & Co. KGaA, 2009.

[118] M. Härting, J. Zhang, D. R. Gamota, and D. T. Britton. Fully printed silicon field effect transistors. *Applied Physics Letters*, 94(19):193509, 2009.

[119] Daniel Gamota. *Printed organic and molecular electronics*. Springer, 2004.

[120] Andreas Willfahrt, John Stephens, and Gunter Hübner. Optimising stencil thickness and ink film deposit.

[121] Frederik C. Krebs. Fabrication and processing of polymer solar cells: A review of printing and coating techniques. *Solar Energy Materials and Solar Cells*, 93(4):394 – 412, 2009.

[122] Eszter Horvath, Gabor Henap, and Gabor Harsanyi. Materials and technological developement of screen printing in transportation. *International Journal for Traffic and Transport Engineering*, 2(2), 2012.

[123] Ken Gilleo. *Polymer thick film: today's emerging technology for a clean environment tomorrow*. Springer, 1996.

[124] G Carter. The physics and applications of ion beam erosion. *Journal of Physics D: Applied Physics*, 34(3):R1, 2001.

[125] Richard Wirth. Focused ion beam (fib) combined with sem and tem: Advanced analytical tools for studies of chemical composition, microstructure and crystal structure in geomaterials on a nanometre scale. *Chemical Geology*, 261(3):217–229, 2009.

[126] CA Volkert, AM Minor, et al. Focused ion beam microscopy and micromachining. *Mrs Bull*, 32(5):389–395, 2007.

[127] N Erdman, R Campbell, and S Asahina. Precise sem cross-section polishing via argon beam milling. *Microscopy Today*, 14(3):22–25, 2006.

[128] Joachim Mayer, Lucille A. Giannuzzi, Takeo Kamino, and Joseph Michael. Tem sample preparation and fib-induced damage. *MRS Bulletin*, 32:400–407, 5 2007.

[129] OV Kolosov, I Grishin, and R Jones. Material sensitive scanning probe microscopy of subsurface semiconductor nanostructures via beam exit ar ion polishing. *Nanotechnology*, 22(18):185702, 2011.

[130] Sam M Stevens, Kjell Jansson, Changhong Xiao, Shunsuke Asahina, Miia Klingstedt, Daniel Grüner, Yasuhiro Sakamoto, Keiichi Miyasaka, Pablo Cubillas, Rhea Brent, et al. An appraisal of high resolution scanning electron microscopy applied to porous materials.

[131] Hideyuki Takahashi, Ayako Sato, Masaru Takakura, Norihisa Mori, Juergen Boerder, Walter Knoll, and John Critchell. A new method of surface preparation for high spatial resolution epma/sem with an argon ion beam. *Microchimica Acta*, 155(1-2):295–300, 2006.

[132] KeeHyun Kim, Makoto Watanabe, Seiji Kuroda, and Naomi Kawano. Observation of high resolution microstructures in thermal sprayed coatings and single deposited splats using ion beam milling. *Materials transactions*, 52(3):439–446, 2011.

[133] MW Phaneuf. Applications of focused ion beam microscopy to materials science specimens. *Micron*, 30(3):277–288, 1999.

[134] L.A. Giannuzzi and F.A. Stevie. A review of focused ion beam milling techniques for {TEM} specimen preparation. *Micron*, 30(3):197 – 204, 1999.

[135] PR Munroe. The application of focused ion beam microscopy in the material sciences. *Materials characterization*, 60(1):2–13, 2009.

[136] Steve Reyntjens and Robert Puers. A review of focused ion beam applications in microsystem technology. *Journal of Micromechanics and Microengineering*, 11(4):287, 2001.

[137] Warren J. MoberlyChan, David P. Adams, Michael J. Aziz, Gerhard Hobler, and Thomas Schenkel. Fundamentals of focused ion beam nanostructural processing: Below, at, and above the surface. *MRS Bulletin*, 32:424–432, 5 2007.

[138] Lake Shore. Lake shore 7500/9500 series hall system user's manual, 2004.

[139] LJ van der Pauw. A method of measuring specific resistivity and hall effect of discs of arbitrary shape. 1958.

[140] Sumio Sakka. *Handbook of sol-gel science and technology. 2. Processing, characterization, and applications*, volume 2. Springer, 2005.

[141] Nicola Pinto and Roberto Murri. Chapter 9 - magnetotransport effects in semiconductors. In Hari Singh Nalwa, editor, *Handbook of Thin Films*, pages 439 – 494. Academic Press, Burlington, 2002.

[142] Hewlett Packard. Operation and service manual 4192a lf impedance analyzer, 1984.

[143] Ruben Bjorge. *Lattice-fringe fingerprinting: Structural identification of nanocrystals employing high-resolution transmission electron microscopy.* PhD thesis, Portland State University, 2007.

[144] Ray Egerton. *Physical principles of electron microscopy: an introduction to TEM, SEM, and AEM.* Springer Science & Business Media, 2006.

[145] CT Schamp. High-resolution metrology in the tem. *Microscopy Today*, 20(03):46–49, 2012.

[146] Andreas Heilmann. *Polymer films with embedded metal nanoparticles*, volume 52. Springer Science & Business Media, 2013.

[147] Christopher Hammond and Christopher Hammond. *The basics of crystallography and diffraction*. Oxford University Press Oxford, 2009.

[148] William F.. Smith and Javad Hashemi. *Foundations of materials science and engineering*. Mcgraw-Hill Publishing, 2006.

[149] A Buffler, S Allie, F Lubben, and B Campbell. Introduction to measurement in the physics laboratory. a probabilistic approach, 2007.

[150] Batsirai Magunje. *Charge Transport in Printed Silicon Nanoparticle Networks*. PhD thesis, University of Cape Town, 2013.

[151] Vadim F. Lvovich. *Equivalent-Circuit Elements and Modeling of the Impedance Phenomenon*. John Wiley Sons, Inc., 2012.

[152] M.R. Shoar Abouzari, F. Berkemeier, G. Schmitz, and D. Wilmer. On the physical interpretation of constant phase elements. *Solid State Ionics*, 180(1416):922 – 927, 2009.

[153] Jean-Baptiste Jorcin, Mark E Orazem, Nadine Pébère, and Bernard Tribollet. Cpe analysis by local electrochemical impedance spectroscopy. *Electrochimica Acta*, 51(8):1473–1479, 2006.

[154] CH Hsu and F Mansfeld. Technical note: concerning the conversion of the constant phase element parameter y0 into a capacitance. *Corrosion*, 57(9):747–748, 2001.

[155] Li-Tang Yan and Xu-Ming Xie. Computational modeling and simulation of nanoparticle self-assembly in polymeric systems: Structures, properties and external field effects. *Progress in Polymer Science*, 38(2):369–405, 2013.

[156] D Toker, D Azulay, N Shimoni, I Balberg, and O Millo. Tunneling and percolation in metal-insulator composite materials. *Physical review B*, 68(4):041403, 2003.

[157] I Balberg. Tunneling and nonuniversal conductivity in composite materials. *Physical Review Letters*, 59(12):1305, 1987.

[158] Haoyan Wei and Hergen Eilers. From silver nanoparticles to thin films: Evolution of microstructure and electrical conduction on glass substrates. *Journal of Physics and Chemistry of Solids*, 70(2):459–465, 2009.

[159] Franz Faupel, Vladimir Zaporojtchenko, Thomas Strunskus, and Mady Elbahri. Metal-polymer nanocomposites for functional applications. *Advanced Engineering Materials*, 12(12):1177–1190, 2010.

[160] EK Sichel and JI Gittleman. The hall effect in granular metal films near the percolation threshold. *Solid State Communications*, 42(2):75–77, 1982.

[161] GP Zhigal'skii and Brian K Jones. *The physical properties of thin metal films*, volume 13. CRC Press, 2003.

[162] Robert Mount Hill. Electrical conduction in ultra thin metal films. i. theoretical. *Proceedings of the Royal Society of London. A. Mathematical and Physical Sciences*, 309(1498):377–395, 1969.

[163] HB Peacock. Hall effect in evaporated films of iron, cobalt, nickel, palladium, and platinum. *Physical Review*, 27(4):474, 1926.

[164] John C Steinberg. Hall effect and specific resistance of evaporated films of silver, copper and iron. *Physical Review*, 21(1):22, 1923.

[165] OA Panchenko, PP Lutsishin, and YG PTUSHINSKY. Galvanomagnetic effects in thin films of some transition metals. *SOV PHYS JETP*, 29(1):76–78, 1969.

[166] V Švorčík, J Siegel, P Šutta, J Mistrík, P Janíček, P Worsch, and Z Kolská. Annealing of gold nanostructures sputtered on glass substrate. *Applied Physics A*, 102(3):605–610, 2011.

[167] Shweta Jagtap, Sunit Rane, Rohini Aiyer, Suresh Gosavi, and Dinesh Amalnerkar. Study of microstructure, impedance and dc electrical properties of ruo 2–spinel based screen printed greenntc thermistor. *Current Applied Physics*, 10(4):1156–1163, 2010.

[168] Toshihiro Nakamura, Kohei Homma, and Kunihide Tachibana. Thin film deposition of metal oxides in resistance switching devices: electrode material dependence of resistance switching in manganite films. *Nanoscale research letters*, 8(1):1–7, 2013.

[169] JW Orton and MJ Powell. The hall effect in polycrystalline and powdered semiconductors. *Reports on Progress in Physics*, 43(11):1263, 1980.

[170] NM White and JD Turner. Thick-film sensors: past, present and future. *Measurement Science and Technology*, 8(1):1, 1997.